Morris, J.D., Villinger, H.W., Klaus, A., et al., 2003
Proceedings of the Ocean Drilling Program, Initial Reports Volume 205

1. LEG 205 SUMMARY[1]

Shipboard Scientific Party[2]

ABSTRACT

The character of the incoming plate subducting at convergent margins and the processes affecting the plate as it passes below the shallow forearc may play a major role in the nature and extent of hazardous intraplate seismicity as well as the magnitude of volcanism and the chemistry of lavas produced in the overlying volcanic arc. The fate of incoming sediments and ocean crust and of their associated volatiles as they pass through the shallow levels of a subduction zone (0–50 km depth) has profound effects on the behavior of the seismogenic zone, which produces most of the world's destructive earthquakes and tsunamis. Fluid pressure and sediment porosity influence fault localization, deformation style, and strength and may control the updip limit of the seismogenic zone. Fluids within both fault zones and sediments underthrust at the trench affect early structural development and are key agents in transport of chemical species. The mineralogy and chemistry of any subducted sediments and their dehydration reactions, governed by the thermal structure of the plate during subduction, may control the physical properties of the deeper subduction interface and, hence, the updip and downdip limits of the seismogenic zone wherein interplate earthquakes are generated. The mineralogy, composition, and volatile content of the slab, transformed during its progress through the shallow subduction zone, will govern the flux of fluids or melts from slab to mantle wedge, which is an important control on the extent of mantle melting and formation of arc lavas.

Costa Rica is an important area for studies of the seismogenic zone and subduction factory for several reasons. As one of the few modern arcs subducting a carbonate-rich sediment section, Central America permits study of CO_2 recycling through a subduction zone. Changes along strike in seismicity, plate coupling, and volume and composition of the arc lavas (between Nicaragua and Costa Rica) appear to correlate with

---

[1] Examples of how to reference the whole or part of this volume.
[2] Shipboard Scientific Party addresses.

changes in sediment dynamics. The balance between sediment accretion, underplating, erosion, and subduction may ultimately result from changing bathymetry, thermal structure, or hydrological behavior along the margin.

Science objectives for Leg 205 had two primary foci, both related to seismogenic zone and subduction factory questions. The first was to determine the igneous and alteration history of the uppermost part of the downgoing plate at reference Site 1253, along with the inferred distribution of fracture permeability in the core and borehole. The second was to characterize and monitor two of the three hydrological systems inferred from Leg 170 results: in basement at Site 1253 and along the décollement (or upper fault zone) at Sites 1254 and 1255. These goals were accomplished by (1) targeted coring of selected intervals, (2) downhole temperature and pressure measurements, (3) logging at Site 1253, and (4) installation of long-term observatories (CORK-IIs) to monitor temperature and pressure and to sample fluids and gases in each of the hydrologic systems. In the décollement zone, instruments were also deployed to attempt to measure fluid flow rates. Temporal variation of fluid composition in the sealed-off intervals will be obtained using osmotic fluid samplers. The samplers and temperature loggers will be recovered for analysis 1 to 2 years after installation, pressure data will be downloaded, and new samplers and temperature probes will be installed.

Science objectives specific to the reference Site 1253 center on mass flux to the subduction trench (and ultimately the volcanic arc) as well as the permeability and hydrology of the downgoing igneous section. In conjunction with Leg 170, coring during Leg 205 provided samples that will allow us to improve on and, thus, better constrain the estimate of the sedimentary carbonate flux to the trench. Although not a primary focus of the cruise, coring from the two legs also provides an extensive ash stratigraphy as the plate moved from near the Galapagos to outboard of the Middle America Trench. Leg 205 coring into the igneous section will be used to investigate the extent of sill emplacement and its origin and contribution to the bulk composition of the subducting plate along with its tectonic and magmatic implications. If a transition to basement is recognized in the lower igneous section, the extensive recovery of Leg 205 can be used to determine the primary and secondary mineralogy and bulk chemistry of the uppermost part of the downgoing plate. These results can be integrated with those from the deep basement hole cored during Leg 206 (also on the part of the Cocos plate generated at the East Pacific Rise) to constrain the composition of the oceanic crust subducting at this margin. Microbial samples were taken (and contamination tests run) from the sedimentary horizons and from larger veins and fractures in the lower part of the igneous sections for postcruise studies. Logging, coring, and physical properties measured during Leg 205 establish key characteristics relevant to fluid flow and deformation, such as porosity, density, fracture distribution, orientation, and strength, ultimately to be used in conjunction with pressure, temperature, and chemical data from the CORK-II seafloor observatory.

Science objectives for the prism Sites 1254 and 1255 centered on the development of the décollement, the use of pore fluid chemistry to infer local diagenetic and deeper dehydration reactions, and the installation of two CORK-IIs, ideally in the region of maximum fluid flow within the décollement or related fault zones. Leg 205 coring intersected a thrust fault, as well as the décollement zone, in two locations slightly different from the two sites cored during Leg 170. Together, they provide the opportunity to examine variability over short distances in the development of the fault zones, the role of variable sediment lithology in strain partitioning and the style of décollement development, and the interplay between structural features and zones of fluid flow. Postcruise analysis of structural fabrics and experiments on whole-round samples will better constrain hydrological models and permit integration of fluid flow and deformation models. Sediments, gases, and interstitial waters collected in the thrust fault and décollement during Legs 170 and 205 have some chemical features expected of deeply sourced fluids and provide samples for postcruise chemical and isotopic analyses, as well as for identifying key horizons for the CORK-II long-term seafloor observatory. Whole-round samples from the décollement and contamination testing allow for postcruise microbiological investigations to determine the resident microbial ecology of the zone for comparison to eventual microbial experiments on fluids collected from the décollement.

Installation of long-term seafloor observatories was a major focus of Leg 205. The modified CORK-II design is discussed in detail in **Jannasch et al.** (this volume). Briefly, the CORK-II is built around and within a 4½-in casing string and monitors a single interval below a single packer. Deployments here combine pressure monitoring as used during Leg 196 with retrievable OsmoSamplers at the horizon of interest (containing osmotic fluid and gas samplers and temperature loggers). At prism Site 1255, OsmoFlowmeters that were included use the dilution of two chemical tracers injected at a constant rate to estimate flow rates.

At Site 1253 on the incoming plate, we cored 230 m, including ~170 m within two igneous units where the upper unit is a 30-m-thick gabbro sill with sediments above and below. We also logged up to 150 m, primarily in the lower igneous section, and installed a CORK-II observatory. Interstitial water chemistry from above and below the sill indicates that there is fluid flow, of near-seawater composition, at depth in the igneous section. The lower igneous unit (Subunit 4B) is composed of microcrystalline to fine-grained gabbro with rare intervals of basalt and medium-grained gabbro; all are of basaltic composition. It may be an exceptionally thick sill composed of multiple intrusions related to Galapagos hotspot activity or a series of thick, slowly cooled lava flows of oceanic crust created at the East Pacific Rise, or it may represent a transition between extrusive and intrusive activity at the ridge. The lower igneous unit is more extensively altered and fractured below ~510–513 meters below seafloor (mbsf). A CORK-II was installed, with temperature probes and two osmotic fluid and gas samplers centered at 500.4 and 515.8 mbsf. Pressure monitoring is within the upper OsmoSampler zone and above the packer (centered at ~452.8 mbsf).

At Site 1254 in the prism, we cored through a thrust fault zone at ~197–219 mbsf and the décollement zone at 338–365 mbsf. Despite drilling disturbance, it is possible to see that deformation, particularly brecciation and brittle shearing, generally increase downward in both zones but with shear concentrated along specific horizons. High concentrations of thermogenic hydrocarbons in the gases and sediments and unique pore water chemistry are seen within both zones, indicating advection of deeply sourced fluids. The base of the décollement lies within the uppermost part of the underthrust section at Site 1254, as opposed to that between the prism and underthrust sediment as seen at Site 1040, which is 50 m away. Two attempts were made to install a

CORK-II at Site 1254, once into the décollement zone and once into the shallower thrust fault. All failed because of a combination of operational difficulties and hole conditions.

At Site 1255, ~0.4 km inboard of the deformation front, we conducted very limited coring and installed a CORK-II into the plate boundary fault. The base of the décollement was placed at 144 mbsf, corresponding to the lithologic boundary between prism and underthrust sediments. The chemical signatures of a deeply sourced fluid were observed just above the décollement, but are weaker than those at Site 1254. The CORK-II was installed successfully, with the packer centered at 129 mbsf and the OsmoSampler (with a capability to provide approximate flow rates) centered at 140 mbsf, along with a temperature logger and pressure monitoring screen.

INTRODUCTION

The character of the incoming plate subducting at convergent margins and the processes affecting the plate as it passes below the shallow forearc may play a major role in the nature and extent of hazardous interplate seismicity as well as the magnitude of volcanism and the chemistry of lavas produced in the overlying volcanic arc. The fate of incoming sediments and oceanic crust, and of their associated volatiles, as they pass through the shallow levels of a subduction zone (0–50 km depth) has profound effects on the behavior of the seismogenic zone, which produces most of the world's destructive earthquakes and tsunamis. Fluid pressure and sediment porosity influence fault localization, deformation style, and strength and may control the updip limit of the seismogenic zone (e.g., Scholz, 1998; Moore and Saffer, 2001). Fluids within both fault zones and sediments underthrust at the trench affect early structural development and are key agents in the transport of chemical species. The mineralogy and chemistry of any subducted sediments and their dehydration reactions during subduction may control the physical properties of the shallower and deeper subduction interface and, hence, updip and downdip limits of the seismogenic zone.

The escape of fluids to the surface from the downgoing plate at depth (return flow) may support a deep biosphere, contributes methane and higher molecular weight hydrocarbons for gas hydrate formation, affects seawater chemistry for selected elements and isotopes, and is intimately linked to deformation, faulting, and the evolution of the décollement. The distillation and loss of some volatiles and fluid-soluble elements from the shallow slab not only affect reactions and processes within the seismogenic zone, but they also play a central role in the supply of residual volatiles to the deeper Earth and change the composition of the slab delivered to the depths of magmatism beneath volcanic arcs. Processes operating in the shallow subduction zone thus affect the way the slab contributes to continent-building magmatism, explosive volcanism, ore formation, and ultimately, the evolution of the mantle through time (collectively known as the subduction factory). The subduction signature recorded in the chemistry of arc volcanic rocks constrains the nature and sometimes the volume of the sediments transported through the seismogenic zone to the depths of magmatism. The arc volcanism thus acts as a flow monitor for the transport of sediments to depths greater than those that can be drilled or seismically imaged.

The Ocean Drilling Program (ODP) has identified deformation at convergent margins, fluid flow in the lithosphere, and subduction zone geochemical fluxes as important aspects of the JOIDES Long Range Plan (JOIDES Planning Committee, 1996). The Initial Science Plan for the Integrated Ocean Drilling Program includes an initiative focused on the seismogenic zone. The Central American convergent margin (Fig. **F1**) has been a focus area for a number of national and international programs studying the seismogenic zone and subduction factory for several reasons. First, it is one of the few modern subduction zones that is subducting a significant carbonate section and thus provides an opportunity to investigate CO_2 cycling through convergent margins. Second, along strike from Nicaragua to Costa Rica (Fig. **F2**), the style and extent of seismicity changes. Third, along the same section, the style of arc volcanism changes, as do volumes and the chemistry of the arc lavas. Changes in both the seismicity and volcanic chemistry have been proposed to result from changes in the balance between sediment underplating, erosion, and subduction (collectively referred to here as sediment dynamics), perhaps related to changing bathymetry, thermal structure, and hydrological behavior along the margin.

F1. Location of Leg 205 drilling area, p. 42.

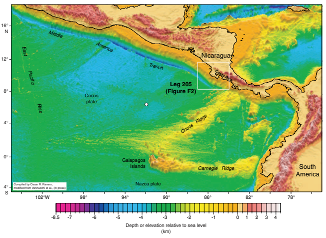

F2. Bathymetric map of the Middle America Trench, p. 43.

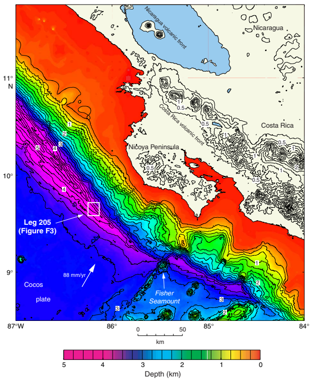

Leg 205, building on Leg 170 coring and logging while drilling (LWD) at the same sites (Fig. **F3**), was designed to investigate the composition of the downgoing plate together with the thermal structure and hydrological activity across the Costa Rica margin. This was and will be achieved through a combination of downhole measurements and long-term sampling of fluids and gases as well as monitoring of fluid pressure, temperature, and flow rate at critical horizons. First observations of temporal variations of fluid and gas chemistry will be available once the fluid and gas samples have been recovered 1 to 2 years postcruise. During the leg, we also drilled and cored into the subducting igneous section to characterize the mass and fluid fluxes to the volcanic arc together with their chemical compositions. The high recovery during coring through the décollement zone in the prism sites provided the opportunity to evaluate local heterogeneity in the development of the décollement (in conjunction with Leg 170 results) and to integrate the location and magnitude of pore fluid anomalies with structural fabrics observed in the cores.

F3. Bathymetric map of Leg 205 and 170 drill sites, p. 44.

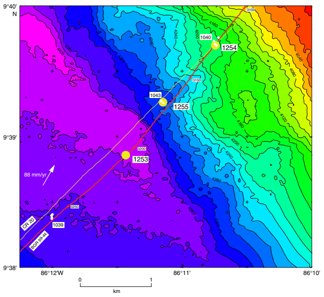

The Central America Seismogenic Zone and Subduction Factory

A large body of work describes differences in seismicity and arc magmatism along the length of the Central American margin (Fig. **F1**), with sharp contrasts between Nicaragua and immediately adjacent parts of Costa Rica. The Nicoya section of the Costa Rica margin appears to produce earthquakes with a moment magnitude (M_w) of 7 or greater at a 40- to 50-yr recurrence interval, with the last such event in 1950 (Guendel, 1986). Mechanical coupling between the downgoing and overriding (often termed "locking") plates is estimated from Global Positioning System data to be 40%–60% (T. Dixon, pers. comm., 2001) and appears to start ~15 km arcward of the trench. Nicaragua is characterized by a greater frequency of $M_w \geq 7$ earthquakes, including the 1992 tsunamigenic earthquake. In detail, the updip limit of seismicity appears to be at ~20 km depth north of the fracture zone trace shown in Figure **F4** and at ~10 km depth to the south (Newman et al., 2002).

F4. Leg 205 drilling area and isochrons, p. 45.

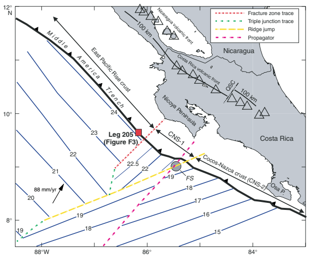

There are also significant changes in volcanism between Nicaragua and Costa Rica. Figure **F2** shows an offset in the volcanic chain just north of the northernmost Nicoya Peninsula. In Nicaragua, the arc-trench gap is 180–190 km and the volcanoes lie ~180–200 km above the Waditi-Benioff Zone of the downgoing slab. In Costa Rica, the arc-trench gap narrows to ~165 km and the seismic zone is ~120–130 km below the volcanoes (Protti et al., 1994). Nicaraguan volcanoes tend to be smaller than those of Costa Rica as shown in Figure **F2;** when averaged over the last 100–130 k.y., magma production rates, compiled in Patino et al. (2000), are much lower in Nicaragua than Costa Rica (~14 and 44 km^3/km arc length per million years, respectively). In the chemistry of the arc volcanic rocks, ^{10}Be data, radiogenic isotopes, and trace element studies of Nicaraguan lavas (Tera et al., 1986; Carr et al., 1990; Reagan et al., 1994; Patino et al., 2000) suggest that the entire sediment section is subducting to the depths of magma generation, producing in the lavas a strong signature from the hemipelagic sediments at the top of the incoming sediment section. In contrast, the Costa Rican lavas have a much smaller sediment signature, little contribution from the uppermost hemipelagic sediments of the incoming plate, and a proportionally larger contribution from the basal carbonate section.

The differences in arc chemistry along strike cannot be explained easily by variations in the lithology or chemistry of the incoming plate. Figure **F5** shows the lithologic section entering the trench offshore Guatemala (Deep Sea Drilling Project Site 495) and Costa Rica (ODP Sites 1039 and 1253). The two sections show 150–180 m of diatom-rich hemipelagic sediments overlying 230–250 m of calcareous nannofossil oozes and chalks. Given the similarity of the subducting sediment sections along the Middle America Trench, differences in the sediment signature between the Nicaraguan and Costa Rican volcanoes are likely caused by variations in sediment dynamics.

F5. Summary of recovered lithology, p. 46.

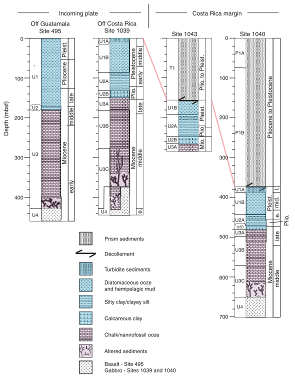

Various workers have suggested that the changing nature of seismicity and arc volcanism along the Middle America Trench may be due to variations in the incoming plate, the fate of incoming sediments as they traverse the forearc of the overriding plate, or a combination of the two. The bathymetry and thermal structure of the incoming plate and the active fluid flow both outboard and inboard of the trench may play a key role in deformation and sediment dynamics across the margin. In addition, differences in origin and chemistry of the subducting oceanic crust may also contribute to changing chemistry of the arc lavas. These issues are addressed in more detail in the following section.

Geological and Geophysical Setting

Geophysical Database

The structure of the Middle America Subduction Zone (Fig. **F1**) has been intensively studied by North American and German geophysicists since the early 1980s. The collected data sets comprise bathymetric and side-scan sonar surveys, seismic refraction and reflection studies, and passive seismological experiments (Christeson et al., 2000; McIntosh et al., 1993; Ranero et al., 2000a, 2000b; von Huene et al., 2000). Potential field investigations were mostly done in conjunction with seismic studies and bathymetric mapping. In Barckhausen et al. (1998, 2001), all marine magnetic data from Nicaragua south to the Carnegie Ridge were interpreted to unravel the tectonic history of the Cocos-Nazca spreading center (CNS) and the adjacent Cocos plate offshore Costa Rica. In addition, recent heat flow surveys at the margin of Costa Rica and Nicaragua (*Meteor* 54-2, 2002) and seaward on the Cocos plate offshore the Nicoya Peninsula (TicoFlux I, 2001; TicoFlux II, 2002) complement older existing data sets by Langseth and Silver (1996). The regional tectonic history with special emphasis on subduction erosion is discussed by Meschede et al. (1999a, 1999b), Ranero and von Huene (2000), Abratis and Woerner (2001), and Vannucchi et al. (2001). Pore pressures and the accompanying fluid and energy fluxes as well as the presence of gas hydrates in the area of Costa Rica are investigated in numerous papers (McIntosh and Sen, 2000; Kopf et al., 2000; Silver et al., 2000; Vannucchi and Tobin, 2000; Saffer et al., 2000; Ruppel and Kinoshita, 2000; Pecher et al., 2001; Chan and Kastner, 2000; Lückge et al., 2002; Saffer, in press). This compilation of published results comprises only recently published papers; additional references can be found in Kimura, Silver, Blum, et al. (1997) and Silver, Kimura, and Shipley (2001).

Oceanic Plate offshore Costa Rica

There are significant variations in the origin, morphology, and thermal structure of the incoming plate through the Nicaragua–Costa Rica segment of the Central American convergent margin (Figs. F1, F2). Large-scale tectonic features, such as the Carnegie and Cocos Ridges and the subduction trench, are clearly reflected in the regional bathymetry as shown in Figures F1 and F2. The topography of the incoming plate changes along the length of the margin (Fig. F1) (Ranero et al., 2000b): crust subducting beneath Nicaragua, formed at the East Pacific Rise (EPR), is pervasively faulted with offsets of up to 700 m on back-tilted normal faults (Kelly and Driscoll, 1998; Kelly et al., pers. comm., 2002), possibly associated with extensional tectonics caused by the flexure of the crust as it is subducted. The offsets become smaller closer to the Nicoya Peninsula, falling to <200 m. Farther to the southeast, seafloor relief in general is more pronounced (being southeast of the "rough-smooth boundary" of Hey, 1977) and the seafloor is covered by numerous seamounts (Figs. F1, F2). Crustal thickness increases slightly from ~5 km offshore Nicaragua to ~6 km offshore the Nicoya Peninsula (Ranero and von Huene, 2000). The thickness of the incoming sediments is generally in the range of 400–500 m.

Analysis of marine magnetic measurements (Hey, 1977; Lonsdale and Klitgord, 1978; Barckhausen et al., 2001) shows (Fig. F4) that ~20 km southeast of the Leg 205 transect, a fracture zone trace (FZT) separates lithosphere formed at the EPR from that formed at the CNS. This means that the drill holes of Leg 205 are underlain by crust that formed at the EPR at ~24 Ma. Analysis of magnetic anomaly data (Wilson, 1996) indicates that the crust at this location was formed at a full spreading rate of ~130 mm/yr. Seismic images of the FZT (Barckhausen et al., 2001) confirm the location of the boundary and reveal a jump up in basement depth of ~100–200 m from the EPR to CNS crust. The lithosphere to the southeast of the FZT formed at the CNS, with decreasing age to the southeast. The oldest crust directly at the FZT is 22.7 Ma, which corresponds to the breakup age of the Farallon plate. ODP Leg 206 Site 1256 (6°44.19′N, 91°56.06′W) is located on crust generated at the EPR at a full spreading rate of ~200 mm/yr in the immediate vicinity of the "rough-smooth boundary."

Convergence parameters are broadly similar along the margin. The convergence rate of the Cocos plate vs. the Caribbean plate increases only slightly from 83 mm/yr offshore Guatemala to 85 mm/yr offshore

Nicaragua and reaches 88 mm/yr offshore southernmost Costa Rica (DeMets et al., 1990). The convergence direction offshore the Nicoya Peninsula is almost perpendicular to the trench with the subducting plate dipping to the northeast (N25°–30°E). The maximum depth of seismicity gradually becomes shallower from Nicaragua (~200 km) to southern Costa Rica (~45 km). The dip angle of the slab in the upper 100 km is closely similar from Nicaragua to Central Costa Rica (~30°) and becomes steeper at 100 km depth with a value of ~80° (Protti et al., 1994).

The part of the Cocos plate that is presently being subducted offshore Costa Rica was overprinted by hotspot-related volcanism between 14 and 12 Ma (Barckhausen et al., 2001). This is most evident in the area of the Cocos Ridge offshore southern Costa Rica, but rock samples dredged from seamounts have proven that the overprinting extended at least as far north as the Fisher Seamount at the southern tip of the Nicoya Peninsula (Hauff et al., 1997). It seems possible that the sills encountered at the base of some of the ODP Leg 170 holes and at Site 1253 of Leg 205 and also observed in nearby seismic reflection profiles may be related to this volcanic event. One other interpretation (U. Barckhausen, pers. comm., 2002) would be that the FZT acted as a "leaky fault" and intruded magma into the bathymetrically lower sediments north of the FZT.

F6. Migrated multichannel seismic profile BGR-99-44, p. 47.

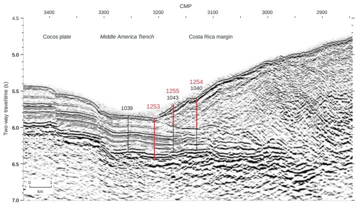

The seismic profile BGR-99-44, shown in Figure F6, reveals the general structure of the seaward side of the trench, the trench itself, and the lowermost seaward part of the prism. All drill sites of Leg 205 are located on this multichannel seismic (MCS) line (C. Reichert and C. Ranero, pers. comm., 2001) shot in 1999. The data were acquired with a 6-km, 1024-channel digital streamer using a 3-m^3 tuned air gun array and Differential Global Positioning System navigation. Data shown in Figure F6 are a near-trace (171-m offset) time-migrated section of the complete profile. The incoming pelagic sediments with a thickness of ~400 m show faults with offsets of 50–100 m seaward of the trench. A prominent reflector at 0.25 s two-way traveltime (TWT) below the seafloor marks the base of lithologic Subunit U3A (Fig. F5) (Kimura, Silver, Blum, et al., 1997) of late Miocene age. Beneath the sedimentary sequence, the strong reflector at 0.5 s (TWT below seafloor) images the top of a gabbro sill as revealed by drilling results from Leg 170 at Site 1039. The top of oceanic basement below the sill is very difficult if not impossible to identify based on the seismic records.

Forearc

Through extensive work, the structure of the forearc has been imaged. Limited ODP Leg 170 coring, drilling, and seismic data show that the bulk of the Pacific margin is a wedge-shaped high-velocity body probably made of rocks similar to the igneous oceanic rocks (Nicoya Ophiolite Complex) cropping out along the coast (Shipley et al., 1992; Kimura, Silver, Blum, et al., 1997; Ranero and von Huene, 2000), which precludes the existence of any significantly large sediment mass being recently accreted. Only a small sediment prism (<10 km wide) is located at the front of the margin wedge. Initially, MCS images were interpreted in terms of sediment accretion to the Costa Rica margin (Shipley et al., 1992). More recently, however, and in the wake of Leg 170 drilling, seismic images have been interpreted to show that basically the entire sediment cover of the ocean plate is currently underthrust beneath the margin and that the frontal sediment prism can store very little, if any, of the incoming material (Kimura, Silver, Blum, et al., 1997; Christeson et al., 1999, 2000; McIntosh and Sen, 2000; Moritz et al., 2000; Silver et al., 2000; Ranero et al., 2000a; von Huene et al., 2000).

Part of the prism relevant to Leg 205 is imaged in the seismic line shown in Figure **F6.** Northeast of the deformation front (shotpoint 3210) the décollement is clearly visible up to 5 km arcward as a boundary separating the underthrust sediment sequence from the overlying poorly structured prism sediments. The detailed analysis of a three-dimensional seismic data set (Shipley et al., 1992) shows that across the 8.5-km-wide coverage of the lowermost part of the prism the décollement structure is quite diverse. Shipley et al. (1992) were able to identify numerous thrust faults mostly in the lower part of the prism acting as possible fluid conduits, but clear tectonic structures are less evident approaching the deformation front. Only one of these faults is imaged offsetting the underthrust sequence (Fig. **F6**) (common midpoint [CMP] 3155) and appears to continue up into the prism sediments.

Prior to Leg 170, the Nicaragua margin was believed to be a non-accretionary margin, whereas Costa Rica was believed to be a site of sediment accretion (von Huene and Scholl, 1991; Shipley and Moore, 1986; Shipley et al., 1992). Leg 170 drilling and subsequent research show no current or recent frontal sediment accretion offshore Costa Rica. The sediment section beneath the décollement at Site 1040 repeats the complete lithology and sequence of the incoming section cored at Site 1039 (Fig. **F5**), allowing little sediment accretion to the front of the prism at present (Kimura, Silver, Blum, et al., 1997). Cosmogenic ^{10}Be, which decays with a 1.5-m.y. half-life, also shows that there has been little, if any, frontal accretion at this site over the last several million years (Fig. **F7**) (Morris et al., 2002). The prism is thus either a paleoaccretionary prism or is composed largely of slumped slope sediments rather than accreted marine sediments. Sedimentological and chemical data (Kimura, Silver, Blum, et al., 1997) are more consistent with the latter interpretation. The thinning of the underthrust section seen between Sites 1039 and 1040 (Figs. **F5, F6**) must then reflect compaction and dewatering, rather than sediment offscraping. As noted earlier, the chemical differences in the arc lavas from Nicaragua and Costa Rica suggest that the entire sediment section is subducting to the depths of magma generation beneath Nicaragua, with the carbonate section dominantly subducting beneath Costa Rica. The seismic and lithologic observations indicate complete sediment subduction past the prism front in both regions. The arc and prism observations can be reconciled if sediments are underplated to the base of the prism beneath Costa Rica or if greatly enhanced subduction erosion occurs beneath the Nicoya segment.

F7. Plot of cosmogenic ^{10}Be, p. 48.

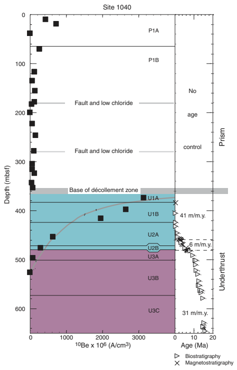

There is evidence for underplating to the base of the prism landward of the Leg 170 and 205 coring area. Christeson et al. (1999) used seismic reflection and refraction data to show stacked velocity duplicates, interpreted as repeated stratigraphic sections because of underplating. The low, but real, ^{10}Be enrichments in the Costa Rican lavas could be explained if the upper 80–100 m of the incoming sediment section was underplated (Valentine et al., 1997).

In addition to evidence for sediment subduction and underplating beneath the Nicoya segment, the seismic stratigraphy of the slope offshore Nicaragua and the tectonic structure offshore Costa Rica indicate extension and subsidence of the margin during much of the Miocene (Ranero et al., 2000a; Ranero and von Huene, 2000; Walther et al., 2000). Multibeam bathymetry along the continental slope displays structures that indicate significant mass wasting offshore Nicaragua and a rugged morphology offshore Costa Rica (Ranero et al., 2000a; von Huene et al., 2000), which is consistent with tectonic erosion and thinning of the overriding plate. These results are further substantiated by Leg 170 coring and postcruise science. Coring at Site 1042, located 7 km landward of the Middle America Trench, encountered a ~30-m-thick sequence of fossiliferous well-lithified calcarenite breccia at a depth of ~4000 meters below sea level (mbsl) (Kimura, Silver, Blum, et al., 1997). Fossil, textural, cement paragenesis, and sedimentological observations document that the calcarenite was formed, brecciated, and cemented in a nearshore setting (Vannucchi et al., 2001). Sr isotope ratios place the depositional age at ~16–17 Ma (latest early Miocene) and establish that the breccia section is stratigraphically upright. It is overlain by ~320 m of unconsolidated slope mud showing the complete Pleistocene to Miocene sequence, where benthic foraminifers indicate the subsidence of the margin from the upper bathyal to abyssal depths (Meschede, 1999b; Vannucchi et al., 2001). Unfortunately, erosion rates over the last several million years are less well constrained. Speculation is that tectonic erosion has been controlled by the roughness of the subducting plate. The thinning of the overriding plate and the continental margin morphology suggest that subduction erosion increases in intensity from Nicaragua to southern Costa Rica (Ranero and von Huene, 2000).

For the purposes of Leg 205, an important result is that the margin offshore Nicoya is not currently accreting sediments and has not done so over the last several million years. The conclusion that all sediments fed to the trench over this time frame have been subducted below Site 1040 greatly simplifies estimating the mass and element fluxes. Specifically, changes in underthrust sediment thickness between Site 1039 and 1040 are due to compaction with underplating farther downdip.

Heat Flow offshore Costa Rica

Heat flow data from the Global Heat Flow Database within the seaward area offshore Costa Rica and Nicaragua are sparse with a typical spacing of 60 to 100 km. However, even with this very limited coverage, a clear trend in the overall picture is very obvious. North of the FZT, heat flow values average ~30 mW/m^2 (about one-third of the expected value from lithospheric cooling after Stein and Stein, 1992) and increase to an average value of ~110 mW/m^2 south of the FZT. Plates north and south of the FZT have approximately the same age, so one would expect them to show similar average heat flow. This indicates that crust south of the FZT, created at the CNS, is close to the expected value from lithospheric cooling, whereas crust north of the FZT is significantly cooler, which means that a substantial amount of its heat is probably being removed by hydrothermal circulation within the crust. This conceptual model still needs confirmation with more heat flow data and hydrogeological modeling in order to understand the driving forces for fluid flow.

A detailed heat flow study prior to Leg 170, focusing on the trench and the prism offshore the Nicoya Peninsula (Langseth and Silver, 1996), confirmed the trend of a cool plate subducting under Costa Rica. Two recent heat flow surveys (TicoFlux I and II) investigated in detail the thermal structure of the incoming plate seaward of the Leg 205 area by mapping heat flow along seismic lines. Three major conclusions can be drawn: (1) small and isolated areas show either very high or very low heat flow, indicative of active recharge or discharge; (2) profiles across the FZT confirm the increase of heat flow as one steps from the EPR-created crust to the CNS-created crust, as suspected from an analysis of the Global Heat Flow Database; and (3) a profile seaward of the deepest part of the trench across major extensional faults shows no indication that these faults act as major fluid conduits. New heat flow values at the prism from northern Nicaragua to southern Costa Rica (*Meteor* cruise 54-2) clearly support the idea that the FZT is a major thermal boundary, not only seaward of the trench but also underneath the prism. One profile runs along the transect of holes drilled during ODP Legs 170 and 205 and coincides with seismic line BGR99-44. Figure **F8A** shows the locations of all seafloor and borehole heat flow measurements along the drilling transect, starting at the trench and up to 34 km away from the deformation front. Data from Leg 170 (Langseth and Silver, 1996) and the *Meteor* 54-2 cruise are projected along this profile. All data sets generally show a similar pattern of an increase from a low heat flow of ~7–15 mW/m² to values of ~20–40 mW/m² passing from the trench to the prism (Fig. **F8B**). Only the extremely low mean value of 6.7 mW/m² at ODP Site 1040 is not confirmed by recent measurements during the *Meteor* 54-2 cruise that showed values twice as high that fit in the general trend of observed heat flow up prism.

F8. Heat flow, p. 49.

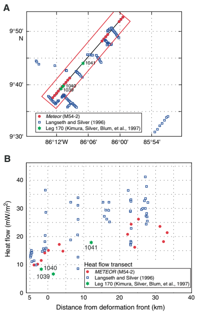

Margin Hydrology

At the Costa Rica subduction zone, coring during ODP Leg 170 and subsequent postcruise studies identified three fluid flow systems: active flow of modified seawater within the upper oceanic crust, updip fluid flow within underthrust sediments, and deeply sourced fluid expulsion along the décollement and through faults in the margin wedge (e.g., Silver et al., 2000; Kastner et al., 2000; Saffer et al., 2000; Chan and Kastner, 2000; Saffer, in press).

The existence of active fluid flow in the oceanic basement of the incoming plate is evidenced by both the heat flow anomalies discussed earlier and the chemistry of pore fluids sampled during Leg 170. Postcruise studies of pore fluid chemistry (Fig. **F9**) show chemical characteristics (e.g., $^{87}Sr/^{86}Sr$) typical of modern seawater in the uppermost sediments. Below this, values depart increasingly from seawater at increasing depth as a result of diagenesis, largely ash alteration. The consequence is that measured pore fluid isotope ratios at a particular depth-age interval are lower than those of seawater at the comparable age, as determined from the paleoseawater Sr isotope curve. The deepest sediments, however, have pore fluid chemistry that trends back toward modern seawater values. This is particularly evident in the Sr isotope profile, where pore fluid values exceed those intrinsic to the Miocene carbonates in a section almost totally lacking terrigenous input other than young volcanic ash. The heat flow anomaly and pore fluid profiles have been modeled in terms of active fluid flow at rates of ~1–5 m/yr (Silver et al., 2000), having a residence time of at least ~15,000 yr. Although certainly model dependent, these results do indicate extensive contemporary flow of seawater to basement and require high permeability horizons thought to be within the uppermost basement based on results from off-axis drilling along the Juan de Fuca and Mid-Atlantic Ridges (Davis and Becker, 1994; Becker et al., 1997, 1998; Fisher, 1998; Davis et al., 2000; Kopf et al., 2000). In addition to cooling the uppermost part of the plate, the flow may further alter the basaltic crust. Any subducted high-permeability horizon may provide conduits for fluids leaving the deeper subduction zone; subduction of altered basalt may

F9. Pore water strontium isotope ratios, p. 50.

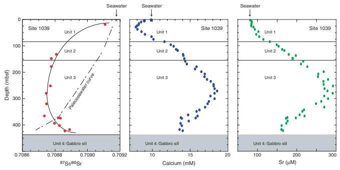

have important implications for volatile transfer and release at greater depths.

The décollement and faults cutting through the margin wedge of the upper plate serve as pathways for updip flow of deeply sourced fluids. Structural observations across the décollement indicate a zoned fault with heavily fractured fault rocks above a ductile plastic zone that may act as an aquitard, segregating the flow systems above and below the plate boundary (Vannucchi and Tobin, 2000; Tobin et al., 2001). At Site 1040, the deformation increases gradually downward and the shipboard structural geologists placed the top of the décollement zone at 333 meters below seafloor (mbsf). The change from brittle to ductile deformation is present at ~355 mbsf, and the base of the décollement is a sharp boundary at 371 mbsf (Fig. **F10**). Pore fluid chemistry studies during and since Leg 170 at Site 1040 show three distinct intervals. Above ~190 mbsf, Li, propane, and Ca concentrations are relatively uniform, as they are again in the underthrust sediments below the décollement. Generally high Li, propane, and Ca concentrations are observed between ~200 mbsf and the décollement, with peaks typically coincident with fault zones. Similar chemical anomalies are also seen along the décollement zone at Site 1043 (~130–150 mbsf). Extremely high Li concentrations are observed along the thrust and décollement at Site 1040 (Fig. **F10**). Enrichments in Ca and Sr, changing Sr and Li isotopic compositions, and K depletion, as well as higher concentrations of thermogenic heavy hydrocarbons (propane to hexane) are also observed. Collectively, these data indicate that some fraction of the fluids sampled along these localized horizons are derived from depths great enough that temperatures are 80°–150°C. The chemical variations shown in Figure **F10** suggest that the zone between 200 and 370 mbsf is heavily infiltrated by deeply sourced fluids; the sharp peaks at ~200 and 350–360 mbsf indicate that the anomalies are supported by relatively recent advective flow. Note that the décollement zone geochemical anomalies approximately coincide with the base of the brittle fracture zone, just above the region of ductile deformation. The composition of deeply sourced fluids, likely derived from the updip limit of the seismogenic zone, may be useful in constraining the mineralogy of sediments at depth and the dehydration reactions that are thought to be important in governing the rheological properties of the subduction interface in the region of seismogenesis. Given that most seismogenic zones will be beyond the reach of even a riser drill ship, development of chemical proxies for "remote sensing" of processes occurring in the seismogenic zone is an important adjunct of Leg 205.

F10. Structures and geochemical anomalies, Hole 1040A, p. 51.

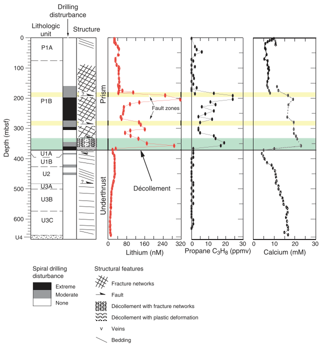

Structural studies indicate a third hydrologic system, which drains fluids from the underthrust sediment section. Results from Leg 170 documented the complete underthrusting of the incoming sedimentary section at the trench, with the important implication that observed changes in sediment thickness and porosity directly reflect the evolution of effective stress. Laboratory consolidation tests, combined with LWD data from Leg 170, show that the subducting sediments are effectively undrained at Site 1043 (Fig. **F11**) (Saffer et al., 2000; Saffer, in press). At Site 1040, the lower carbonate section (Unit 3) remains essentially undrained, whereas the upper hemipelagic units (Units 1 and 2) are partially drained, as shown in Figure **F11.** Pore fluid profiles from sediments immediately below the décollement at Sites 1040 and 1043 show a distinct chemistry from that along the décollement. A Ba spike immediately below the décollement (Fig. **F11**) reflects sulfate reduction in the uppermost underthusting section that mobilizes Ba out of barite

F11. Pore pressures and compaction ratios, p. 52.

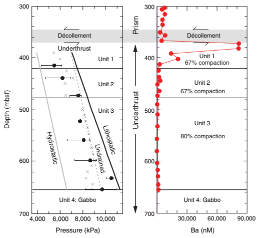

and into the pore fluids. The very low Ba values in the décollement zone itself indicate that these fluids are not primarily draining into the décollement, indicating little, if any, communication between the hydrologic systems above and below the décollement. Other broad anomalies below, and separate from, the décollement also imply updip advective flow of locally derived fluids below the décollement (Kastner et al., 2000).

The differences in pore pressure development downsection reflect nonuniform fluid escape (Saffer et al., 2000; Saffer, in press). More rapid drainage of the uppermost ~100 m (Units 1 and 2) than that of Unit 3 may result from (1) more abundant coarse-grained high-permeability ash layers that focus flow, (2) higher permeability within the hemipelagic sediments, or (3) significant permeability anisotropy within the hemipelagic sediments. The nonuniform dewatering also has important mechanical implications. An inferred minimum in effective stress developed near the top of Unit 3 between Sites 1043 and 1040 results in a mechanically weak horizon and suggests that detachments may form below the décollement there. This is consistent with the downstepping of the décollement 2–3 km inboard from the trench observed in this region (McIntosh and Sen, 2000) and illustrates the role of fluid pressure in mediating structural development. Based on analyses of the underthrust sediments drilled during Leg 170, observed changes in porosity and volumetric fluid sources (in $V_{\text{fluid}}/V_{\text{sediment}}/\text{s}$) range from ~$10^{-12}$/s at the top of the section to ~10^{-13}/s at the base. These values are one to two orders of magnitude larger than those calculated for underthrust sediments at the Nankai and Barbados subduction zones (e.g., Zhao et al., 1998; Screaton et al., in press). This dramatic difference likely reflects higher sediment permeabilities at Costa Rica, resulting in a more active fluid flow system.

Overall, hydrological and geological modeling (e.g., Saffer et al., 2000; Silver et al., 2000) suggests relatively high permeabilities in the oceanic basement, décollement, and underthusting section, with the décollement being locally more permeable than the underthrusting sediments.

SCIENTIFIC OBJECTIVES

During Leg 205, we returned to near the Leg 170 drill sites. Science objectives for Leg 205 had two primary foci. The first was the igneous and alteration history of the basement at reference Site 1253 on the incoming plate. The second was two of the three hydrological systems: in basement at Site 1253, along the décollement at Sites 1254 and 1255, and in the uppermost section of the subducting sediment section at Site 1254. At the prism sites, coring in the fault zones provides an opportunity to integrate structure, fluid flow, and fluid chemistry. These goals were accomplished as described in detail below by limited coring of selected intervals (Table T1), downhole temperature measurements, logging at Site 1253, an extensive shipboard and postcruise analytical plan, the installation of long-term observatories to monitor temperature and pressure, and sampling fluids and gases at key hydrological intervals.

T1. Leg 205 operations summary, p. 75.

Reference Site 1253 Science Objectives

During Leg 205, coring and sampling began at Site 1253 within the carbonates above the sill encountered during Leg 170 and continued through the sill and the previously undrilled sediments below and ~100 m into the lower igneous unit. The scientific objectives to be addressed through coring, sample analysis, and logging at Site 1253 were as follows:

1. Calculate subduction fluxes to the trench. Leg 170 data provide information for the bulk of the sediment section, whereas Site 1253 coring and shipboard analysis added data from the lowermost sediment section, the sill, and the lower igneous unit. Postcruise emphasis will be placed on elements and isotopes of particular interest for evaluating sediment dynamics through the forearc, fluid and element fluxes out of the downgoing plate as it passes through the seismogenic zone, subduction and recycling behavior of carbonate and CO_2 from trench to arc, composition of the subducting igneous basement (fresh and locally altered), and the trench-arc recycling of key tracers for quantifying sediment and oceanic crust contributions to the arc lavas. Leg 205 data will be combined with results from the >500-m penetration of EPR oceanic crust during Leg 206 to provide a more complete picture of the downgoing oceanic crust.
2. Investigate the extent of the igneous sections cored, their origin and tectonic implications, and their contribution to the bulk composition of the subducting igneous crust. Leg 170 encountered a gabbro sill, with trace element characteristics consistent with an origin related to Galapagos activity.
3. Determine the igneous and alteration mineralogy, petrology, and geochemistry in the uppermost 140 m of the igneous section and characterize the original igneous structure therein, using coring and logging data. Use the geochemical data to calculate subduction fluxes. Attention will be paid to low-temperature alteration features that may result from near-trench fluid flow as well as that deriving from ridge-crest and near-off-axis hydrothermal circulation.
4. Collect microbiological samples within the more fractured and veined parts of the oceanic section for shipboard cell counts and preliminary deoxyribonucleic acid (DNA) extractions and postcruise analysis. Contamination testing using perfluorocarbon tracer (PFT) and microspheres was carried out.
5. In conjunction with Leg 170, construct an ash stratigraphy that maps Galapagos and Central American ashes as the plate moves from near ridge to near trench.
6. Determine physical properties in the core and borehole that may affect estimations of igneous composition and lithologic variation or that relate to fluid flow and deformation such as porosity, density, fracture distribution and orientation, and strength. We identified regions of higher fracture density to determine sites for osmotic samplers.

A long-term borehole observatory (i.e., a CORK-II) (Fig. **F12**) was installed at Site 1253 to sample fluids and to monitor temperature and pressure within the uppermost permeable basement. Osmotic samplers were installed at two different levels within the section. The science objectives for the CORK-II installation were to

F12. Schematic of CORK-II installation, p. 53.

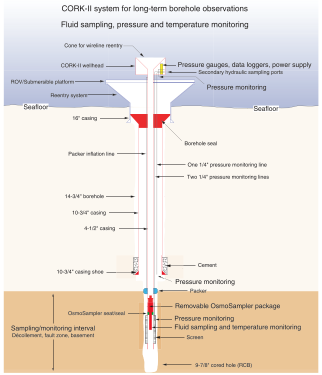

1. Use pressure, temperature, fluid, and gas compositions together with downhole measurements to characterize the fluid and heat

fluxes responsible for the abnormally low heat flow in the vicinity of this site caused by seawater incursion inferred to be in the uppermost basement. Monitoring and sampling will run for 1–2 yr, after which pressure data will be downloaded and the temperature loggers and osmotic samplers will be replaced with instruments designed to operate for 4 yr before recovery.

2. Evaluate the thermal, hydrological, and chemical implications of this extensive fluid circulation for the thermal structure of the uppermost part of the subducting plate, the hydrological pathways available in the shallow subduction zone and beneath the overlying prism, and global element fluxes.

Prism Holes 1254A, 1254B, and Site 1255 Science Objectives

Limited coring focused on an upper fault zone and the décollement; these two fault zones have pore fluid chemical anomalies indicative of advective flow of deeply sourced fluids. Two penetrations of the décollement and good recovery therein allowed more detailed structural analysis at several sites (in conjunction with Leg 170), higher-resolution chemical sampling, and integration of structural characteristics with indicators of fluid flow. Coring results were used to guide installation of a CORK-II to monitor and sample within the area of maximum flow a deeply sourced fluid in the décollement. Together, these approaches plus shipboard and postcruise work will be used to address the following scientific objectives:

1. Make detailed observations of the structural development of the upper fault (Sites 1040 and 1254) and décollement (Sites 1040 and 1254 and Sites 1043 and 1255) that will contribute to a better understanding of the structural development of the décollement zone as a function of position along and within the plate boundary fault zone, lithologic properties, and fluid flow characteristics.
2. Determine physical properties, including permeabilities, of the décollement horizon from further structural experiments on whole-round samples to constrain hydrological modeling and permit integration of fluid flow and deformation models.
3. Determine hydrocarbon chemistry within the fault and décollement zone sediments and major and minor cation and anion concentrations and isotope ratios in pore fluid profiles from fault zone and décollement whole rounds. The advective spikes and diffusive gradients derived therefrom will be evaluated against the structural features in the cores and also compared to profiles measured during Leg 170 to evaluate possible heterogeneity.
4. Collect whole-round samples from the upper fault zone and décollement under appropriate conditions for postcruise microbiological investigations to determine the resident microbial ecology of the zone for comparison to eventual microbial experiments on fluids collected from the décollement. Contamination tests have been conducted using microspheres only to detect any possible chemical contamination of pore fluids by the PFT solution.
5. Install a CORK-II at one site into the zone of maximum fluid flow to determine pressure, temperature, and composition of flu-

ids and gases along the décollement and evaluate any possible changes through time for hydrologic modeling. OsmoFlowmeters were included in an attempt to constrain fluid flow rates through the sampler screen. This same data set will constrain the flux of elements out of the downgoing sediment section along the décollement to evaluate the role of fluid egress on element fluxes to the ocean and its corollary, changing composition of the residual slab because of fluid loss.

6. Use selected elements, element ratios, and isotopic compositions in the fluids from the décollement, both from whole rounds and ultimately CORK-II osmotic samplers, in an attempt to constrain dehydration reactions at the updip and, perhaps, downdip limits of the seismogenic zone.

SITE SUMMARIES

Site 1253

Site 1253 is located ~200 m seaward of the deformation front in the deepest part of the Middle America Trench (Figs. F3, F13). Operationally, one primary goal for this site was to recore the sediments immediately above the sill encountered during Leg 170, drill and core for the first time through the sediments below the sill, and core >100 m into the oceanic section. The other major task was to install a CORK-II observatory in the deep igneous section, where coring and logging were used to identify depths at which to set the packer and osmotic fluid and gas samplers.

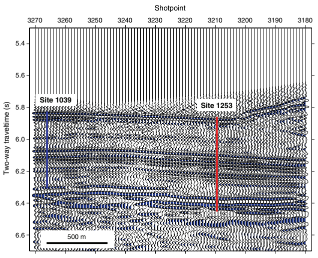

F13. Multichannel seismic profile BGR 99-44, p. 54.

There were two primary science objectives for this site. The first goal was to determine the bulk composition and distribution within the incoming plate of key element and isotopic tracer; this would provide a baseline in physical, mineralogical, and chemical characteristics against which changes during shallow subduction processes may be measured or inferred. They also provided a starting point from which to examine the recycling from subduction trench to volcanic arc (or deeper mantle) of important components such as CO_2. The second major objective at this site was to investigate the hydrology and thermal structure of the igneous section entering the trench. This objective will be addressed using temperature and pressure data and fluid and gas samples recovered from the observatory 1–2 and 5–6 yr postcruise. Interstitial water chemistry analyzed shipboard during Leg 205, together with that from Leg 170, provides evidence for contemporary flow of seawater at depth at both reference sites.

The seismic record (Fig. F13) in the vicinity of Hole 1253A (CMP 3210) images the sedimentary sequence of middle Miocene age with a clear change in seismic reflectivity at ~6.1 s TWT. This represents the top of the calcareous Unit U3 (Kimura, Silver, Blum, et al., 1997) at ~180 mbsf. Beneath the sedimentary sequence, the strong reflector at 6.34 s TWT images the top of a gabbro sill as revealed by drilling results from Leg 170 at Site 1039. The coherent reflection pattern below the top of the sill is difficult, if not impossible, to interpret below the drilled depth of 600 mbsf.

At Site 1253, we drilled one hole that was partially cored and into which we installed a long-term hydrologic borehole observatory. After setting a reentry cone and 16½-in casing into the seafloor, we reentered this hole with the rotary core barrel (RCB) and drilled without coring to

~370 mbsf. RCB coring below 370 mbsf penetrated 30 m of calcareous and locally clay-rich sediments with intermittent ash layers (average recovery = 75%) before encountering a gabbro sill between 400 and 431 mbsf (average recovery = 74%). Below the sill was ~30 m of partially lithified calcareous sediments with intermittent ash layers (average recovery = 20%). This interval was followed by coring ~140 m into a second igneous unit (average recovery = 75%), with local zones of 30%–50% recovery.

After coring, operations focused on preparing the hole for logging and CORK-II installation. The hole was opened to 14¾ in; 10¾-in casing was installed to a depth of ~413 mbsf and cemented in place to inhibit communication between the borehole and the formation. After drilling out the cement shoe and drilling a rathole with an RCB bit, we logged the hole. Because we conducted operations at or very near Leg 170 drill sites where LWD was conducted, our logging focused on the igneous section at Site 1253. Here, we ran the triple combination (triple combo) and Formation MicroScanner (FMS)-sonic tool strings to determine physical properties, fracture distribution, and structure of the basement rocks. After an initial logging run encountered an impassable bridge in the shallow sediment section, casing was run into the uppermost part of the sill to stabilize the hole for subsequent CORKing operations. The subsequent logging run encountered a bridge at 530 mbsf that limited the triple combo and first FMS-sonic run to the interval between 530 and 413 mbsf; on a second pass, the FMS-sonic tool string passed below the bridge and the hole was logged upward from 564 mbsf. A miniaturized temperature logger was run along with the Lamont-Doherty Earth Observatory Temperature/Acceleration/Pressure (TAP) tool.

After logging, we assembled the CORK-II components, including a 4½-in casing screen, casing packer, and casing made up to the instrument hanger. The entire assembly was then lowered into the hole and latched in to seal the borehole outside of the 4½-in casing. The OsmoSampler with integral temperature sensors was lowered through the center of, and latched into the bottom of, the 4½-in casing. The final operation was to inflate the packers and shift spool valves that would connect the CORK-II pressure monitoring system to the formation, which would completely seal the zone to be monitored. Problems with the go-devil used for this step made it difficult to determine whether the packer had inflated or the valves had turned for pressure monitoring. *Alvin* dives since then have confirmed that the installation is fully operational. Three absolute pressure gauges including a data logger are installed within the instrument hanger head. One sensor monitors pressure within the sealed-off fluid sampling zone at the bottom of the hole; one monitors pressure variations present within the borehole above the sealed-off section; and the third sensor provides seafloor reference pressures. One additional sampling line extends from the CORK-II head all the way down to the screened interval below the packer and is available for future pressure/fluid sampling purposes. The specifics of the CORK-II installation, relative to the structure and petrology of the igneous sections, are discussed in more detail below.

Lithostratigraphy and Sediment Geochemistry

Sediment coring began at Site 1253 at 370 mbsf, where nannofossil chalks with minor clay interlayers were recovered, closely similar to those at Leg 170 Site 1039. Other significant grains identified are siliceous sponge spicules, diatoms, and zeolites derived from the degradation of volcanic glass shards. Volcanic detritus (glass, altered glass, and mineral fragments) is ubiquitous, varying between ~3% and 10% of the total. Tephra layers (<1% of total stratigraphic thickness) are typically thin (<5 cm), with mafic layers accounting for >70% of the layers identified. A thick (8 cm) siliceous white tephra was recovered at 398.8 mbsf. Diagenesis has resulted in moderate lithification in the section, except immediately above the gabbro sill, where the sediment is much more clay rich, laminated, and lithified. This section (Core 205-1253-4R) is less calcareous (<2 wt% $CaCO_3$). Clays and zeolites form increasingly large volumes of the sediment in the last 3 m above the gabbro sill, and quartz from diatom and/or spicule opal recrystallization to quartz is seen as thin chert layers at 395.4 mbsf (interval 205-1253A-4R-1, 53–61 cm). Below the gabbro sill, in Core 205-1253A-10R, less lithified nannofossil chalks were recovered. These are identified as the same lithologic unit as above the sill, but they are dominated by a clastic granular limestone, defined as packstone with clay. Minor amounts of baked sediments, usually inferred to be out of place, were recovered within and below the gabbro sill. Bulk sediment chemistry, by inductively coupled plasma–atomic emission spectroscopy (ICP-AES), largely map the minor variations in lithology, with SiO_2 increasing and CaO and Sr decreasing in the more clay-rich interval immediately above the sill. The TiO_2 and Al_2O_3 contents in the sediments are largely controlled by the ash contribution; relatively constant Ti/Al ratios through the calcareous and clay sediment sections suggest relatively homogeneous amounts of volcanic detritus throughout the section. Baked sediments have chemistry similar to the dominant lithology. No appreciable increases in Fe, Mn, or transition metal concentrations were noted above the sill, in contrast to the increases in Cu, Ni, Zn, and V observed for ~80 m above the sill at Site 1039.

F14. Logging summary, p. 55.

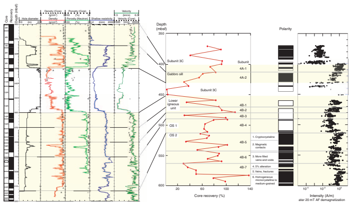

F15. Subunit 4A features, p. 57.

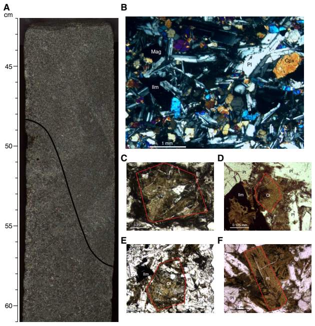

Biostratigraphy

Because of the small amount of new sediment recovery expected during Leg 205, the shipboard science party did not include a micropaleontologist. Samples were taken for a shore-based participant. Results are expected to help constrain the ages of the gabbro sill and the lower igneous unit.

Igneous and Metamorphic Petrology

Coring at this site penetrated two separate igneous subunits (Fig. F14). The upper subunit is a gabbro sill (Fig. F15) and is similar to that encountered at Leg 170 Holes 1039B, 1039C, and 1040C. The sill (Subunit 4A) has been further subdivided tentatively into two subsections, Subunits 4A-1 and 4A-2, based on the distribution of voids, veins, grain size variation with depth, and the proportions of plagioclase to pyroxene. The lower igneous subunit (Subunit 4B) has been tentatively subdivided into seven subsections using the same criteria. Both the upper and lower igneous sections contain plagioclase and clinopyroxene phenocrysts, with rare olivine, orthopyroxene, ilmenite, and magnetite (Fig. F16). Subunit 4B, particularly below 513 mbsf, is more glass rich and more altered. Phenocrysts are set in a groundmass that typically varies between microcrystalline and fine grained, with occasional medium-grained horizons. A 1.3-m-thick interval of cryptocrystalline material is present at 513 mbsf (Fig. F17), where larger amounts of glass

F16. Zeolites in the upper part of Subunit 4B, p. 58.

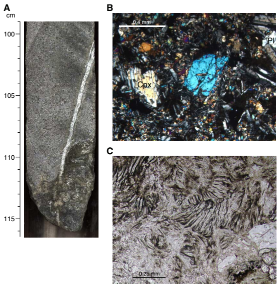

F17. Cryptocrystalline groundmass, p. 59.

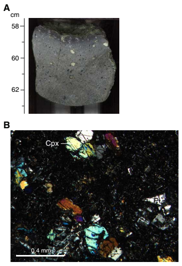

and a greater degree of alteration are observed. The petrologic data suggest that Subunit 4B is either a sill complex with multiple intrusions or a series of thick and slowly cooled lava flows. Its possible that changes in petrology and physical properties at ~513 mbsf mark the change from a sill complex to basement; postcruise dating and detailed analysis will be necessary to evaluate the two possible origins of Subunit 4B. Note that some characteristics of Subunit 4B are similar to those seen in some horizons recovered during Leg 206 coring, which intersected thick ponded lava flows (Wilson, Teagle, Acton, et al., in press).

Discrete alteration is highest at the tops of the subunits and generally higher in the lowermost cores, but is generally low (1%–5%) overall. Veins sampled below 485 mbsf in Subunit 4B contain up to ~11 wt% carbonate, although quantification is difficult because vein material is mixed with various amounts of igneous rock. Diffuse alteration of the bulk rock, in the form of zeolite formation and clay replacement of minerals and glass, ranges from ~10%–50%, with higher levels of alteration seen below 513 mbsf. Chemically, all rocks from both subunits are of basaltic composition (46–49 wt% SiO_2 and 6–9 wt% MgO), with compositional variation in part due to olivine, clinopyroxene, and plagioclase fractionation. Variations in elements such as Ti, V, Ba, and Zr indicate that Subunits 4A and 4B are not comagmatic and possibly could have been derived from different mantle sources. Chemical and isotopic analyses beyond those available shipboard will be necessary to determine whether these mantle sources are associated with the Galapagos hotspot, the EPR, or both.

Structural Geology

The most evident feature of the sediments above the magmatic intrusion (in cores firm enough to preserve original structures) is the tilted bedding with 30° average dip; paleomagnetically reoriented dip azimuths cluster at 221°, similar to the geometry observed at Sites 1039 and 1040. Small normal faults perpendicular to bedding, with millimeter-scale offsets are common throughout, as are pressure solution structures 3–10 cm long. The close association of reworked pelagic sediment in the lower part of Subunit U3C, westward-tilted bedding, and the magmatic intrusion suggest that the lowermost part of the sedimentary section was deformed during the gabbro emplacement. At Site 1253, the sediments do not exhibit subhorizontal shortening related to incipient subduction, despite the location of the deformation front only several hundred meters to the east.

F18. Petrologic summary, p. 60.

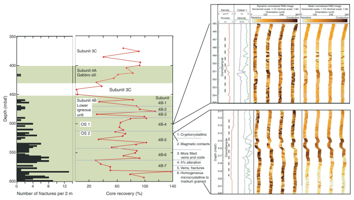

The igneous units were carefully analyzed with respect to the CORK-II experiment and to provide data for comparison to the FMS data (Fig. F18). A sediment/gabbro contact was recovered in interval 205-1253A-27R-1, 1–6 cm, and it dips 72°, although this piece sits at the top of the core and may not have been recovered in place. The igneous units are commonly cut by magmatic veins. Dilational joints are also frequent, usually filled with a film of green minerals (clay and zeolite?), and are rarely present as open fractures (Fig. F19). The paleomagnetic reorientation of the fractures to the real geographical coordinates has been done with particular care; some joints share preferred orientations with magmatic veins, but many do not. Overall, fracture density increases with depth (Fig. F18). Brittle shear zones, represented by en echelon Riedel shears, are common in the lower part of the deeper igneous unit (Core 205-1253A-36R and below) and usually show a reverse sense of movement.

F19. Zeolite as cavity fillings, p. 61.

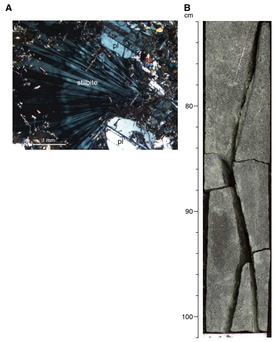

Physical Properties

Variations in physical properties correlate with major lithologic changes between sediments and igneous units (Fig. **F14**). A limited number of measurements indicate decreased porosity and increased grain density and *P*-wave velocity within sediments immediately above and between the igneous units; these differences may reflect alteration (recrystallization) and porosity reduction caused by emplacement of the igneous units.

Clear trends in the physical property data are (1) the small but systematic increase in velocity, bulk density, and grain density and decrease in porosity within the lower igneous unit and (2) the higher natural gamma radiation (NGR) in the upper igneous unit and the clear shift in NGR emissions at 512 mbsf within the lower igneous unit. The cause of these trends in porosity, density, grain density, and velocity with depth in the lower igneous unit is unclear. The differences in NGR emissions suggest chemical differences between and within the igneous units, which may reflect primary compositional differences or varying degrees of alteration within igneous units that were initially chemically similar. The fact that the trends in porosity, density, and velocity are not correlated with the NGR trend suggests that the processes that control porosity, density, and *P*-wave velocity are separate from the chemical or lithologic processes that affect the NGR emissions.

Paleomagnetism

Shipboard magnetic studies on the archive-half sections and discrete samples (Fig. **F14**) established a reliable set of magnetic polarity changes and investigated rock magnetism, especially mineral composition and the domain state of magnetic minerals in the sediments and igneous rocks. The small amount of coring above the sill yielded at least two reversed polarities consistent with those seen in Holes 1039B, 1039C, and 1040C during Leg 170. Sediments below the sill generally showed negative polarity, but low recovery and high drilling disturbance preclude identification of a magnetic chron or subchron. Good recovery in the gabbro sill allows identification of several intervals of normal and reversed magnetic polarity. In the lower igneous unit, the upper part (between 450 and 513 mbsf) is primarily within an interval of reversed polarity. Two brief intervals of possibly normal polarity are identified, but discrepancies between archive-half and discrete sample results preclude firm identification. Below this depth, multiple intervals of normal and reversed polarity are observed. Postcruise age dating will be necessary to provide an absolute framework for this chronostratigraphy. Saturation isothermal remanent magnetization and Lowrie's test of the sediments show three separate unblocking temperatures, interpreted to reflect the presence of goethite, pyrrhotite (or griegite), and magnetite. In the igneous section, magnetization is often unstable and appears to reflect largely multidomain (>100 µm) magnetic minerals, presumed to be magnetite. Intervals of more stable magnetization and high magnetic intensity are observed at 400 mbsf in the upper unit and at 462–474, 513–523, and 572–593 mbsf in the lower unit.

Inorganic Geochemistry

Interstitial water chemistry of sediment pore fluids was used to investigate in situ diagenetic reactions and the possibility of fluid flow in basement (Fig. F20). Several features in the pore water chemistry suggest a role for enhanced ash alteration and associated authigenic mineral formation above and below the sill. Higher Na and much lower K and Si are observed just above the sill, and the Ca and Sr gradients remain constant at this depth. Cl concentrations are very slightly freshened (1.5%) relative to seawater, which may reflect opal-A or clay dehydration reactions immediately above the sill. The implied liberation of Na, Ca, and Sr to the fluids suggests ash alteration and carbonate recrystallization. The sharp decrease in K and Si is consistent with the uptake of these liberated elements via the authigenic formation of clays, zeolites, and quartz, also observed lithologically. Just below the sill, the Mg concentration in the fluid is quite low, consistent with the authigenic formation of more Mg-rich clays associated with ash alteration. Clear overall gradients with depth are noted for Ca, Sr, SO_4^{2-}, Si, and Li. The gradients parallel those measured during and after Leg 170 (Kimura, Silver, Blum, et al., 1997) but are shifted deeper by ~40 m, thus maintaining the same depth relationship to the top of the sill. The gradients trend toward values typical of modern seawater in the intervals just above and below the sill.

F20. Pore fluid chemical data, Legs 205 and 170, p. 62.

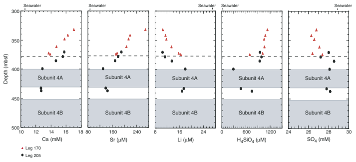

Organic Geochemistry

Organic geochemistry at this site reflects the low heat flow of the incoming plate, with all hydrocarbon concentrations measured for shipboard safety requirements being below the detection limit of the gas chromatographs. Calcium carbonate concentrations in the sediments above and below the sill range from 32 to 65 wt% and overlap those of Site 1039, except in the laminated, clay-rich sediments just above the sill, where values drop to <2 wt%. $CaCO_3$ in the igneous rock is low (<0.4 wt%, except in veins), even in the top and bottom of Subunit 4A and the top of Subunit 4B, immediately adjacent to the sediment section. Veins below 485 mbsf typically contain carbonate (<11 wt%), where some of the differences may be due to variable dilution with matrix igneous material. Total organic carbon is low, and frequently below detection limit, throughout. Sulfur concentrations are low in the sediment sections and near zero in the igneous section, except for one vein sampled at 546.1 mbsf.

Microbiology

Sediment whole rounds (5 cm) were taken for contamination testing (microspheres and PFT) and postcruise microbiological measurements (adenosine-5′-triphosphate [ATP] assay, cell counts, and DNA extractions and analysis). As expected with RCB coring in partially lithified sediments, contamination was significant and variable. In the igneous section, veined intervals were taken as whole rounds (up to 40 cm) and split under sterile conditions. Aliquots will be used for DNA extraction and analysis, culturing experiments and cell counts, fluorescent in situ hybridization studies, and for studies of mineral alteration and chemical change associated with microbial activity. Contamination tests, although difficult to use quantitatively, indicate that the tracers were delivered to all but one cored interval. Interior tracer concentrations are variable, but microsphere concentrations are lower to very low in the interiors.

Downhole Measurements

At Site 1253, the Davis-Villinger Temperature-Pressure Probe (DVTPP) was deployed twice in an attempt to determine the in situ temperature and pressure of the formation. The first measurement was performed directly beneath the casing of the reentry cone at a depth of 60 mbsf; the second was at a depth of 150 mbsf. Prior to these measurements, the bottom water temperature was determined using a high-resolution and calibrated miniaturized temperature data logger (MTL) (Pfender and Villinger, 2002) attached to the video system during reentry, giving a bottom water temperature of 1.989°C at Site 1253. At Site 1039, the bottom water temperature was 1.81°C, as measured by two different tools (water-sampling temperature probe and Adara). The cause of this difference is not clear. The MTL was also affixed to the triple combo logging tool near the TAP tool and run during logging. Unfortunately, thermal changes attributed to the curing of the cement used to tag the casing to the formation created a large signal visible in the temperature record in the upper logged interval, and temperature differences recorded between the two runs indicate that equilibrium formation temperatures had not been attained. The two DVTPP runs encountered difficulties with electronic noise and excessive tool motion, precluding their use to provide high-quality temperature or pressure measurements at this site.

Downhole Logging

The hole was logged upward with one pass of the triple combo and one pass of the FMS tool string from 530 mbsf to the bottom of the casing shoe at 413 mbsf (Figs. F14, F18). On the second pass, the FMS slid past the obstruction at 530 mbsf and the hole was logged upward from 564 mbsf, where a second bridge was encountered. Measured inclination of the hole was very small (0.5°–1.6°). The caliper data indicate that the hole diameter in the logged portions of the upper and lower igneous units (423–431 and 461–561 mbsf) was relatively uniform, ranging mostly between 10 and 12 in. Thin intervals of increased hole diameter are present at 482, 485, 487–489, and 502–504 mbsf. The caliper reached maximum extension between 435 and 461 mbsf, corresponding to the sedimentary section between the igneous units.

The logs can be clearly separated into three intervals on the basis of obvious changes in hole diameter, velocity, resistivity, bulk density, and porosity, corresponding to the upper igneous subunit (Subunit 4A; gabbro sill), the sediments below, and the lower igneous subunit (Subunit 4B) (Fig. F14). In the logged part of sill (413–431 mbsf, with a 14¾-in hole above 423 mbsf and a 9⅜-in hole below), porosities are low and densities, resistivities, and *P*-wave velocities are high. In the sedimentary section of enlarged borehole (431–461 mbsf), high porosities and low bulk densities, resistivities, and *P*-wave velocities identify sediments. A return to high bulk densities, resistivities, and *P*-wave velocities at 461 mbsf indicates the top of the lower igneous subunit. The logs better identify the exact depth of the lower igneous subunit than do core depths because of partial recovery and the standard curatorial practices of moving any recovered material to the top of the core. The NGR intensity is distinctly higher in Subunit 4A than in the sediments and Subunit 4B. Natural gamma logs are not available below 513 mbsf, where NGR emissions measured on cores using the multisensor track

(MST) suggest a small increase in K, U, or Th concentrations in the lower part of the lower igneous subunit.

The logging data identify a change in the character of the resistivity and *P*-wave velocity logs in Subunit 4B at ~491–493 mbsf. Above this depth in the lower subunit, values are relatively homogeneous; below, the logs have similar average values but a more spiky character. FMS images indicate a change in character at a depth of ~508 mbsf. Above that depth, conductive features are generally discontinuous. Below, more closely spaced, thin, near-horizontal to slightly dipping conductive features are present in several intervals that are separated by intervals of poor images and irregular borehole size that could be fractured material or sediment interlayers. Intervals of decreased bulk density but no corresponding velocity decrease may indicate a fractured interval rather than sediment interlayers, which should cause a velocity decrease. Based on the bulk density and sonic logs, potential fractured intervals are inferred at 466–468, 484–486, 490–493, and 506–508 mbsf. Sediment interlayers thinner than the vertical resolution of the sonic tool (107 cm), would not be clearly distinguishable in this log, but the general high density and low porosity in areas of smaller borehole diameter preclude the presence of any significant sediment layers.

FMS images can be used to characterize structure and fabric in the igneous units. The gabbro sill (Subunit 4A) between 419 and 426 mbsf exhibits a blocky texture with an ~0.5-m size to the blocks. Between 426 and 432 mbsf, the formation appears more massive with thin conductive features at a 0.5- to 2-m spacing, although it is difficult to trace the conductive features across the four FMS pads. At the very top of Subunit 4B (463–467 mbsf), curved conductive features (fractures or irregularities in the borehole wall) are common. Between 467 and 493 mbsf, the formation appears more massive to blocky, with 0.5- to 1-m spacing between thin conductive features. These conductive features can be clearly traced across the four pads only between ~472 and 478 mbsf. Between 487 and 493 mbsf, irregular to curved vertical conductive features are present, representing possible fractures or irregularities in the borehole wall. From 493 to 498 mbsf, conductive features are rare, becoming more common again between 498 and 508 mbsf. At 508 mbsf, the character of the FMS image changes to more closely spaced conductive features (<0.5-m spacing). In rare cases, such as at 513–514 mbsf, these conductive features can be traced across the four pads and suggest a low dip angle. Image quality between 514.5 and 518 mbsf is poor because of an enlarged borehole. Relatively low (3800–4000 m/s) *P*-wave velocities and low (5–15 Ωm) spherically focused resistivities occur at similar depths. Below 518 mbsf, the layered character returns but the absolute value of resistivity increases. Imaging is poor from 525 to 527, from 534 to 539, and from 542 to 555 mbsf. From 539 to 541 and 555 to 563 mbsf, the image is characterized by more closely spaced (<0.5 m), thin, nearly horizontal conductive features. These conductive features appear to dip to the southwest. The static FMS images indicate that both intervals have high resistivity. Therefore, it appears unlikely that these are sediment layers.

Synthesis Topics

Fluid Flow in the Incoming Plate

As at Site 1039, 1.4 km to the west, interstitial water chemistry determined at Site 1253 is also indicative of fluid flow in or below Subunit 4B, where the chemical composition of the fluid is inferred to approach values typical of modern seawater. Figure **F20** shows depth profiles for major, minor, and biogeochemical components determined shipboard in the sediment interval above and below the sill. In the limited sediment interval cored, Site 1253 profiles for Ca and Sr mimic those at Site 1039 (Fig. **F20**). High Ca values (~18.5 mM) seen at ~300 mbsf at Site 1039 likely reflect the effects of mafic ash alteration, which liberates Ca. Mg calcite and dolomite production are also suggested by Mg and Mg/Ca profiles at Site 1039 (Kimura, Silver, Blum, et al., 1997). In the pore waters from the deeper sediments at Site 1253, Ca and Sr decrease by ~20%–30%, toward, but not to, values typical of seawater. A similar magnitude change is seen in the Si content of the pore fluids above and below the sill, excluding the exceptionally low values seen at the immediate boundary with the sill (where quartz precipitation was noted). Li contents increase by ~60% over the lowermost 30 m of the section above the sill. Sulfate concentrations in the pore waters from Site 1253 are relatively uniform (27.2–28.6 mM, with no clear depth variation) and nearly of seawater composition. This contrasts with values of 12–20 mM measured higher in the section at Site 1039. These gradients are in directions opposite to those expected for most biogeochemical and fluid/rock reactions in deep siliceous and calcareous sediments at either low or elevated temperatures, which would be expected to reduce sulfate and to release Si, Ca, and Sr while consuming Mg and Li. The gradients observed at Site 1253, like those at Site 1039, suggest communication with a fluid of nearly seawater composition presumably flowing at depths below those from which interstitial waters have been recovered. At Site 1039, residence time calculations based on Sr and Li isotopes and concentrations (Silver et al., 2000) indicate that the gradients toward seawater are maintained by flow within the last 15–20 k.y. The gradients at Site 1253 are closely similar to those at Site 1039, supporting an argument for recent flow here also, which may have extracted heat from the plate to produce the unusually low heat flow in this region. The nature of this large regional-scale flow system, presumed responsible for the large heat flow anomalies as well as the chemical gradients, remains enigmatic; the CORK-II was installed at this site in hopes of providing necessary new information for better understanding the flow system.

Igneous Stratigraphy

The petrology of the igneous units can be combined with paleomagnetic and rock magnetism studies and logging results to better understand the nature of the two units and their internal structure (Fig. **F14**). Paleomagnetic results show that the sill (Subunit 4A) spans several polarity reversals, implying multiple pulses of magma intrusion, although the elapsed time cannot be evaluated until age dating is completed postcruise. Magnetic intensity is highest at the top of the sill, indicating more stable magnetization, probably because of the presence there of finer-grained magnetite than at deeper levels in the sill. The petrologic boundary between Subunits 4A-1 and 4A-2 approximately corresponds to a polarity reversal boundary. Subunit 4A-2 is composed entirely of microcrystalline gabbro. Logging results show a large hole diameter at the top of Subunit 4A-2, which corresponds to the 14¾-in hole drilled to provide a rathole for the casing installation. Seismic velocity and shallow resistivity (considered more reliable in the igneous units; see **"Downhole Logging,"** p. 22) are relatively high and uniform, and the cores recovered are massive in appearance, breaking into large pieces (see **"Site 1253 Visual Core Descriptions"**). At the base of the sill, recovery drops, the hole size increases, and velocity and resistivity decrease in general and exhibit a more spiky character, suggesting that fractured rock is present or possibly thin (<1 m) sediment interlayers.

The lower igneous subunit (Subunit 4B) begins at a depth of 450 mbsf in the core reference frame, which was used for petrologic and paleomagnetic work, and at ~460 mbsf in the logging data. A depth of 460 mbsf for the top of Subunit 4B is considered more reliable, given the very low recovery at the top of the subunit and the standard curatorial practice of moving all recovered material to the top of the core. Subunit 4B was subdivided into seven subsections, using the same criteria used for Subunit 4A. Within each subsection, multiple alternations between microcrystalline and fine-grained material may indicate the presence of multiple cooling units. Subunits 4B-1 through 4B-3 all formed during what may be a single reversed polarity interval, although dating is required. Magnetic intensity is again high at the top of Subunit 4B and decreases with depth. The logging data show that Subunits 4B-1 through 4B-3 are characterized by high and relatively uniform resistivity and *P*-wave velocity. There is a marked increase in resistivity at the top of Subunit 4B-4, which corresponds to a short massive interval that was drilled very slowly (0.75 m/hr) with high recovery. In this interval, conductive features are rare in the FMS data (see **"Downhole Logging,"** p. 22). There is a hint of increased *P*-wave velocity at and below this interval, seen in the logging data and as measured in the cores. From ~490 mbsf to the base of the logged section, the borehole character becomes more heterogeneous, with intermittent highs and lows in resistivity and seismic velocity. Below 508 mbsf, FMS images change to more closely spaced conductive features, which are continuous across all four pads at rare intervals, such as 513–514 mbsf. This is an interesting depth, as it corresponds to a thin layer of rock with true basaltic texture and a return to high magnetic susceptibility, similar to that seen at the top of the sill and the top of Subunit 4B, and interpreted as indicating single-domain (<100 µm) magnetite. Below this depth, several clear sets of polarity reversals are seen, indicating multiple periods of magmatic activity. The MST natural gamma measurements on the core suggest increased K, U, or Th concentrations in this lower part of Subunit 4B. Glass is more abundant below this depth, discrete and diffuse alteration is more extensive, and carbonate-bearing veins are present. Despite these differences, the generally microcrystalline and fine-grained material below this depth shares many textural, mineralogical, and chemical similarities with the overlying sections.

CORK-II Installation

Details of the core and borehole at the levels of the CORK-II installation in Hole 1253A are shown in Figure **F21,** with the petrological and structural character of key depths as shown in Figures **F14** and **F18.** The center of the packer was set at ~473 mbsf, with the inflatable element being between 471.5 and 475.5 mbsf. The cores indicate that this is an interval of high recovery of massive rock with relatively few fractures. The logging results (see **"Downhole Logging,"** p. 22) show this to be in an area of relatively uniform physical properties (high resistivity, bulk density, and *P*-wave velocity). Interpretation of FMS images indicates a massive-blocky formation, with 0.5- to 1-m spacing between thin conductive features, which can be traced across the four pads. The upper OsmoSampler, located inside a 7.35-m-long screen in the 4½-in casing, is set between 496.7 and 504 mbsf (Fig. **F18**). A 2-m pressure screen is located within the casing screen, and a fluid sampling line runs from

F21. Hole 1253A borehole installation, p. 63.

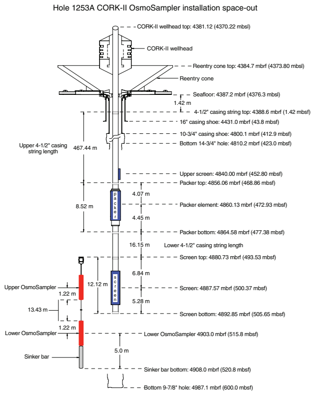

this screen to the CORK-II wellhead. Figure **F18** shows this to be an interval of modest recovery of moderately fractured rock composed of alternating microcrystalline and fine-grained material (see **"Igneous and Metamorphic Petrology,"** p. 18). Logging data in Figure **F14** show this to be an interval of generally uniform hole diameter, with minor variations in bulk density and *P*-wave velocity. FMS images show closely spaced conductive features. The lower sampler is dangled in the open hole between 512.1 and 519.5 mbsf. This is again a zone of moderate recovery and fracture density in a cryptocrystalline (basaltic) to microcrystalline part of the section, with relatively high concentration of voids and 10% to locally 50% secondary mineral formation. The logging data (Fig. **F14**) show this to be an interval of decreased resistivity and sonic velocity and variable hole diameter. In the upper part of this interval, FMS images show closely spaced (<0.5 m) shallowly dipping conductive features that are continuous and can be traced across the four FMS pads. The intervals for the osmotic samplers were chosen using a combination of scientific and operational constraints. Originally, the intervals between 513–521 (now OsmoSampler 2) and 560–568 mbsf were targeted, where the latter is a zone of high fracture density and maximum alteration in largely microcrystalline rock. However, the bridge encountered by the logging tools at 530 mbsf restricted the OsmoSampler deployment to shallower levels. The upper pressure screen, located above the packer, was set into the sediments between the two igneous subunits, where sediments collapsing around the screen are expected to make an effective seal. The final installed configuration for this modified CORK-II geochemical and hydrologic borehole observatory is shown in Figure **F21.** For details of the postcruise submersible visit to this site, see **"Postcruise *Alvin* Submersible Visit to Site 1253 and 1255 CORK-IIs,"** p. 36.

Site 1254

Site 1254 is located ~1.5 km arcward from the deformation front at a water depth of 4183 m, close to the holes drilled at Site 1040 during Leg 170 (Kimura, Silver, Blum, et al., 1997). Hole 1254A is positioned ~15 m west of Hole 1040C, and Hole 1054B is ~50 m northeast of Hole 1040C (Figs. **F3, F22, F23**). Therefore, all comparisons to Leg 170 results are to Hole 1040C at Site 1040, as it was the only one that penetrated the décollement and underthrust.

The primary objective of Site 1254 was to investigate a fault zone in the prism, investigate the décollement, and install a long-term observatory for monitoring of fluid flow, pressure, and temperature in the décollement. Results from Site 1040 (Kimura, Silver, Blum, et al., 1997) and seismic data (Fig. **F23**) provided the framework for drilling the sedimentary sequence and the interpretation of pore fluid geochemistry and structure. Site 1040 geochemical anomalies suggest that deeply sourced fluids, perhaps from seismogenic depths, are migrating along the décollement and prism fault. Site 1254 was intended to investigate in detail the structure and geochemistry of these zones and install an observatory in the décollement. Although perturbed by drilling disturbance, high recovery at Site 1254 enabled detailed structure observations (where they were considered reliable) and higher-resolution chemical sampling than was possible during Leg 170. It is also possible to better correlate intervals of maximum inferred fluid flow to specific structural horizons.

F22. Location of Site 1254, p. 64.

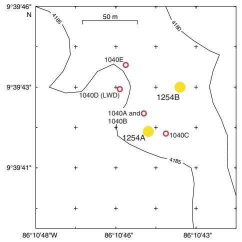

F23. Multichannel seismic profile BGR 99-44, p. 65.

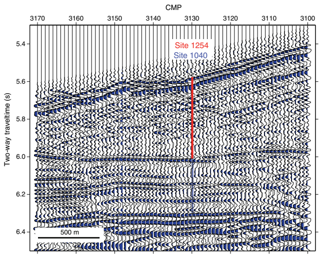

The seismic record (Fig. **F23**) in the vicinity of Site 1254 (CMP 3130) shows no coherent reflections above the décollement. This reflects the general chaotic sedimentary pattern observed in cores from Hole 1254A. The first prominent reflector relevant for drilling objectives is at 6 s TWT, which marks the boundary between margin sediments and the underthrust sequence, cored at 361 mbsf. The prism fault zone is not imaged in the seismic data.

After setting the reentry cone in Hole 1254A, we cored the prism fault zone (150–230 mbsf) and the décollement (300–367.5 mbsf) with the RCB. Recovery averaged ~88% throughout the cored interval. With generally good hole conditions, we planned to case the hole with 10¾-in casing. However, after running the casing to 232 mbsf, the casing could no longer advance and had to be pulled up. Soon it became clear that the reentry cone had hung up on the casing; when the sections that were jammed into the cone were pulled up into the moonpool, it became obvious that the casing had collapsed in the throat of the reentry cone for unknown reasons. Hole 1254B, the second attempt for a CORK-II installation, was offset 50 m to the northeast. However, drilling conditions there prevented us from deepening the hole to >278 mbsf, when the drill string got stuck during several attempts to deepen the hole. Therefore, we decided to install the osmotic fluid sampler in the upper fault zone with the screen located at 225 mbsf; this interval, cored and analyzed in Hole 1254A, was not recored because of time constraints. The depth for the screen was determined by inference from the geochemical results of Hole 1254A, which indicate that deeply sourced fluids containing thermogenic hydrocarbons are present in the target zone. After a successful installation of the 10¾-in casing, the installation of the CORK-II failed as it got stuck ~20 m above the final depth. Attempts to penetrate further probably caused the 4½-in casing to break right below the CORK-II head. Thus, we had to abandon Hole 1254B with ~20 m of casing sticking out of the reentry cone.

In total, we drilled 367.5 m at Site 1254, with 140.5 m cored and 227 m drilled and washed. Because of the nature of the tectonic structures encountered, part of the core was heavily disturbed by RCB drilling, which makes structural and paleomagnetic studies difficult. However, the generally good recovery (average = 89%) allowed extensive whole-round sampling of the cored sections for pore water and organic geochemistry in addition to shipboard sampling for physical property and paleomagnetic studies and provided personal samples for postcruise studies.

Lithostratigraphy

The sedimentary sequence recovered at Site 1254, Subunit P1B after Leg 170, is dominated by structureless and typically unsorted dark greenish gray claystones with variable subsidiary quantities of silt and rare interbedded volcanic ashes, sandstone, and redeposited limestone clasts, spanning a sparsely dated sequence of presumed Pliocene–Pleistocene age (Fig. **F24**). Recovered cores often show moderate to extreme degrees of drilling disturbance; nonetheless, coherent fragments of more lithified sedimentary rocks do indicate that much of the section is either massive or slightly mottled, which is suggestive of moderate bioturbation.

The dominance of clay minerals within the sequence is readily apparent from smear slides, as is the downcore decrease in volcanic ash. Fresh volcanic glass is present at low (<10%) and moderate (<30%) lev-

F24. Summary of results, Hole 1254A, p. 66.

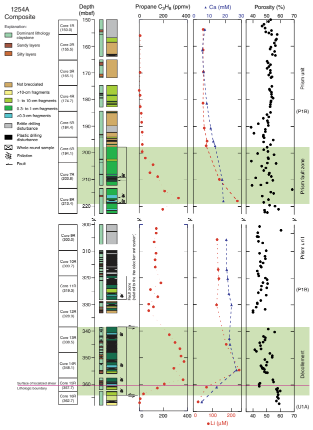

els above 230 mbsf, becoming heavily altered deeper (>300 mbsf) in the section. The continental provenance of the sediments cored in Hole 1254A is clear from the abundance of quartz and feldspar grains and also from the bright, brownish red biotite mica flakes that are found at all stratigraphic levels. The terrigenous nature of the sediments is confirmed by the very low biogenic component (<5%) of the sediment, restricted to occasional nannofossils above 200 mbsf and below 360 mbsf. Below Section 205-1254A-15R-2 (360.62 mbsf), the proportion of diatoms increases sharply (>10%). The appearance of diatoms is considered important for understanding the structure of the forearc prism because the uppermost sedimentary subunit in the subducting Pacific stratigraphy (Subunit U1A) recorded high percentages of diatom abundance (Kimura, Silver, Blum, et al., 1997).

Redeposited blocks of shallow-water peloid limestones, lithified prior to incorporation within mudstones, are found throughout the section, which is consistent with fluidized gravity and debris flows being the dominant mode of sedimentation. The cobbles show evidence for a shallow-water depositional environment, identified by shallow-water bivalve shell fragments and small gastropods.

Compared to the sequence of well-preserved tephra found at ODP Sites 1039 and 1253 on the subducting Cocos plate, there is little well-preserved tephra stratigraphy found at Site 1254. Although occasional thin altered ash layers are recognized, they are rare, typically <2 cm thick, and often completely altered to claystone. Volumetrically, the tephra represents <1% of the total section. Two thicker coherent ash layers are recorded at Site 1254 (intervals 205-1254A-5R-8, 14–20 cm, at 193.49–193.55 mbsf, and 8R-8, 22–65 cm, at 222.37–222.80 mbsf). Both the thicker ashes preserve relatively fresh glass shards and are interpreted to be the product of primary air fall deposition followed by settling through the water column. The base of the tephra recovered in Section 205-1254A-8R-8 was not recovered, resulting in a minimum thickness estimate of 43 cm. Because Site 1254 is ~150 km from the nearest arc volcano in Central America, this thickness at this range indicates that this must have been a very large eruption, comparable to the Minoan Ash from Santorini as the closest analog (Watkins et al., 1978). Major and trace element analyses of this tephra (interval 205-1254A-8R-8, 22–65 cm) characterize its source as being the volcanic arc of Central America.

Structural Geology

Coring at Site 1254 targeted two different structural domains based on Site 1040 results: (1) a fault zone from 150 to 223 mbsf containing fractured sediment and locally steep bedding dips called the prism fault zone and (2) the décollement zone from 300 to 368 mbsf (Fig. F24). A variety of deformation structures is present at Site 1254, and description of deformation was based on breccia size, foliation, hardness of breccia clasts, and the presence of polished surfaces. Because structural observations in poorly lithified material require good quality cores and the recovered cores are sometimes severely disturbed by drilling, it is difficult to distinguish natural from drilling-induced features.

Cores from 150 to 223 mbsf show various degrees of deformation, with the intensity of deformation, particularly brecciation and brittle shearing, increasing downward, reaching a peak at ~219 mbsf. Deformation is discontinuous, being focused along sheared horizons, 20 cm to 2 m thick. These horizons are characterized by stratal disruption, foliated breccia with fragments as small as a few millimeters in length, brittle shear zones, deformation bands, and distinctly inclined bedding. Concentration of deformation structures at ~210 and 219 mbsf documents that this is indeed a fault zone. Riedel shears within a well-preserved foliated breccia (interval 205-1254A-8R-1, 0–24 cm; 213 mbsf) indicate reverse movement. Paleomagnetic reorientation of this shear zone suggests that the fault is a northeast- or southwest-dipping feature, implying that it is a thrust fault (Fig. F24) that strikes parallel to the deformation front.

The second interval cored started at 300 mbsf, and well-preserved structures are observed starting at Core 205-1254A-11R (319.30 mbsf) (cf. Fig. F24). Cores typically show pervasive drilling disturbance, previously described during Leg 170 as "spiraliferous" (Kimura, Silver, Blum, et al., 1997), consisting of a spiral rotation of clay-rich sections. Despite the drilling disturbance, some bedding plane orientations were observed. Bedding and fissility show various dips, indicating heterogeneity of deformation, but the paleomagnetic reorientation shows that they consistently dip northeast or southwest, with strike parallel to the deformation front. The recovered section from 319.30 to 367.50 mbsf is characterized by intense deformation. The deformation is heterogeneous, and brecciation, usually associated with a strong foliation, is the basis for dividing the deformed interval in two zones.

The upper zone from 319.30 to 328.90 mbsf is characterized by generally increasing brecciation with depth, producing fragments of <0.3 cm in length. Foliation is common throughout Core 205-1254A-11R, resulting in a clear alignment of clasts, which are equidimensional but internally strongly foliated. Below 324.15 mbsf (Core 205-1254A-12R) deformation sharply decreases and consolidated and coarsely brecciated sand layers become common. These sandstone layers have steeply dipping laminations and a few web structures. We interpret this well-defined change in deformation intensity to mark the top of a relatively less deformed rock volume that may be the footwall of the fault identified between 319. and 328.9 mbsf and may be related to the décollement zone. This indicates a more articulate structural geometry for the décollement and associated faults than that observed at Site 1040 (Kimura, Silver, Blum, et al., 1997; Tobin et al., 2001).

The upper boundary of the décollement zone at 338.5 mbsf is defined by increasing deformation intensity in Core 205-1254A-13R. The upper boundary of the décollement is difficult to define precisely because the deformation gradually increases in intensity with depth. A sharp increase in deformation is not observed between Cores 205-1254A-12R and 13R. The décollement zone itself is heterogeneous, with a general downward increase of brecciation intensity, fragment aspect ratio, and hardening of the sediments. Despite the good recovery, "spiraliferous" drilling disturbance affects the cores, although less extensively than at Site 1040. Unlike at Site 1040, "spiraliferous" disturbance is not concentrated in the lowermost part of the décollement zone. Brecciation can be pervasive and severe with fragments characterized by polished surfaces; the development of scaly fabric is precluded by the abundant silt and sand in the sediments. From 354.8 to 355.9 mbsf, sandstone layers are brecciated and foliated. At 360.60 mbsf the appearance of diatoms in the sediments marks the lithologic boundary with the hemipelagic Subunit U1A of the underthrust (Figs. F24, F25). The lithologic boundary is present below 50 cm of finely brecciated sand and 10 cm of highly sheared clay indicating a surface of ductility contrast which appears as a major structural discontinuity. The hemipelagic

F25. Boundary between forearc prism and underthrust sediments, p. 67.

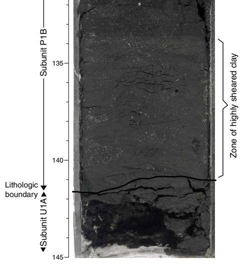

sediments below the lithologic boundary are still intensely deformed and brecciated with aligned clasts showing a strong internal foliation (Fig. F26). The base of the décollement is placed at 364.2 mbsf and is below the lithologic boundary. Deformation starts to decrease and becomes localized below 364.2 mbsf, where intact sediments are separated by 3- to 8-cm-thick brittle shear zones producing gouge or Riedel shears (Fig. F27). These brittle shear zones show exceptionally consistent normal movement and landward dips when reoriented to the geographical coordinates. The hemipelagic sediments above 364.2 mbsf are also deformed by normal faults; a few of them are present as conjugate features. At Site 1254 the décollement zone has a thickness of 25.7 m. Based on this interpretation, the décollement has cut down into the uppermost underthrust section, incorporating a small amount (4.2 m) of Subunit U1A into its base. The complex geometry of the décollement system at Site 1254 contrasts with that described at Sites 1040 and 1043, where the top of the décollement was identified by an increase in brecciation and the lithologic boundary between the prism and the hemipelagic subunit coincides with the base of the décollement.

F26. Deformed hemipelagic sediments, p. 68.

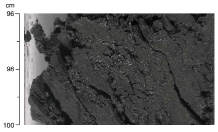

F27. Fault gouge, p. 69.

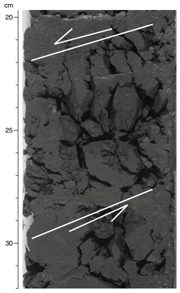

Paleomagnetism

Paleomagnetic measurement on archive-half sections and discrete samples are severely degraded by pervasive drilling disturbance and drill string overprints. Natural remanent magnetization inclinations are still variable after alternating-field demagnetization and make the firm identification of magnetic polarity changes and the construction of a magnetostratigraphy difficult. However, the declination data were useful in carefully selected intervals to reorient core segments for structural interpretation. Demagnetization curves of discrete samples from the prism sediments (Subunit P1B) are often poorly behaved, indicating that they have a very unstable magnetization. Two significant high magnetic intensity and susceptibility zones were observed in the intervals from 184 to 202 mbsf and from 310 to ~350 mbsf. The interval of the first anomaly is close to the prism fault zone at ~210 to 220 mbsf, and the second anomaly is within the décollement zone. These variations suggest changes in concentration, grain size, and chemical components of magnetic minerals related to lithology and/or chemical alteration perhaps related to fluid flow.

Inorganic Geochemistry

A total of twenty 35- to 45-cm whole rounds were sampled at Site 1254 for pore fluid geochemistry. Pore waters were analyzed for Ca, Mg, K, Na, B, Ba, Fe, Mn, Sr, H_4SiO_4, NH_4^+, and SO_4^{2-} concentrations (Fig. F24). Samples taken from between 305 and 366 mbsf were analyzed for Li, Ca, K, Mg, and Na in "real time" on the shipboard ICP-AES to identify the horizon of maximum flow of deeply sourced fluid within the décollement zone based on correlation to nearby Site 1040. The "real-time" chemical analyses were available 2 hr after core recovery and, together with careful observations of hydrocarbon gas concentrations and penetration rate, helped to identify the top of the underthrust section.

The pore fluid salinity in the prism sediments (Subunit P1B) is lower than that of seawater by 20%, and thin excursions of higher dilutions up to a maximum of 29% are present at 218 and ~351 mbsf (13 m from base of the décollement zone). The two main salinity minima also show C_3H_8, Li, and Ca concentration maxima, as well as Mg/Ca, K, and Mg minima. The geochemical excursions between 210 and 218 mbsf are present within a highly fractured interval interpreted as a fault zone, whereas the excursions at ~351 mbsf are located within the décollement zone and appear to coincide with a brecciated, moderately indurated, sandy interval. A small peak in Ca, Li, and C_3H_8 concentrations is present at 330 mbsf and may also be associated with a similar sandy, brecciated interval within the décollement. These data, together with results from the entire interval cored during Leg 170, suggest that fluid has migrated along conduits and permeated the lower half of the deformed wedge. Assuming that the geothermal gradient is ~20°–30°C/km, the source region must be present at >4 km depth because the *minimum* temperature required for thermogenic gas formation is 80°–90°C. The minima in K concentrations at 218 and 351 mbsf further suggests that the deformed sediments have been permeated by a fluid from an elevated temperature source of 80° to 120°C, where the illitization reaction, which consumes potassium, is effective. Also, the K depletion signature of this fluid provides an approximate upper limit to the temperature at the source of ~<150°C, although the data do not preclude the possibility of mixing between fluids from greater depths (>150°C) with shallower fluids along the flow path. Above this temperature, fluid-rock reactions leach potassium from the rocks. Lithium, like K, is partitioned into solids at low to moderate temperatures. At higher temperatures, >100°C but <250°C, Li is released into the fluid phase (Chan and Kastner, 2000). The precise threshold temperatures for the partitioning of Li and K into the solid or fluid phases are as yet unknown. Clay and other silicate mineral dissolution or alteration releases B into the fluid phase; however, clay, especially illite, formation consumes B and may be responsible for the low B concentrations within the deformed sediments. The deeply sourced fluid, however, is not enriched in dissolved silica.

Geochemical excursions in Ca, Li, C_3H_8, K, and Mg are present at ~218 mbsf within the prism fault zone at Site 1254. Similar increases in Ca, Li, and C_3H_8 concentrations, as well as marked decreases in Mg and K concentrations, were observed at an observed prism fault zone at Site 1040; however, the prism fault zone was present between ~180 and 200 mbsf. Therefore, the upper geochemical excursion in Hole 1254A is ~20 m below the same anomaly observed during Leg 170.

The geochemical change at ~218 mbsf separates intervals with pore fluid chemistry typical of clay-rich sediments from those permeated by a fluid from an elevated temperature source, and it seems to be independent of lithology. Bulk sediment chemistry is also relatively homogeneous throughout the entire prism. Changes in pore water chemistry in a lithologically and chemically homogeneous sediment section likely result from fluid advection into the lower half of the deformed sediment section. The chemical changes observed at the base of the fault zone (conduit) at ~218 mbsf are similar to those observed near the bottom of the décollement zone. Except for the biogeochemical components, the pore fluid concentration depth profiles of the underthrust section are similar to those at the reference Site 1039. The concentrations themselves are slightly different in magnitude than those at Site 1039, presumably reflecting the changes in solubilities and dissolution rates of the major sediment components under the new pressure regime as they are underthrust. In contrast to Site 1039, the higher NH_4^+ concentrations and the absence of SO_4^{2-} at the interface between décollement and the underthrust sediments reflect the fact that all the sulfate is reduced at Site 1254 by microbiological activity. Sulfate reduction thus reaches completion in the uppermost few meters of the underthrust hemipelagic section, resulting in somewhat elevated CH_4 concentrations within the zero-sulfate depth interval. These geochemical patterns are similar to those observed in Hole 1040C.

Organic Geochemistry

Volatile hydrocarbon gases were sampled by headspace and vacutainer techniques at a higher frequency than pore water samples to assist in determining the exact depths of the inferred fluid conduits associated with fault zones discovered at Site 1040. Analyses of the vacutainer samples (Fig. F24) show that the gas mainly consists of CH_4 but also contains considerable amounts of higher alkanes up to C_5H_{12}. Methane concentrations were very high ($7–9 \times 10^5$ ppmv) throughout the cored interval but dropped to $\sim 4 \times 10^4$ ppmv directly below the décollement zone at 364 mbsf. Propane, which is a strong indicator of deeply sourced fluids because of its thermogenic origin (>80°–90°C required), shows one peak at 216 mbsf and another in the basal part of the décollement zone at 355 mbsf, with maximum levels of 326 and 370 ppmv, respectively. These high C_3H_8 concentrations correlate with structurally identified fault zones. Similar patterns, at much lower concentrations, were also observed in the headspace gas samples.

Microbiology

Samples for microbiological investigations were taken and either frozen or fixed for postcruise ATP quantification, DNA assessment, or cell counts. Samples of drilling water were frozen to evaluate contamination of cores. The chemical tracer for quantifying microbiological contamination was not deployed during coring at Site 1254 because of concern that the trace element chemistry of the PFT may affect postcruise pore fluid geochemical analyses. Particulate tracer tests yielded fluorescent microsphere counts suggesting very low to no particulate contamination in the interior of the microbiology whole rounds.

Physical Properties

Porosities and bulk densities at Site 1254 (Fig. F24) exhibit trends similar to those seen at Hole 1040C. Variations in porosity and density within the structurally defined décollement zone correlate with core descriptions: in general, zones of lower porosity (40%–45%) correspond to zones characterized by "spiral" deformation interpreted as drilling disturbance; zones of higher porosity (50%–55%) correspond to zones characterized by brecciation. Porosity is also low (42%–44%) between 358 and 361 mbsf, within and adjacent to a zone of localized shear. Porosity increases and bulk density decreases sharply below 361 mbsf across the lithologic boundary between prism sediments and Pleistocene diatomaceous claystone.

Downhole Measurements

We attempted three downhole measurements of formation temperature and pressure, two with the DVTPP at 50 and 200 mbsf and one at 150 mbsf with the Davis-Villinger Temperature Probe (DVTP). The temperature measurement at 200 mbsf was the only deployment with an interpretable decay curve and indicated a temperature of 3.59°C. This is in good agreement with measurements from Hole 1040C. All pressure measurements were unsuccessful because of tool movement when in formation. However, pressures measured at the mudline and bottom of the hole are in very good agreement with expected hydrostatic pressures expected at that depth, which clearly demonstrates that the pressure sensor is reliable.

Summary

In summary, the analyses of structural fabric and geochemical anomalies allowed us to identify a fault and geochemical boundary at ~218 mbsf. The region above has pore fluids typical of clay-rich sediments; below, the section is lithologically homogeneous but permeated by a fluid from a source at elevated temperature. At ~338.5 mbsf a fault marks the upper boundary of the décollement zone, which extends into the upper meters of the underthrust sequence at 364.2 mbsf. Maximum pore fluid chemical anomalies, indicative of active fluid flow, may preferentially follow zones characterized by brittle fabric. Analysis of cores from the two intervals allowed us to select the optimal depth interval for the long-term borehole fluid sampler experiment. However, because of unstable hole conditions, the attempts to install a CORK-II failed and Site 1254 had to be abandoned because of time constraints.

Site 1255

Site 1255 is located ~0.4 km arcward from the deformation front at a water depth of 4311.6 m and in close vicinity to the holes of Site 1043 drilled during Leg 170 (Kimura, Silver, Blum, et al., 1997). Hole 1255A is ~20 m east of Hole 1043A and ~30 m northwest of Hole 1043B (Figs. F3, F28, F29). In Hole 1043A the complete section was cored to 282 mbsf in the underthrust sequence (Unit U3), whereas Hole 1043B was logged using LWD to 482 mbsf, the top of the igneous basement. As both holes penetrated the décollement, their results were used to plan the drilling strategy and the installation of the CORK-II observatory.

F28. Location of Site 1255, p. 70.

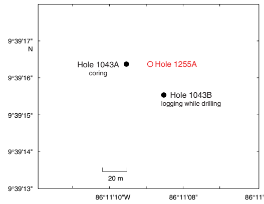

The objective of Site 1255 was to identify the décollement with "real-time" geochemical analyses and penetration rate and to install a long-term observatory for monitoring of fluid flow, pressure, and temperature in the décollement. Because of time constraints, only four cores were taken from 123 to 157 mbsf. We recovered 7.2 m (21%) from the 34-m cored section. Because of the limited recovery and whole-round sections taken for pore water analyses for locating the décollement, other studies on the cores were limited.

F29. Multichannel seismic profile BGR 99-44, p. 71.

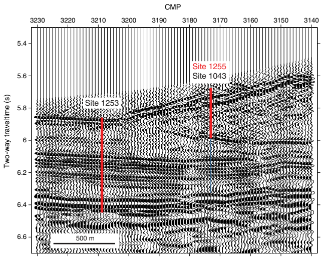

The seismic record (Fig. F29) in the vicinity of Hole 1255A (CMP 3174) shows no coherent reflections above the décollement. This reflects the general chaotic sedimentary pattern observed already in cores from Site 1254 and in Leg 170 results. The confused seafloor reflection pattern, masking a clear seafloor identification, is probably due to side echoes, generated by local bathymetric relief (Fig. F3). The first prominent reflector relevant for drilling is at 5.96 s TWT, which marks the boundary between margin sediments and the underthrust sequence, cored at 144 mbsf in Hole 1255A. The current seismic data do not show any evidence for fault zones above the décollement.

After setting the reentry cone in Hole 1255A, we drilled to a depth of 123 mbsf with a 14¾-in bit. We then installed 10¾-in casing to a depth of 117 mbsf and cemented it in. Coring started at 123 mbsf, after drilling out the cement shoe, and stopped at 157 mbsf when a sudden increase in penetration rate during cutting of the fourth core indicated that the underthrust sediments were reached. The installation of the CORK-II was successful and completed with the deployment of the remotely operated vehicle (ROV) platform. A postcruise *Alvin* dive showed the installation to be fully operational, and pressure data showed a return to hydrostatic conditions within the borehole.

Lithostratigraphy

The section recovered from Hole 1255A can be separated into lithostratigraphic Unit T1 (equivalent to Subunit P1B at Site 1254) and Subunit U1A just beneath the level of the décollement at 144.08 mbsf. The division marks a sharp junction between a series of structureless greenish gray claystones with silts and few or no diatoms above an underlying series of diatom-rich claystones with interbedded silts, sands, and occasional fine-grained conglomerates. The clastic sediments in the underthrust section (Subunit U1A), interpreted as near-trench turbidites during Leg 170, differ from the purely hemipelagic diatom ooze recovered at Site 1043 (Kimura, Silver, Blum, et al., 1997). The fact that these turbidites were not recovered at Site 1043 may indicate that this section is very thin and simply not recovered or not present at all because of lateral facies changes over short distances. Blocks of reworked carbonate in Unit T1 indicate that these sediments are mostly debris flow deposits, in part derived originally from shallow nearshore environments. The presence of a pelagic nannofossil chalk interval and the larger proportion of diatoms at Site 1255 suggests that this site experienced a larger amount of pelagic sedimentation than did Site 1254. The underthrust section represents a trench depositional setting, with turbidite silts and sands interbedded with hemipelagic mudstones. Unlike other sites cored during Leg 205, sediments at Site 1255 contain no primary ash layers in the short section recovered; however, fresh and altered volcanic glass shards do compose a significant proportion (10%–15%) of the prism sediments.

Structural Geology

At Site 1255, structural deformation, with brecciation and polished clast surfaces as an indication of incipient scaly fabric, increases within the recovered section from 132.7 mbsf to the base of the décollement at 144.08 mbsf. The top of the décollement zone could not be defined as a result of limited coring and recovery. The base of the décollement is sharp and well defined and coincides with the division between Unit T1 and Subunit U1A. Only one measurement of bedding dip (44°) was possible in the décollement zone. The hemipelagic layers in the underthrust section below 144.08 mbsf show some medium-scale brecciation (1- to 3-cm fragments) with unpolished surfaces, whereas the sandy layers are undeformed.

Organic Geochemistry

Volatile hydrocarbon gases were sampled using the vacutainer and headspace technique. As no gas voids were apparent at Site 1255, in contrast to Site 1254, vacutainer samples show large air contamination. Headspace CH_4 concentrations drop rapidly from >3000 ppmv in Core 205-1255A-2R to 5 ppmv below the décollement (145 mbsf). Propane, as an indicator for deeply sourced fluids, is low in the prism section (~1 ppmv) and absent below the décollement.

Inorganic Geochemistry

Only three whole rounds (one per core) could be taken for geochemical analyses of pore waters because of low recovery, and all conclusions are therefore somewhat speculative. As observed at Site 1254, the chemical composition of the pore fluids at Site 1255 also is distinctly different in the wedge and underthrust section, with a less sharp transition at the base of the décollement zone at ~144 mbsf. Fluid flow is indicated by salinity, Na and Ca concentration minima, and a Li concentration maximum within the décollement sample at 134.2 mbsf. Similar concentration variations were observed at Site 1043 along with a magnesium concentration maximum within the same interval. Across the décollement, changes in Ca and Mg concentrations are in the opposite direction to those seen at Site 1254. In general, the pore fluids within the upper fault zone and in the décollement at Sites 1254 and 1040 are characterized by having a significantly stronger signature of a deeply sourced fluid than the pore fluids from Sites 1255 and 1043 (see **"Inorganic Geochemistry,"** p. 27, in the "Site 1254" chapter). At Sites 1255 and 1043, the pore fluid chemistry in the wedge and the uppermost underthrust sediments appears to reflect some mixing between the lower wedge and uppermost hemipelagic pore fluids, thereby partially obscuring the deeply sourced fluid signature observed at Site 1254. This pore water mixing could be achieved by advection of fluid from the underthrust section across the décollement and into the lower wedge.

Microbiology

Two samples for microbiological investigations were taken and either frozen or fixed for postcruise ATP quantification, DNA assessment, or cell counts. Samples of drilling water were frozen as well to evaluate contamination of cores. The chemical tracer for quantifying microbiological contamination was not deployed during coring in Hole 1255A because of concern that the trace element chemistry of the PFT may affect postcruise pore fluid geochemical analyses. Particulate tracer tests yielded fluorescent microsphere counts suggesting very low to no particulate contamination in the interior of the microbiology whole rounds.

Paleomagnetism

Paleomagnetic declination and inclination, measured on discrete samples and archive halves, disagree only in the upper part (132.76–134.84 mbsf) of the cored interval, making any magnetostratigraphic interpretation questionable within this interval. Across the décollement, a clear polarity change can be seen in both archive halves and discrete samples. However, the polarity changes cannot be assigned to a particular chron and are not usable for dating purposes. Magnetic intensities and susceptibilities are generally low in the upper part of the section but increase substantially in the sandy layers of the underthrust sequence.

Physical Properties

Sample porosities and LWD porosities from Leg 170 show a clear increase at the base of the décollement from values of ~55% in the prism section to values of ~70% in the underthrust. Sample porosities from Hole 1255A clearly confirm the values in the prism, but the few data points below the décollement are not representative of the porosity of the underthrust sequence but, rather, show the influence of sampling clayey or sandy material. Only the magnetic susceptibility shows a marked increase below the décollement, which reflects a presumably higher magnetite content in the turbidites of the underthrust.

CORK-II Installation

A CORK-II observatory was successfully installed as shown in Figure **F30.** The center of the packer is at 129 mbsf and the center of the screen at 140 mbsf, in the middle of the geochemical anomaly as determined from Site 1255 data and Site 1043 results. The second pressure port inside a small screen was installed just above the upper packer. This CORK-II installation was also visited by *Alvin* shortly after Leg 205 and was found to be fully operational (see next section).

F30. Hole 1253A borehole installation, p. 72.

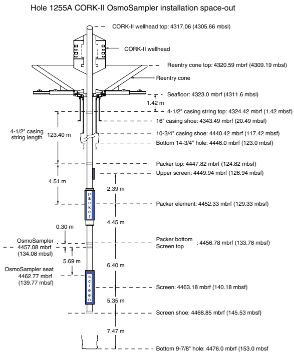

POSTCRUISE *ALVIN* SUBMERSIBLE VISIT TO SITE 1253 AND 1255 CORK-IIS

Because of the likelihood that the spool valves had not shifted and the packer had not inflated at the time of the CORK-II installation at Site 1253, a visit to the site was planned with the manned submersible *Alvin* in November 2002, roughly 1 month after the installation of the CORK-IIs. Data recovery operations at wireline-installed CORKs in Holes 504B and 896A, located on the southern flank of the Costa Rica Rift, had been fortuitously scheduled for this time. Proximity of the *Atlantis/Alvin* port call to the margin sites, efficiency of operations at the rift flank sites, and assistance from the National Science Foundation made the visit to the margin sites possible. Participants in that program included K. Becker (chief scientist), E. Davis, T. Pettigrew, and R. Meldrum. The site visits are documented in two edited videos that show the seafloor installations and data downloading (Figs. **F31, F32**).

F31. CORK head at Site 1253, p. 73.

Two parallel solutions were prepared for resolving the spool-valve problem. The first would make use of a pump mated to the hydraulic connection at the top of the CORK-II assembly that accesses the packer-filling line (the very line that was believed not to have been pressurized when the packer-inflation go-devil failed to reach its landing point during deployment). This pump was designed and built by B. Carson and L. Holloway for formation testing in the CORKed Hole 949C in the Barbados accretionary prism. If this operation were to fail, a second approach would employ a stand-alone pressure sensor and data logger constructed by E. Davis and R. Macdonald that would be coupled to the redundant fluid sampling line from the lower CORK-II formation screen, which was plumbed to the seafloor through a valved port. This sensor/logger unit was equipped with an underwater-mateable electrical connector identical to that on the CORK-II unit itself to facilitate data downloading at the time of future site visits.

F32. CORK head at Site 1255, p. 74.

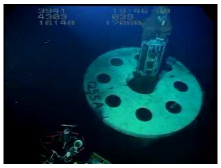

As it turned out, visual inspection to the CORK-II head showed that both spool valves had indeed shifted (although the left-hand piston was ~¼ in above the level of the right) despite the go-devil never properly landing. The pump was coupled and run for 16.5 min as an ultimate precaution (this served to shift the left-hand spool valve fully down to the same level as the right). However, following an inspection of the downloaded data, it became clear that the installation was successful from the beginning. The success was evident from the data showing tidal pressure signals in basement and small, but well-resolved, average pressure differentials (several kilopascals) between the two basement levels separated by the packer.

Time remaining after operations at Site 1253 was just enough to allow a visit to Site 1255 before the end of the dive. The site was somewhat difficult to find using the sonar scanner on the *Alvin,* as the site is located at the bottom of a local topographic slope or in a local depression. Here two more mysteries awaited. First, despite the T-handles having been secured by rubber bands at the time of deployment, the top-left sampling valve was found to be rotated ~10° from horizontal. This brought bad memories of Leg 196; the cause of this behavior remains unknown. Fortunately in this instance, the rotation was insufficient to cause the valve to leak. The second mystery is that the formation pressure registered by the sensor connected to the deeper level below the packer indicated leakage somewhere in the CORK-II plumbing until ~36 hr before the submersible arrived. Pressures at the sensor remained close to hydrostatic, and the tidal signal remained unattenuated relative to seafloor pressure until a time near the end of this first recording period, when the sensor pressure rose to a level somewhat higher than that observed in the upper interval (~180 kPa) and displayed an attenuated tidal variation. It is with considerable confidence that we now look forward to the first real phase of data recording and first OsmoSampler recovery at both of these sites.

REFERENCES

Abratis, M.W., and Woerner, G., 2001. Ridge collision, slab-window formation, and the flux of Pacific asthenosphere into the Caribbean realm. *Geology,* 29:127–130.

Barckhausen, U., Ranero, C.R., von Huene, R., Cande, S.C., and Roeser, H.A., 2001. Revised tectonic boundaries in the Cocos plate off Costa Rica: implications for the segmentation of the convergent margin and for plate tectonic models. *J. Geophys. Res.,* 106:19207–19220.

Barckhausen, U., Roeser, H.A., and von Huene, R., 1998. Magnetic signature of upper plate structures and subducting seamounts at the convergent margin off Costa Rica. *J. Geophys. Res.,* 103:7079–7093.

Becker, K., Fisher, A.T., and Davis, E.E., 1997. The CORK experiment in Hole 949C: long-term observations of pressure and temperature in the Barbados accretionary prism. *In* Shipley, T.H., Ogawa, Y., Blum, P., and Bahr, J.M. (Eds.), *Proc. ODP, Sci. Results,* 156: College Station, TX (Ocean Drilling Program), 247–252.

Becker, K., the Leg 174B Scientific Party, and Davis, E.E., 1998. Leg 174B revisits Hole 395A: logging and long-term monitoring of off-axis hydrothermal processes in young oceanic crust. *JOIDES J.,* 24:1–3, 13.

Carr, M.J., Feigenson, M.D., and Bennett, E.A., 1990. Incompatible element and isotopic evidence for tectonic control of source mixing and melt extraction along the Central American arc. *Contrib. Mineral. Petrol.,* 105:369–380.

Chan, L.-H., and Kastner, M., 2000. Lithium isotopic compositions of pore fluids and sediments in the Costa Rica subduction zone: implications for fluid processes and sediment contribution to the arc volcanoes. *Earth Planet. Sci. Lett.,* 183:275–290.

Christeson, G.L., McIntosh, K.D., and Shipley, T.H., 2000. Seismic attenuation in the Costa Rica margin wedge: amplitude modeling of ocean bottom hydrophone data. *Earth Planet. Sci. Lett.,* 179:391–405.

Christeson, G.L., McIntosh, K.D., Shipley, T.H., Flueh, E., and Goedde, H., 1999. Structure of the Costa Rica convergent margin, offshore Nicoya Peninsula. *J. Geophys. Res.,* 104:25443–25468.

Davis, E.E., and Becker, K., 1994. Formation temperatures and pressures in a sedimented rift hydrothermal system: ten months of CORK observations, Holes 857D and 858G. *In* Mottl, M.J., Davis, E.E., Fisher, A.T., and Slack, J.F. (Eds.), *Proc. ODP, Sci. Results,* 139: College Station, TX (Ocean Drilling Program), 649–666.

Davis, E.E., Wang, K., Becker, K., and Thomson, R.E., 2000. Formation-scale hydraulic and mechanical properties of oceanic crust inferred from pore pressure response to periodic seafloor loading. *J. Geophys. Res.,* 105:13423–13435.

DeMets, C., Gordon, R.G., Argus, D.F., and Stein, S., 1990. Current plate motions. *Geophys. J. Internat.,* 101:425–478.

Fisher, A.T., 1998. Permeability within basaltic oceanic crust. *Rev. Geophys.,* 36:143–182.

Guendel, F., 1986. Seismotectonics of Costa Rica: an analytical view of the southern terminus of the Middle America Trench [Ph.D. thesis]. Univ. of California, Santa Cruz.

Hauff, F., Hoernle, K., Schminke, H.-U., and Werner, R., 1997. A mid-Cretaceous origin for the Galapagos hotspot: volcanological, petrological, and geochemical evidence from Costa Rican oceanic crustal segments. *Geol. Rundsch.,* 86:141–155.

Hey, R.N., 1977. Tectonic evolution of the Cocos-Nazca spreading center. *Geol. Soc. Am. Bull.,* 88:1404–1420.

JOIDES Planning Committee, 1996. *Understanding our Dynamic Earth through Ocean Drilling: Ocean Drilling Program Long Range Plan into the 21st Century:* Washington, D.C. (JOI).

Kastner, M., Morris, J., Chan, L.H., Saether, O., and Lückge, A., 2000. Three distinct fluid systems at the Costa Rica subduction zone: chemistry, hydrology, and fluxes. *Goldschmidt 2000, J. Conf. Abstr.,* 5:572. (Abstract)

Kelly, R.K., and Driscoll, N.W., 1998. Structural controls on ^{10}Be occurrences in arc lavas. *Eos,* 79:45.

Kimura, G., Silver, E.A., Blum, P., et al., 1997. *Proc. ODP, Init. Repts.,* 170: College Station, TX (Ocean Drilling Program).

Kopf, A., Deyhle, A., and Zuleger, E., 2000. Evidence for deep fluid circulation and gas hydrate dissociation using boron isotopes of pore fluids in forearc sediments from Costa Rica (ODP Leg 170). *Mar. Geol.,* 167:1–28.

Langseth, M.G., and Silver, E.A., 1996. The Nicoya convergent margin: a region of exceptionally low heat flow. *Geophys. Res. Lett.,* 23:891–894.

Lonsdale, P., and Klitgord, K.D., 1978. Structure and tectonic history of the eastern Panama Basin. *Geol. Soc. Am. Bull.,* 89:981–999.

Lückge, A., Kastner, M., Littke, R., and Cramer, B., 2002. Hydrocarbon gas in the Costa Rica subduction zone: primary composition and post-genetic alteration. *Org. Geochem.,* 33:933–943.

McIntosh, K.D., and Sen, M.K., 2000. Geophysical evidence for dewatering and deformation processes in the ODP Leg 170 area offshore Costa Rica. *Earth Planet. Sci. Lett.,* 178:125–138.

McIntosh, K.D., Silver, E.A., and Shipley, T., 1993. Evidence and mechanisms for forearc extension at the accretionary Costa Rica convergent margin. *Tectonics,* 12:1380–1392.

Meschede, M., Zweigel, P., Frisch, W., and Völker, D., 1999a. Mélange formation by subduction erosion: the case of the Osa mélange, southern Costa Rica. *Terra Nova,* 11:141–148.

Meschede, M., Zweigel, P., and Kiefer, E., 1999b. Subsidence and extension at a convergent plate margin: evidence for subduction erosion off Costa Rica. *Terra Nova,* 11:112–117.

Moore, J.C., and Saffer, D.M., 2001. Updip limit of the seismogenic zone beneath the accretionary prism of southwest Japan: an effect of diagenetic to low-grade metamorphic processes and increasing effective stress. *Geology,* 29:183–186.

Moritz, E., Bornholdt, S., Westphal, H., and Meschede, M., 2000. Neural network interpretation of LWD data (ODP Leg 170) confirms complete sediment subduction at the Costa Rica convergent margin. *Earth Planet. Sci. Lett.,* 174:301–312.

Morris, J.D., Valentine, R., and Harrison, T., 2002. ^{10}Be imaging of sediment accretion, subduction along the northeast Japan and Costa Rica convergent margins. *Geology,* 30:59–62.

Newman, A.V., Schwartz, S.Y., Gonzalez, V., DeShon, H.R., Protti, J.M., Dorman, L.M., 2002. Along-strike variability in the seismogenic zone below Nicoya Peninsula, Costa Rica. *Geophys. Res. Lett.,* 29:10.10292002GL015409.

Patino, L.C., Carr, M.J., and Feigenson, M.D., 2000. Local and regional variations in Central American arc lavas controlled by variations in subducted sediment input. *Contrib. Mineral. Petrol.,* 138:265–283.

Pecher, I.A., Kukowski, N., Ranero, C.R., and von Huene, R., 2001. Gas hydrates along the Peru and Middle America Trench system. *In* Paull, C.K., and Dillon, W.P. (Eds.), *Natural Gas Hydrates: Occurrence, Distribution, and Detection.* Am. Geophys. Union, Geophys. Monogr., 124:257–271.

Pfender, M., and Villinger, H., 2002. Miniaturized data loggers for deep sea sediment temperature gradient measurements. *Mar. Geol.,* 186:557–570.

Protti, M., Guendel, F., and McNally, K., 1994. The geometry of the Wadati-Benioff zone under southern Central America and its tectonic significance: results from a high-resolution local seismographic network. *Phys. Earth Planet. Internat.,* 84:271–287.

Ranero, C.R., and von Huene, R., 2000. Subduction erosion along the Middle America convergent margin. *Nature,* 404:748–752.

Ranero, C.R., von Huene, R., Flueh, E., Duarte, M., Baca, D., and McIntosh, K.D., 2000a. A cross section of the convergent Pacific margin of Nicaragua. *Tectonics,* 19:335–357.

Ranero, C.R., von Huene, R., Weinrebe, W., McIntosh, K.D., and Reichert, C., 2000b. Mass transfer and fluid flow paths related to subduction erosion at the Middle America convergent margin. *Eos, Am. Geophys. Union,* 81:F81.

Reagan, M., Morris, J., Herrstrom, E., and Murrell, M., 1994. Uranium series and beryllium isotopic evidence for an extended history of subduction modification of the mantle below Nicaragua. *Geochim. Cosmochim. Acta,* 58:4199–4212.

Ruppel, C.K., and Kinoshita, M., 2000. Fluid, methane, and energy flux in an active margin gas hydrate province, offshore Costa Rica. *Earth Planet. Sci., Lett.,* 179:153–165.

Saffer, D.M., in press. Pore pressure development and progressive dewatering in underthrust sediments at the Costa Rica subduction margin: comparison with Northern Barbados and Nankai. *J. Geophys. Res.*

Saffer, D.M., Silver, E.A., Fisher, A.T., Tobin, H., and Moran, K., 2000. Inferred pore pressures at the Costa Rica subduction zone: implications for dewatering processes. *Earth Planet. Sci. Lett.,* 177:193–207.

Scholz, C.H., 1998. Earthquakes and friction laws. *Nature,* 391:37–42.

Screaton, E.J., Saffer, D.M., Henry, P., Hunze, S., and the Leg 190 Shipboard Scientific Party, in press. Porosity loss within underthrust sediments of the Nankai accretionary complex: implications for overpressures. *Geology.*

Shipley, T.H., McIntosh, K.D., Silver, E.A., and Stoffa, P.L., 1992. Three-dimensional seismic imaging of the Costa Rica accretionary prism: structural diversity in a small volume of the lower slope. *J. Geophys. Res.,* 97:4439–4459.

Shipley, T.H., and Moore, G.F., 1986. Sediment accretion, subduction, and dewatering at the base of the trench slope off Costa Rica: a seismic reflection view of the décollement. *J. Geophys. Res.,* 91:2019–2028.

Silver, E.A., Kastner, M., Fisher, A.T., Morris, J.D., McIntosh, K.D., and Saffer, D.M., 2000. Fluid flow paths in the Middle America Trench and Costa Rica margin. *Geology,* 28:679–682.

Silver, E.A., Kimura, G., and Shipley, T.H. (Eds.), 2001. *Proc. ODP, Sci. Results,* 170 [CD-ROM]. Available from: Ocean Drilling Program, Texas A&M University, College Station TX 77845-9547, USA.

Stein, C.A., and Stein, S., 1992. A model for the global variation in oceanic depth and heat flow with lithospheric age. *Nature,* 359:123–129.

Tera, F., Brown, L., Morris, J., Sacks, I.S., Klein, J., and Middleton, R., 1986. Sediment incorporation in island-arc magmas: inferences from ^{10}Be. *Geochim. Cosmochim. Acta,* 50:535–550.

Tobin, H., Vannucchi, P., and Meschede, M., 2001. Structure, inferred mechanics, and implications for fluid transport in the décollement zone, Costa Rica convergent margin. *Geology,* 29:907–910.

Valentine, R., Morris, J.D., and Duncan, D., 1997. Sediment subduction, accretion, underplating and arc volcanism along the margin of Costa Rica: constraints from Ba, Zn, Ni, and ^{10}Be concentrations. *Eos,* 78:F673.

Vannucchi, P., Ranero, C.R., Galeotti, S., Straub, S.M., Scholl, D.W., and McDougall-Ried, K., in press. Rates of subduction erosion along the Costa Rica Pacific margin: implications for non-steady rates of Austral recycling at a subduction zone. *J. Geophys. Res.*

Vannucchi, P., Scholl, D.W., Meschede, M., and McDougall-Reid, K., 2001. Tectonic erosion and consequent collapse of the Pacific margin of Costa Rica: combined implications from ODP Leg 170, seismic offshore data, and regional geology of the Nicoya Peninsula. *Tectonics,* 20:649–668.

Vannucchi, P., and Tobin, H., 2000. Deformation structures and implications for fluid flow at the Costa Rica convergent margin, Ocean Drilling Program Sites 1040 and 1043, Leg 170. *J. Struct. Geol.,* 22:1087–1103.

von Huene, R., Ranero, C.R., Weinrebe, W., and Hinz, K., 2000. Quaternary convergent margin tectonics of Costa Rica, segmentation of the Cocos plate, and Central American volcanism. *Tectonics,* 19:314–334.

von Huene, R., and Scholl, D.W., 1991. Observations at convergent margins concerning sediment subduction, subduction erosion, and the growth of the continental crust. *Rev. Geophys.,* 29:279–316.

Watkins, N.D., Sparks, R.S.J., Sigurdsson, H., Huang, T.C., Federman, A., Carey, S., and Ninkovich, D., 1978. Volume and extent of the Minoan tephra layer from Santorini volcano: new evidence from deep-sea sediment cores. *Nature,* 271:122–126.

Walther, C.H., Flueh, E., Ranero, C.R., von Huene, R., and Strauch, W., 2000. An unusual crustal structure across the Pacific margin of Nicaragua. *Geophys. J. Int.,* 14:759–777.

Wilson, D.S., 1996. Fastest known spreading on the Miocene Cocos-Pacific plate boundary. *Geophys. Res. Lett.,* 23:3003–3006.

Wilson, D.S., Teagle, D.A.H., Acton, G.D., et al., in press. *Proc. ODP, Init. Repts.,* 206 [CD-ROM]. Available from: Ocean Drilling Program, Texas A&M University, College Station TX 77845-9547, USA.

Zhao, Z., Moore, G.F., and Shipley, T.H., 1998. Deformation and dewatering of the subducting plate beneath the lower slope of the northern Barbados accretionary prism. *J. Geophys. Res.,* 103:30432–30449.

Figure F1. Bathymetric map of the eastern central Pacific showing the location of the Leg 205 drilling area in the Middle America Trench offshore Costa Rica. The white box shows the location of the map in Figure F2, p. 43. The white circle denotes the location of the Leg 206 site. The map is modified after Vannucchi et al. (in press) based on a data compilation of C. Ranero.

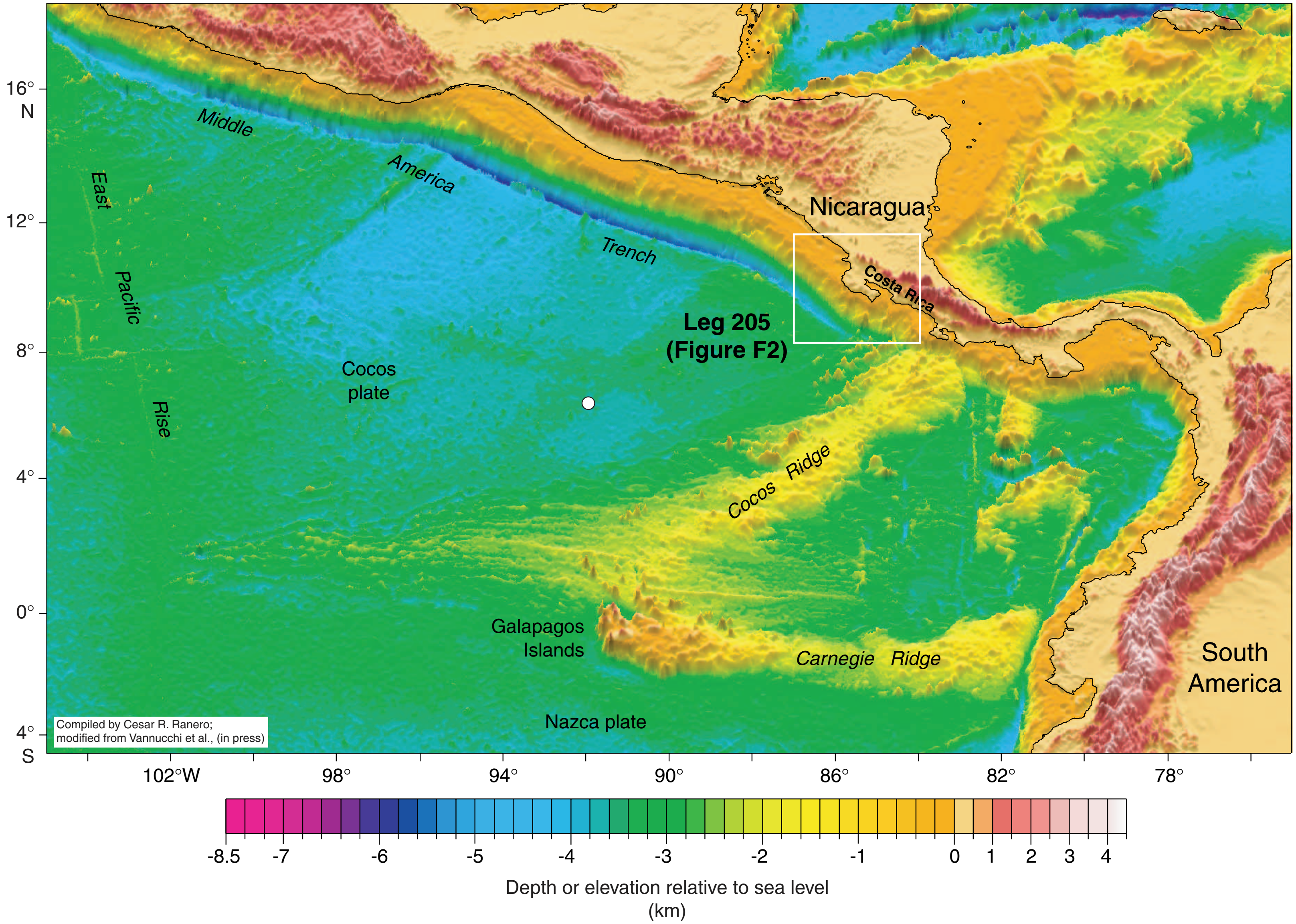

Compiled by Cesar R. Ranero;
modified from Vannucchi et al., (in press)

Figure F2. Bathymetric map of the Middle America Trench offshore the Nicoya Peninsula, Costa Rica. The white box shows the location of the Leg 205 drilling area shown in Figure F3, p. 44. Bathymetry is from Hydrosweep (Ranero and von Huene, 2000) and Simrad (E. Flueh, pers. comm., 2002) swath-mapping data combined with ETOPO5.

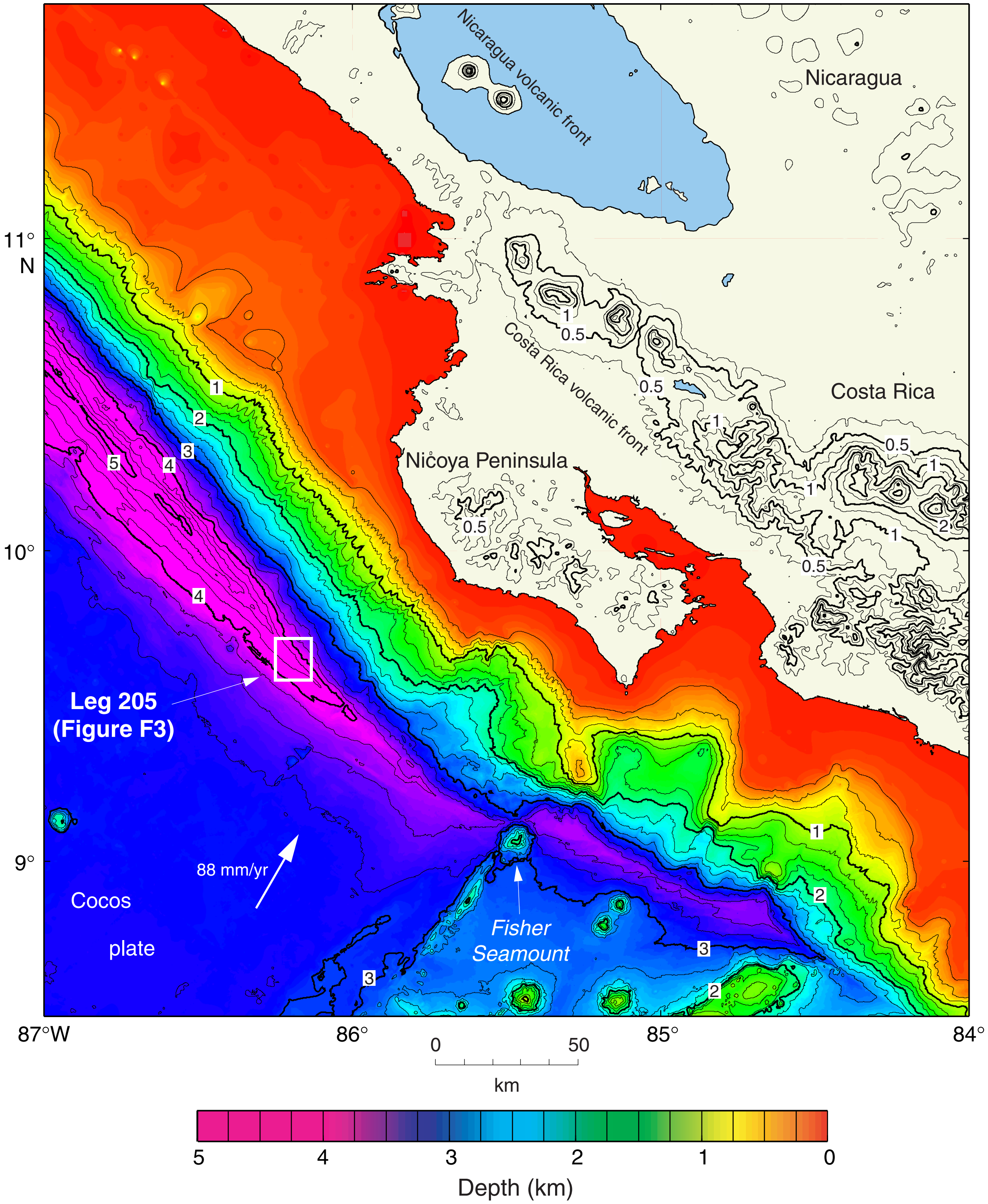

Figure F3. Bathymetric map of the Leg 205 drilling area showing Leg 205 (large yellow dots) and 170 (small white dots) drill sites. Seismic profiles are shown by the thick red (Fig. F24, p. 66) (BGR-99-44; C. Reichert and C. Ranero, pers. comm., 2001) and thin yellow (CR-20; Shipley et al., 1992) lines. Leg 170 drill sites were based on seismic profile CR-20 (thin yellow line). The segment of multichannel seismic profile BGR 99-44 (thick red line) across Sites 1253 and 1039 is also shown in Figure F22, p. 64. Numbers along the BGR 99-44 seismic line are shotpoints. The white arrow gives the convergence direction (N30°E) and rate (88 mm/yr) (DeMets et al., 1990). The location of the map is shown in Figure F2, p. 43; bathymetric contours are in meters. The bathymetric map is an integration of the compilation by Ranero and von Huene (2000) and Simrad data from E. Flueh (pers. comm., 2000).

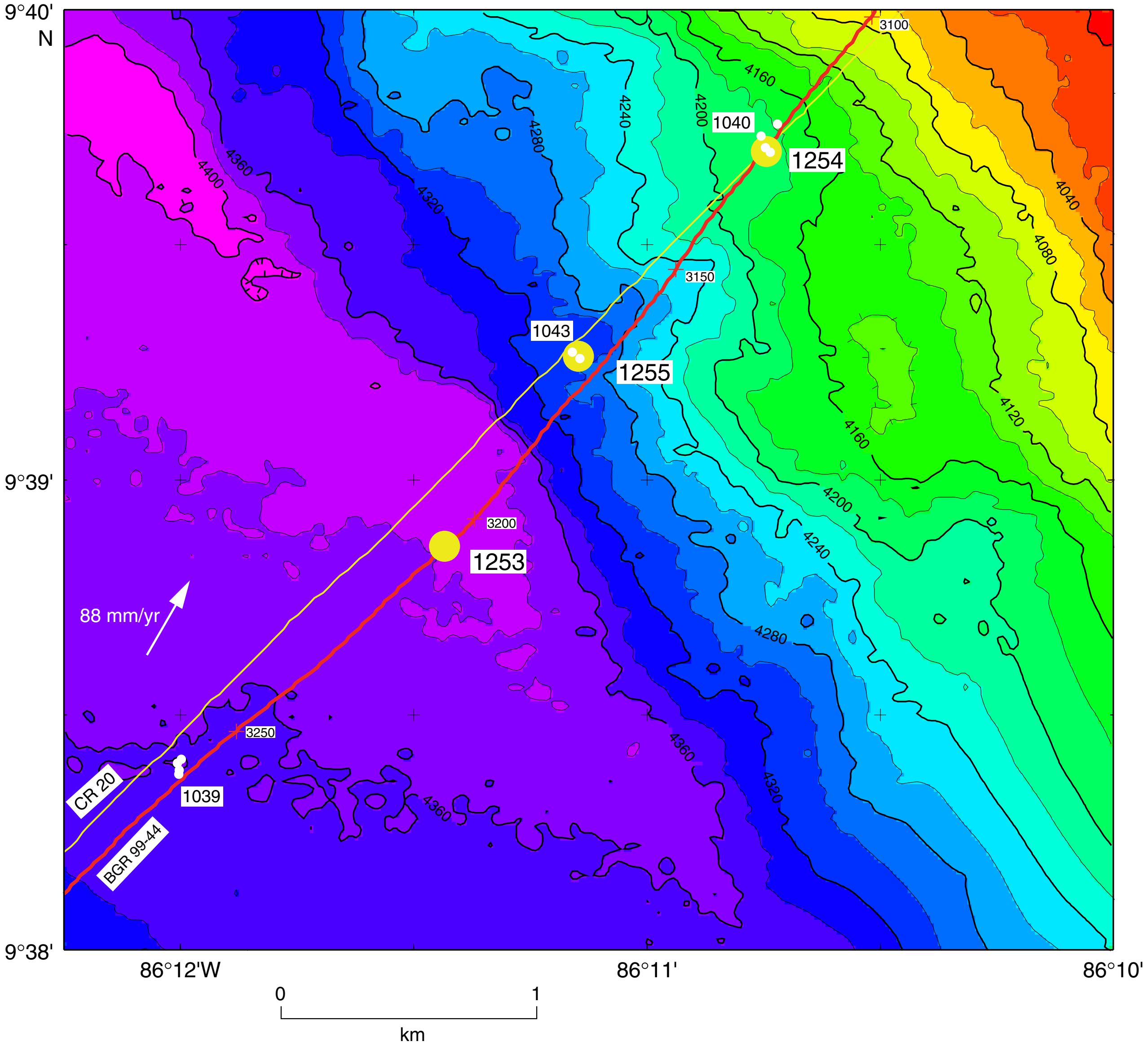

Figure F4. Leg 205 Costa Rica drilling area (red box) (Fig. F3, p. 44) and isochrons derived from seafloor magnetic anomalies (Barckhausen et al., 2001). Numbers indicate crustal age in millions of years. Tectonic boundaries, convergence direction and rate (arrow) (DeMets et al., 1990), and arc volcanoes (triangles) are shown. *FS* = Fisher Seamount, QSC = Quesada Sharp Contortion.

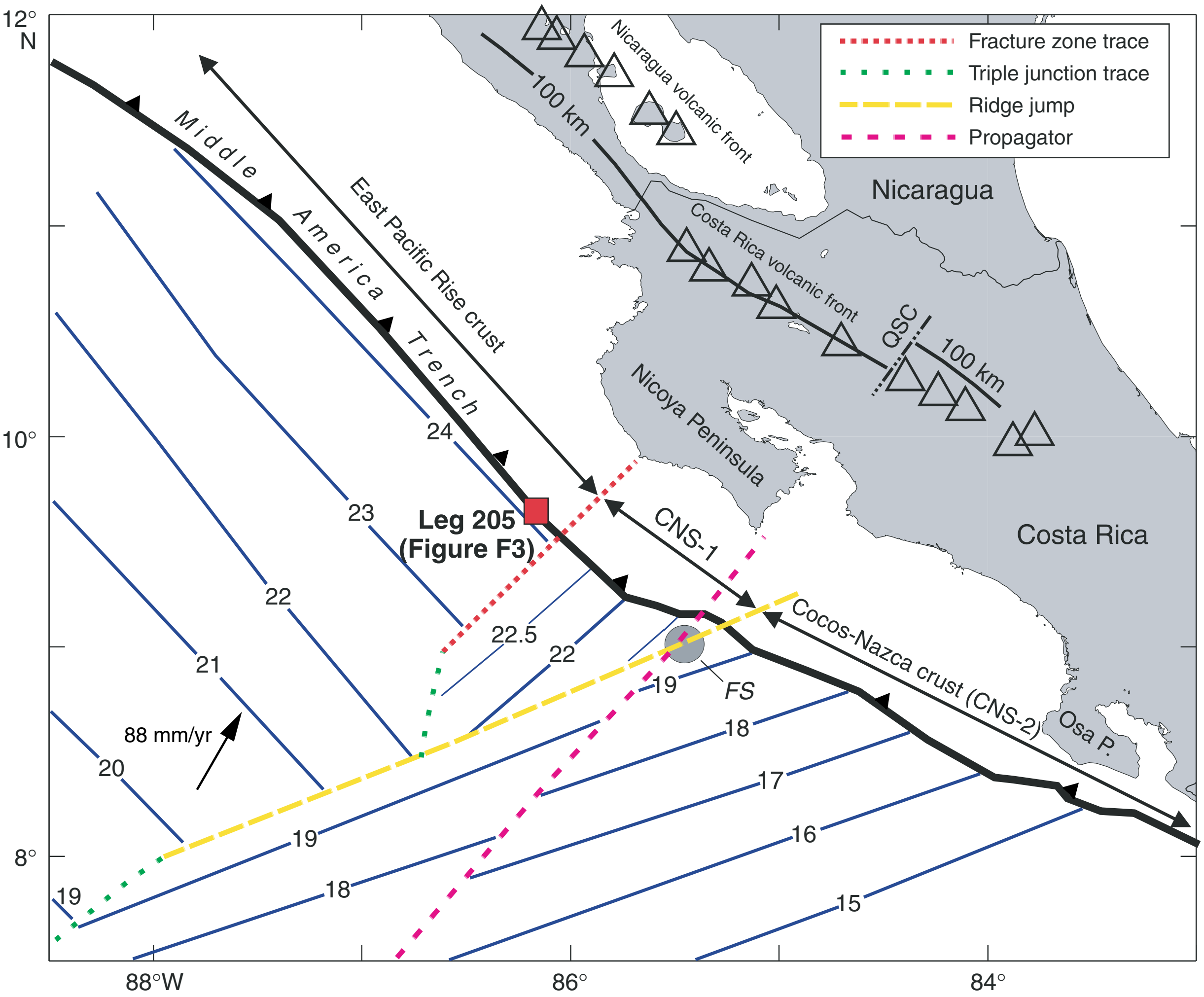

Figure F5. Summary of recovered lithology at drill sites on the incoming plate offshore Guatemala (Deep Sea Drilling Project Site 495) and Costa Rica (Site 1039) as well as on the Costa Rica margin (Sites 1040 and 1043). Note the similarity of incoming sediment sections at Sites 1039 and 495, as well as the repetition of the Site 1039 section below the décollement at Sites 1040 and 1043. Lithologic columns are modified from Kimura, Silver, Blum, et al. (1997).

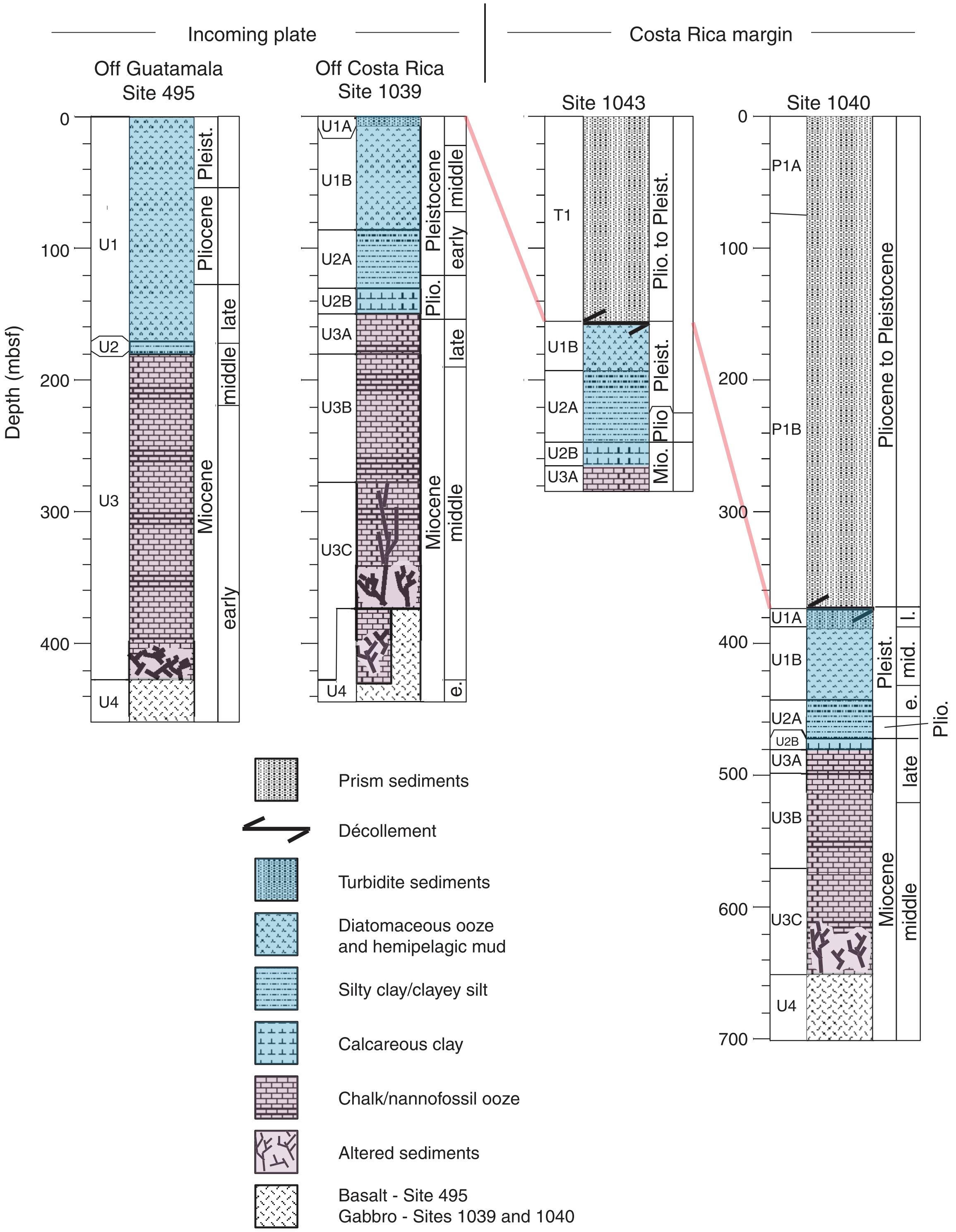

Figure F6. Migrated multichannel seismic profile BGR-99-44 (C. Ranero and C. Reichert, pers. comm., 2001) across the Middle America Trench. Thick red lines = Leg 205 Sites 1253, 1254, and 1255. Thin black lines = Site 1039, 1040, and 1043 (Leg 170) locations (Kimura, Silver, Blum, et al., 1997). CMP = common midpoint.

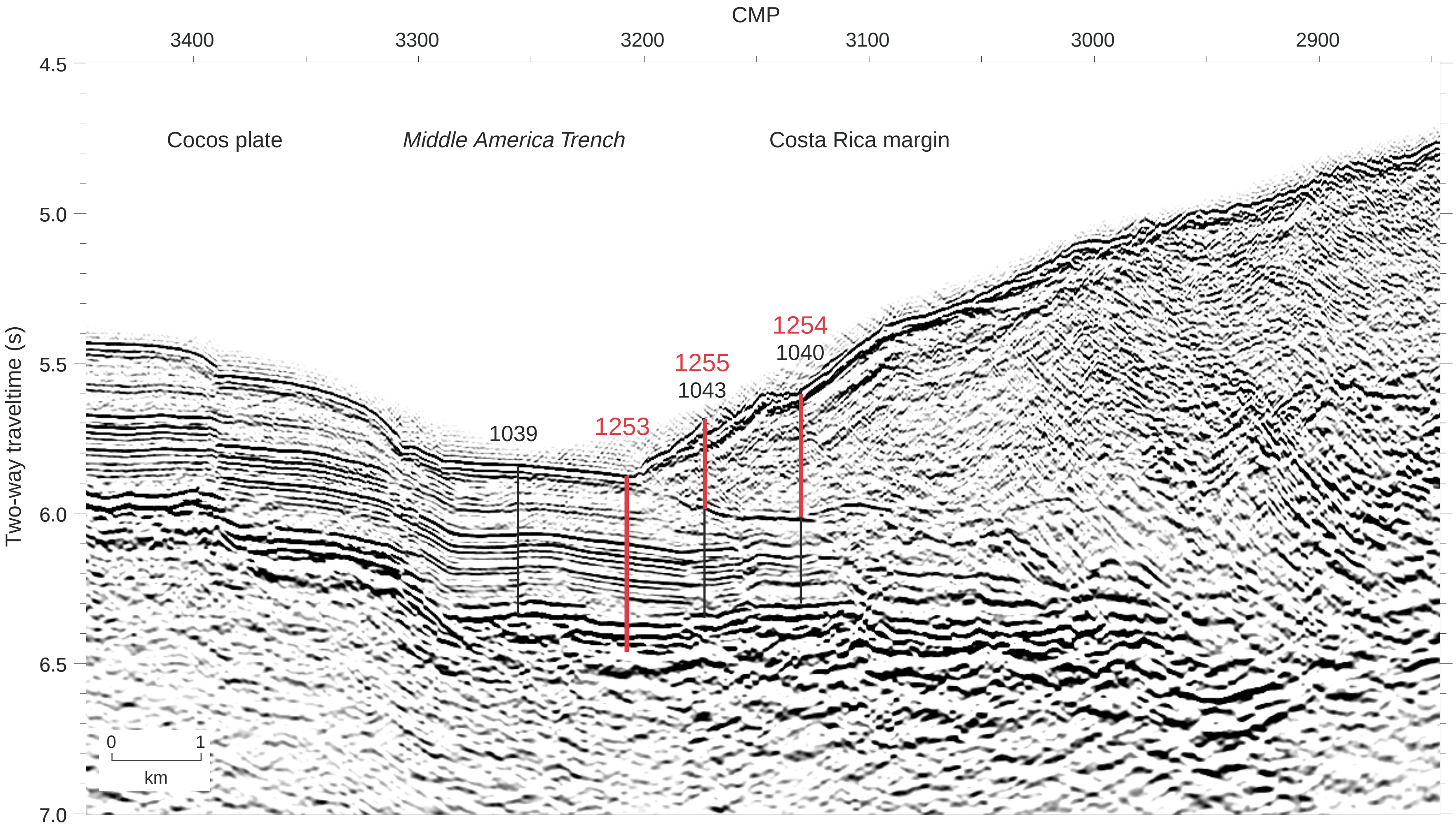

Figure F7. Plot of cosmogenic ^{10}Be vs. depth below seafloor at Site 1040. Produced by cosmic rays in the atmosphere and decaying with a 1.5-m.y. half-life, measurable ^{10}Be enrichments are seen in sediments younger than 7–10 Ma. The underthrust sediments beneath the décollement (blue and purple) have high values typical of the incoming sediment section. Throughout the prism sediments of the upper plate, ^{10}Be concentrations are very low, typical of sediments that are older than 3–5 Ma. Biostratigraphic (triangles) and magnetostratigraphic (x's) ages as well as sedimentation rates from Leg 170 cores (Kimura, Silver, Blum, et al., 1997) are shown on the right.

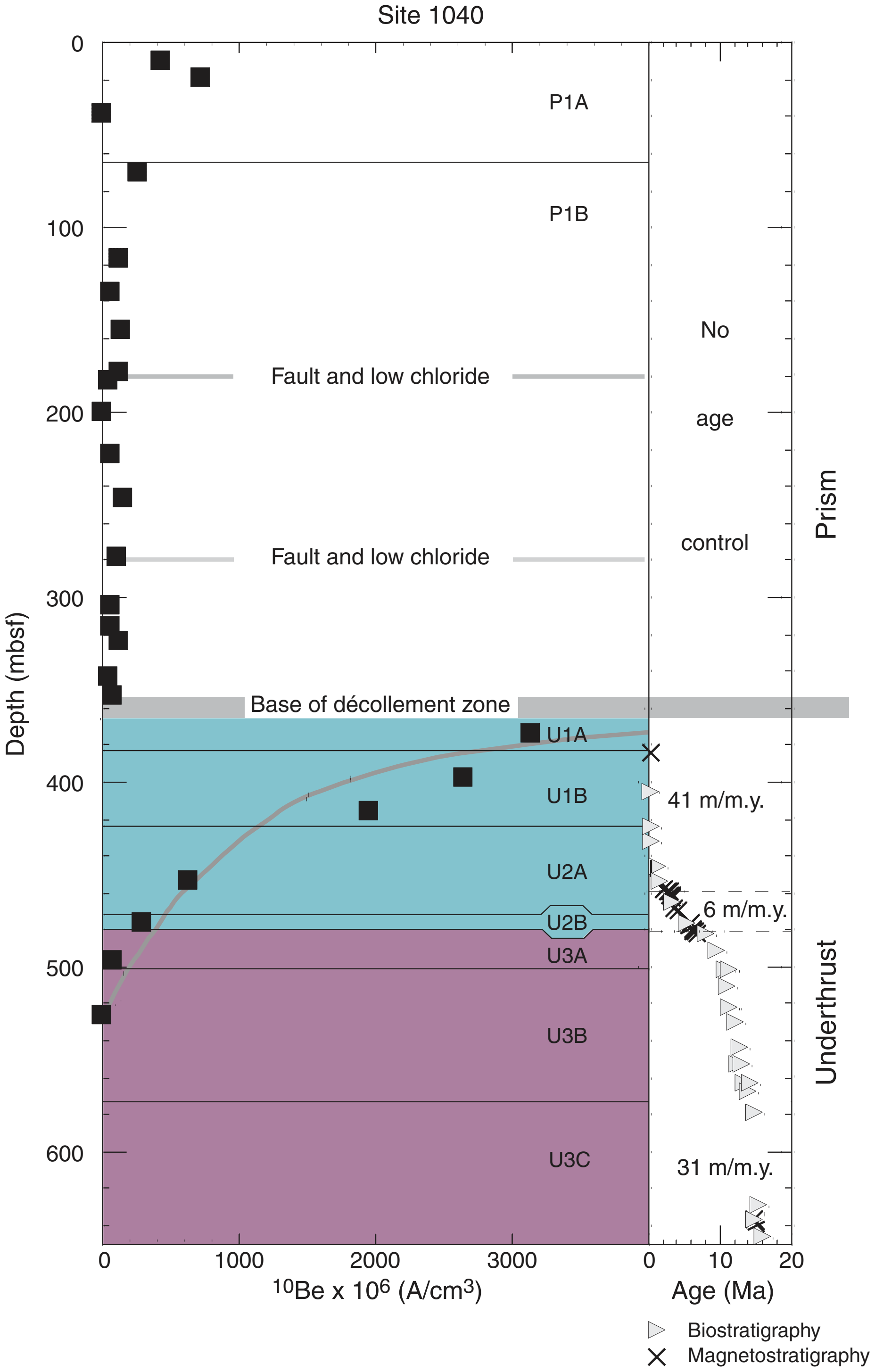

Figure F8. **A.** Heat flow measurements in the Leg 205 study area. The red box shows data projected onto a line (blue) across the Leg 205 and 170 drill sites, which are shown below. The *Meteor* and Langseth and Silver (1996) data are from shallow penetration probes, and the Leg 170 data are from deeper penetration boreholes at Sites 1039, 1040, and 1043. **B.** Heat flow projected onto a line across the Leg 205 and 170 drill sites. The x-axis shows the distance from the deformation front.

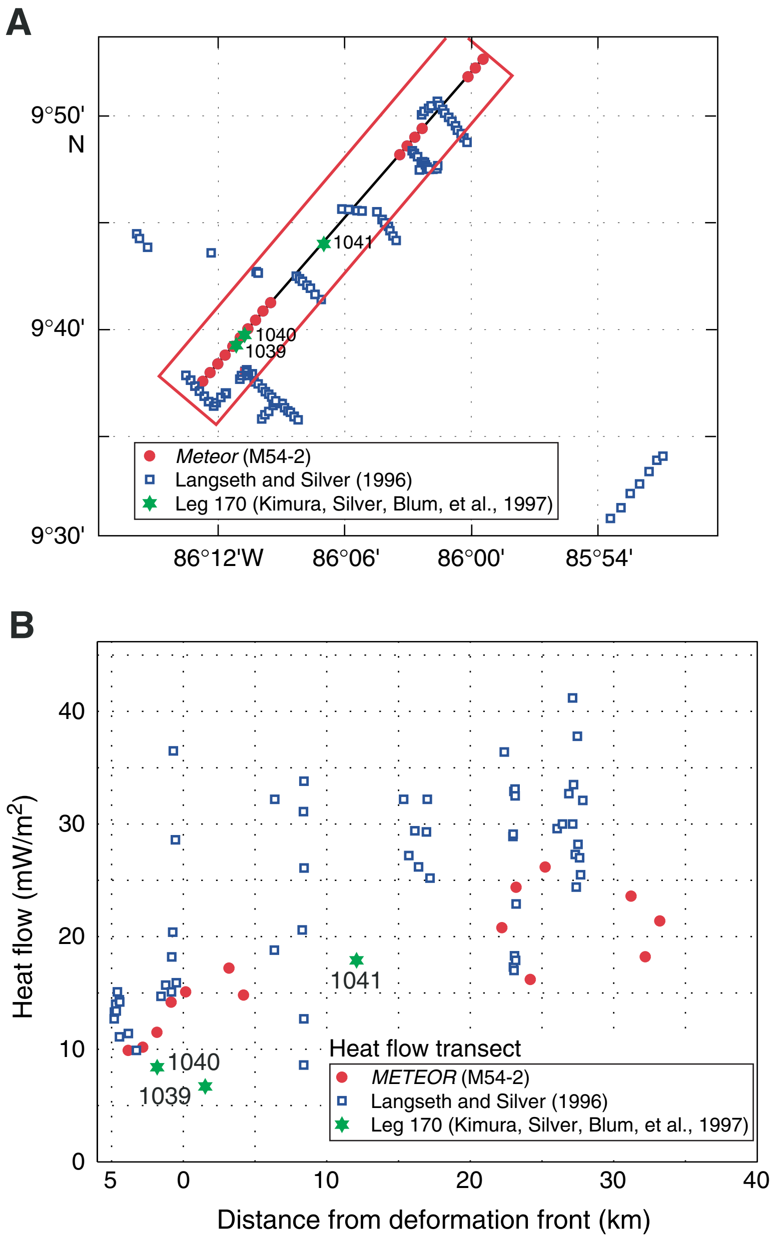

Figure F9. Strontium isotope ratios from pore water samples from Site 1039 are indicated by data points and the solid line, with the dashed line showing the strontium seawater curve appropriate to the sediment age. Note the basal pore water trend toward modern seawater composition, with values greater than Miocene seawater, indicating a strong seawater component in basement fluids. Similar variations are seen in calcium and strontium concentration data.

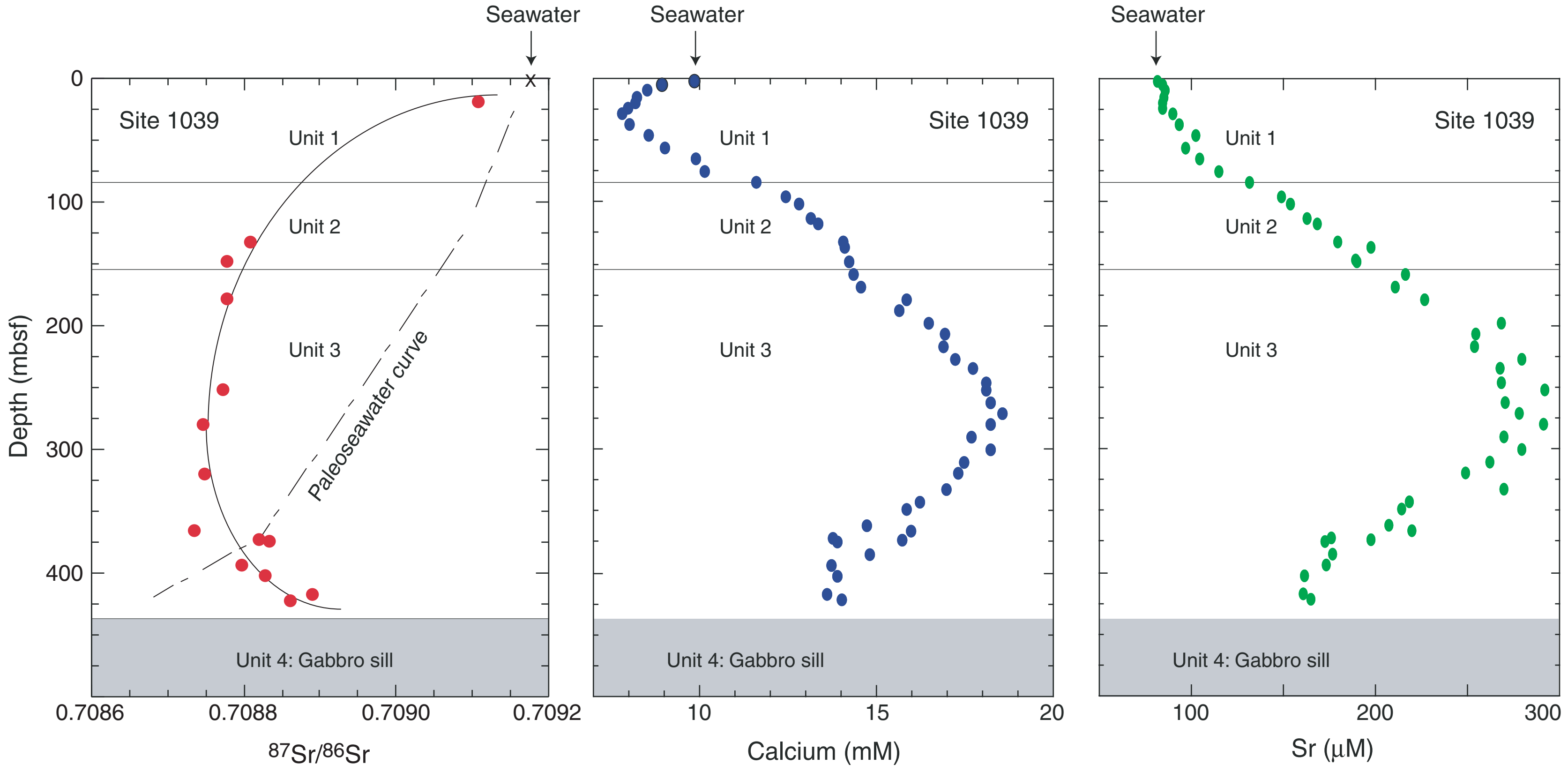

Figure F10. Structures and geochemical anomalies at Hole 1040A.

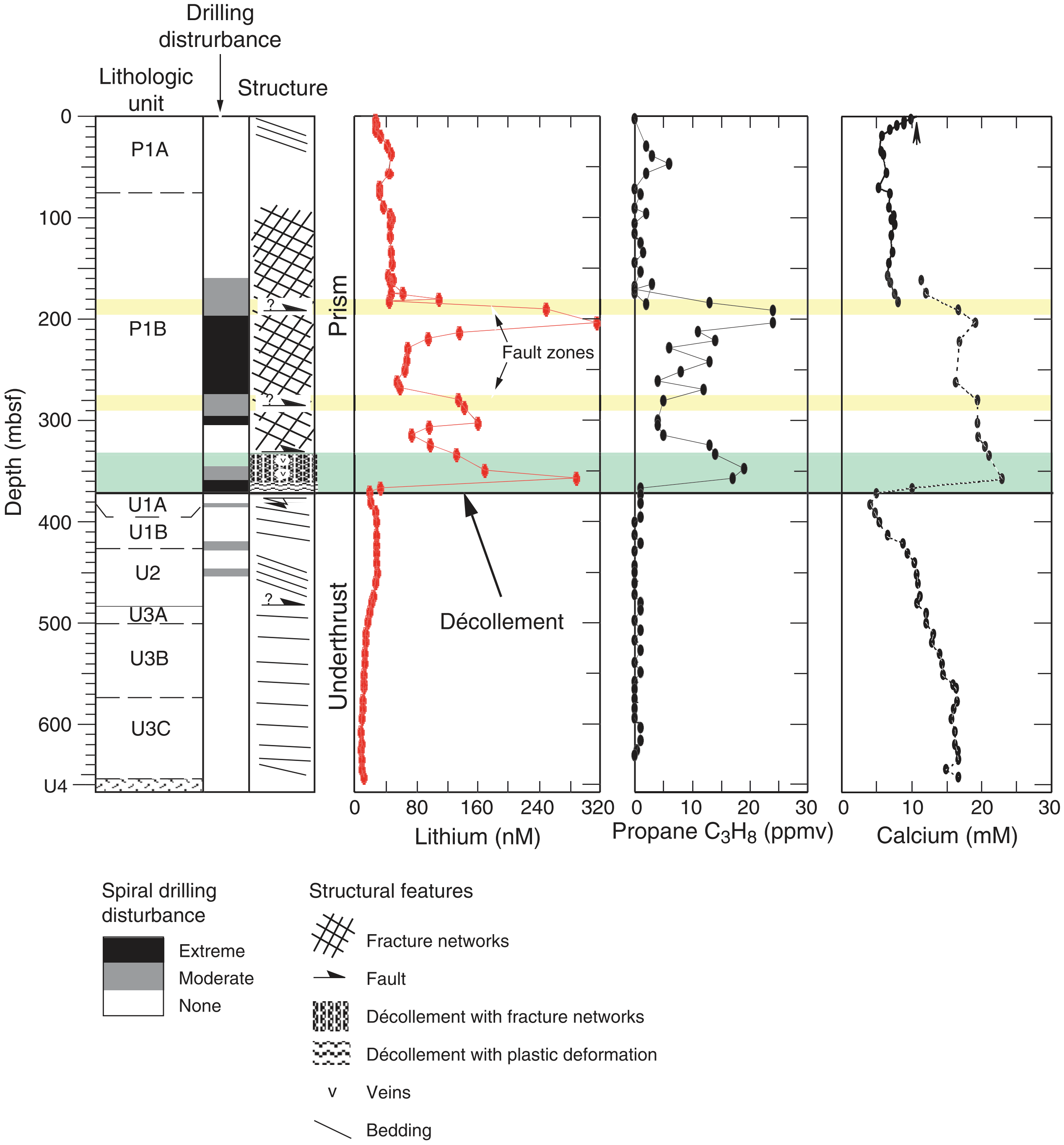

Figure F11. Pore pressures determined from consolidation tests for Site 1040 (Leg 170) and compaction ratios after Saffer (in press). The very sharp gradient in barium concentrations across the base of the décollement indicates limited vertical diffusion or advection (after M. Kastner, pers. comm., 2002).

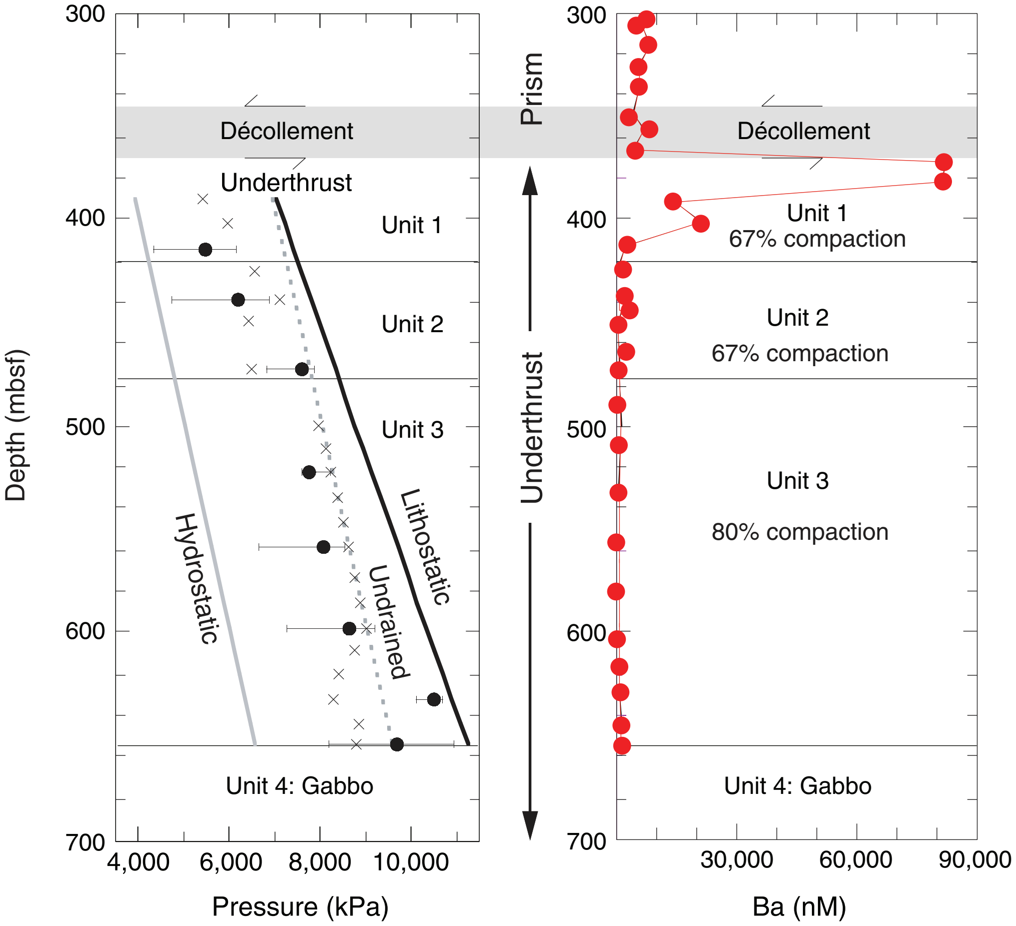

Figure F12. Schematic of a CORK-II installation for monitoring fluid flow, flow rates, pressure, and temperature (after **Jannasch et al.,** this volume). ROV = remotely operated vehicle, RCB = rotary core barrel.

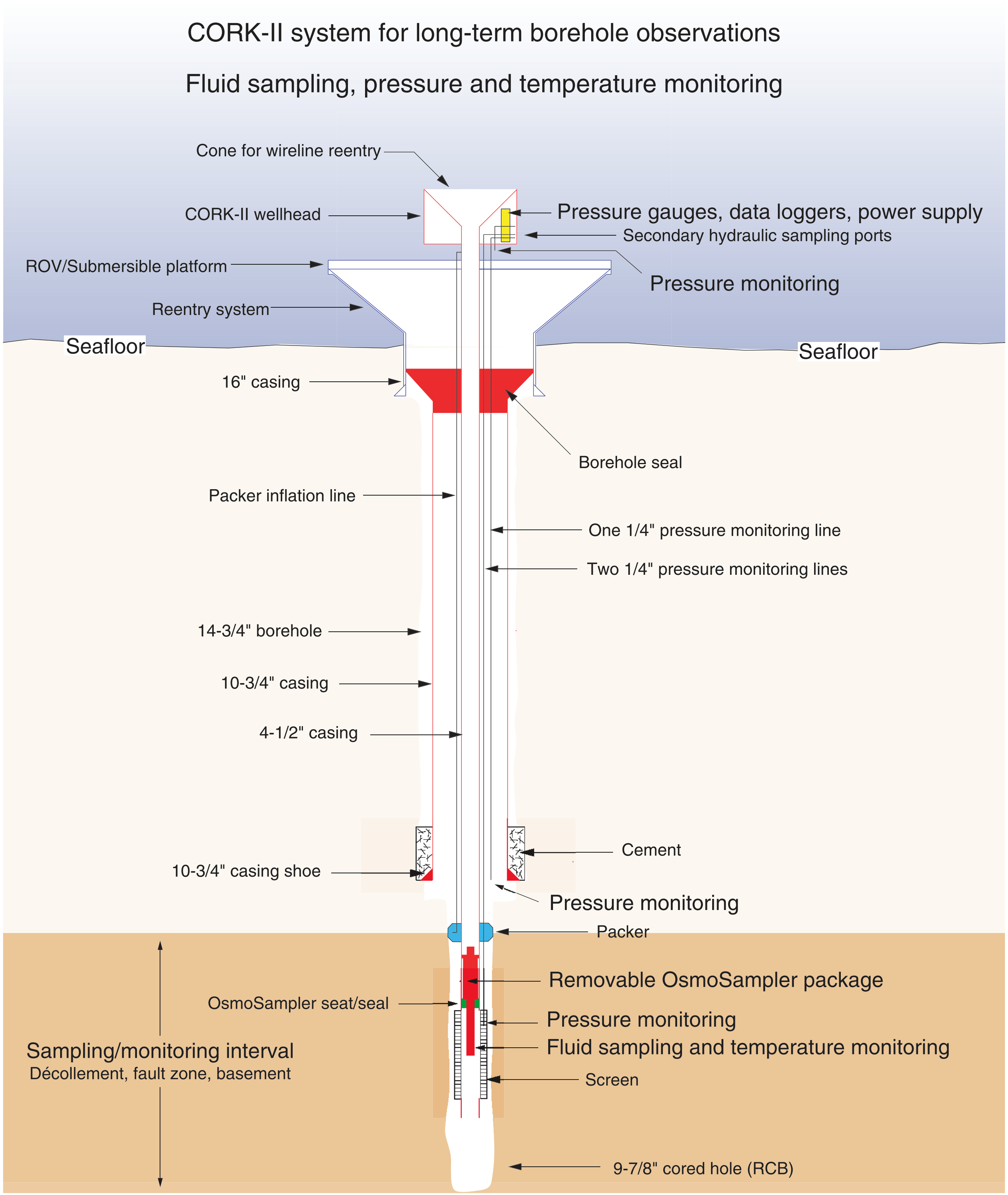

Figure F13. Portion of multichannel seismic profile BGR 99-44 across Sites 1253 and 1039. The location of the seismic profile is shown in Figure F3, p. 44. Figure F24, p. 66, shows the BGR 99-44 seismic profile across all drill sites. Vertical exaggeration = ~1.6.

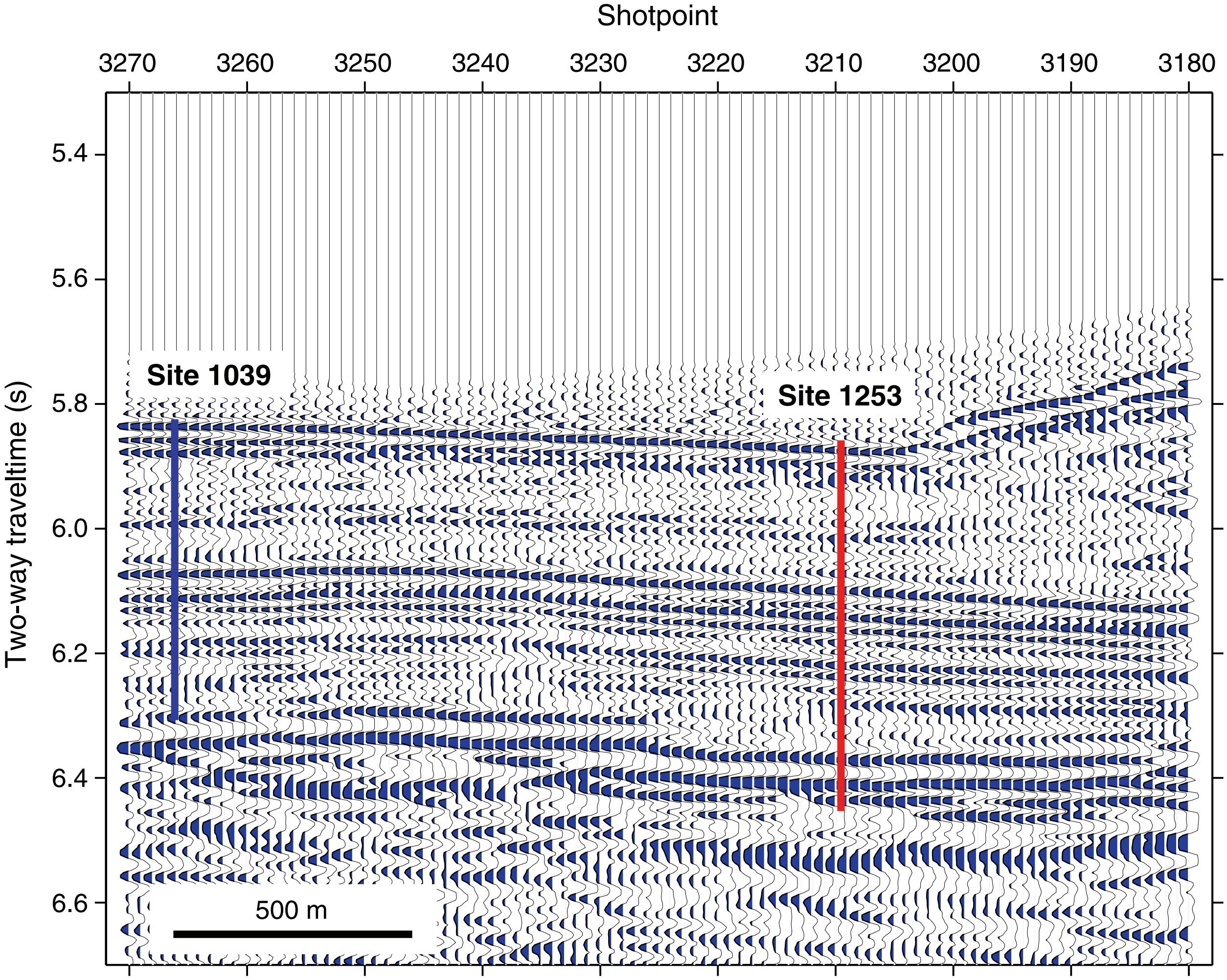

Figure F14. Composite diagram showing selected logging data annotated with physical property measurements on the cores, petrologic observations, and paleomagnetic and rock magnetism results. Petrologic and magnetic results are reported in the core reference frame, wherein Subunit 4B was curated at a depth of 450 mbsf. Logging data show that Subunit 4B begins at a depth of ~460 mbsf. Correlations between core and logging intervals are shown as solid lines to indicate major boundaries (bottom of Subunit 4A and top of Subunit 4B) or as dashed lines to indicate subunit boundaries identified petrologically. Labeled zones at the base of the petrologic section indicate the following observations: (1) location of the cryptocrystalline horizon of basaltic texture; (2) greater number of magmatic contacts; (3) more veins or voids filled with holo- and cryptocrystalline groundmass/altered glass, clay, and zeolites; (4) up to 5% degree of alteration within 1 m of Section 205-1253A-37R-1 and higher abundance of voids filled with clays and zeolites, ending in an homogeneous microcrystalline gabbro; (5) increasing number of centimeter-scale fractures and veins; and (6) very homogeneous microcrystalline to fine-grained gabbro with very weak magmatic contacts. Also indicated are the positions of the two OsmoSamplers (OS). (**Figure shown on next page.**)

Figure F14 (continued). (Caption shown on previous page.)

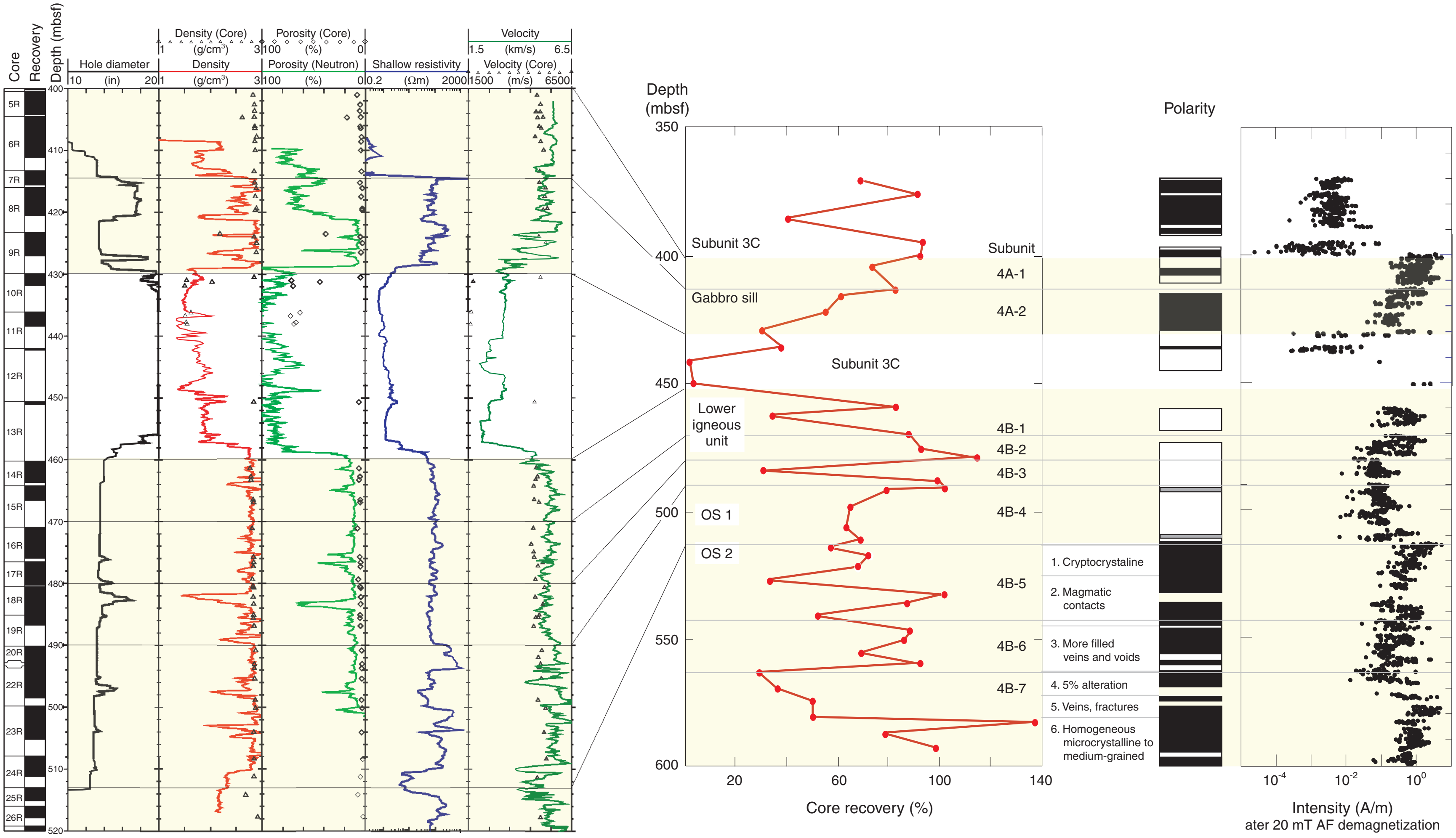

Figure F15. Core photograph and thin section photomicrographs from Subunit 4A. **A.** Close-up photograph of microcrystalline to fine-grained homogeneous holocrystalline gabbro (interval 205-1253A-8R-2 [Piece 2, 42–61 cm]). **B.** Microcrystalline gabbro observed within Subunit 4A. **C.** Completely altered primary mineral, replaced by clay (thin section 10-A; Sample 205-1253A-7R-1, 130–133 cm; 414.6 mbsf). **D.** Olivine, completely altered to clay (thin section 13-C; Sample 205-1253A-8R-1, 24–27 cm; 416.24 mbsf). **E.** Olivine, mostly replaced by clay (thin section 13-D; Sample 205-1253A-8R-1, 24–27cm; 416.24 mbsf). **F.** Altered plagioclase, replaced by a mixture of clay and isotropic secondary products (thin section 13-E; Sample 205-1253A-8R-1, 24–27 cm; 416.24 mbsf). Mag = magnetite, Pl = plagioclase, Ilm = ilmenite, Ol = olivine.

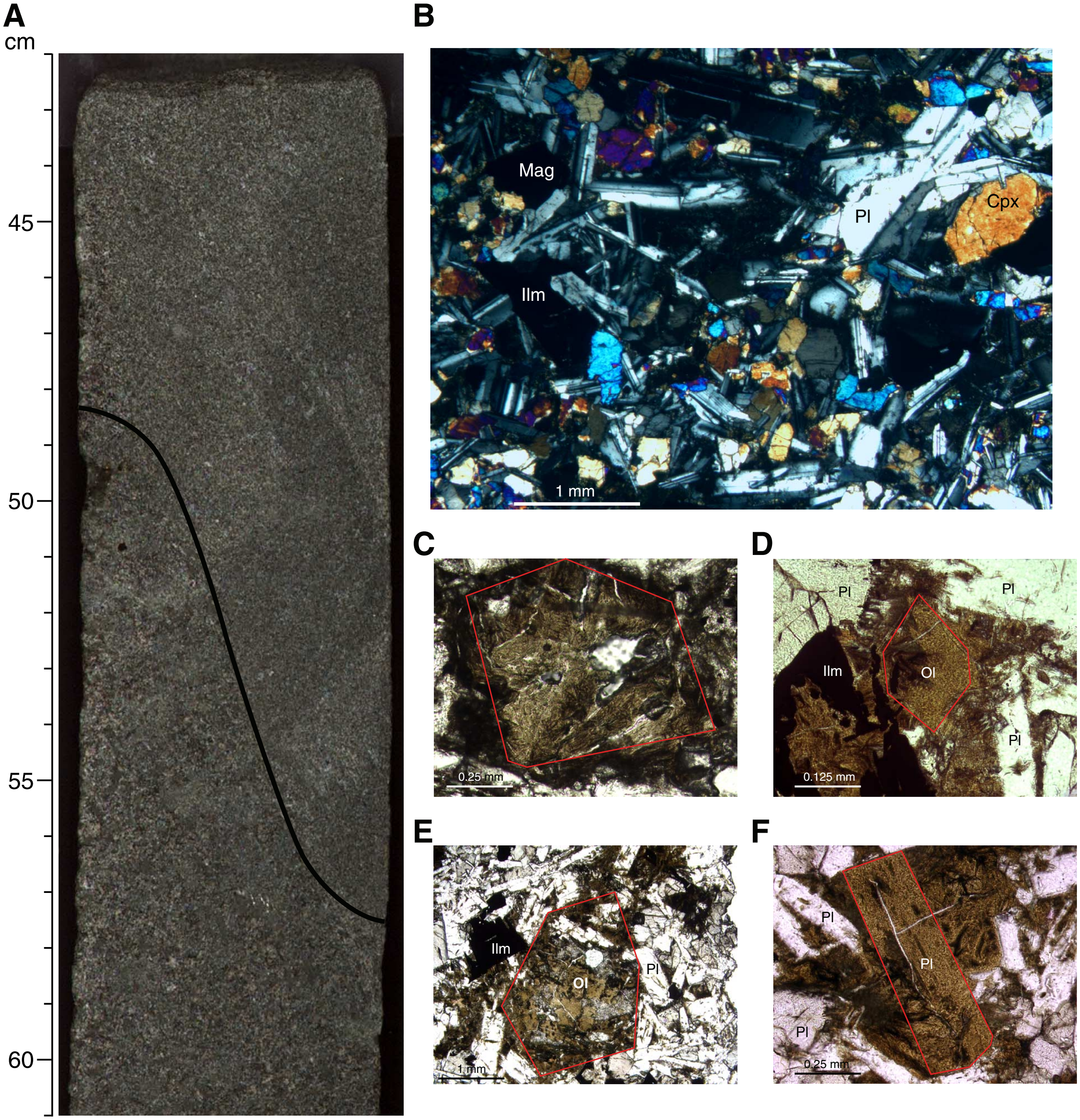

Figure F16. Core photograph and thin section photomicrographs from Core 205-1253A-17R, in the upper part of Subunit 4B. **A.** 4-mm-wide vein with glassy margin and zeolite filling (Sample 205-1253A-17R-2, 100–117 cm). **B.** Photomicrograph in cross-polarized light (XPL) taken with a blue filter at 5× magnification, showing microcrystalline gabbro (Sample 205-1253A-17R-2, 108–111 cm). **C.** Photomicrograph showing zeolites, probably mesolite or thomsonite (thin section 27-E; Sample 205-1253A-17R-2, 108–111 cm; 478.18 mbsf). Cpx = clinopyroxene, Pl = plagioclase.

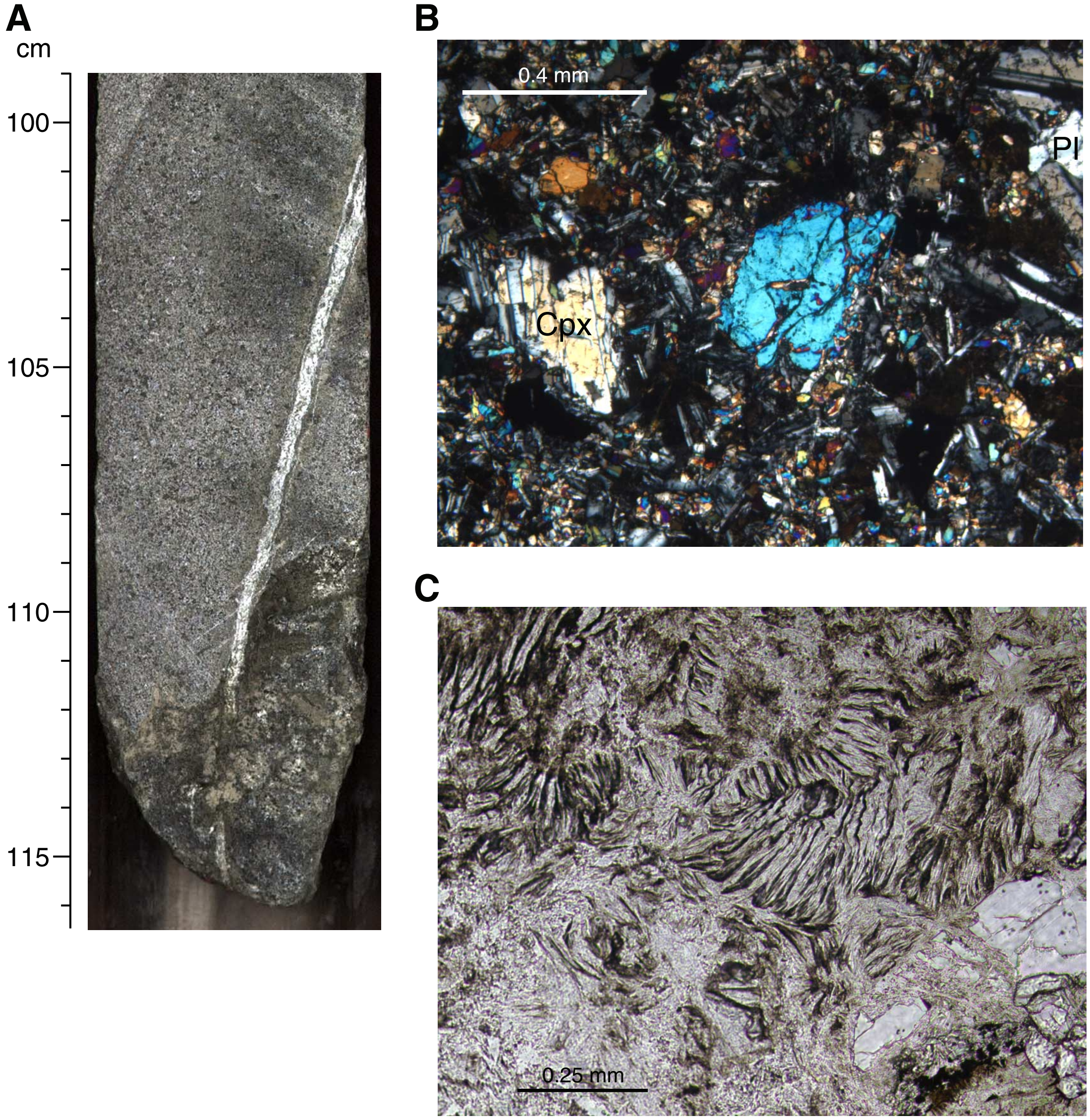

Figure F17. Core photograph and photomicrograph from Sample 205-1253A-25R-1 (Piece 9, 57.5–63.5 cm; 513 mbsf). **A.** Chilled margin of cryptocrystalline basalt including voids filled with zeolites and clay. **B.** Photomicrograph in cross-polarized light (XPL) taken with a blue filter at 5× magnification showing cryptocrystalline groundmass. Cpx = clinopyroxene.

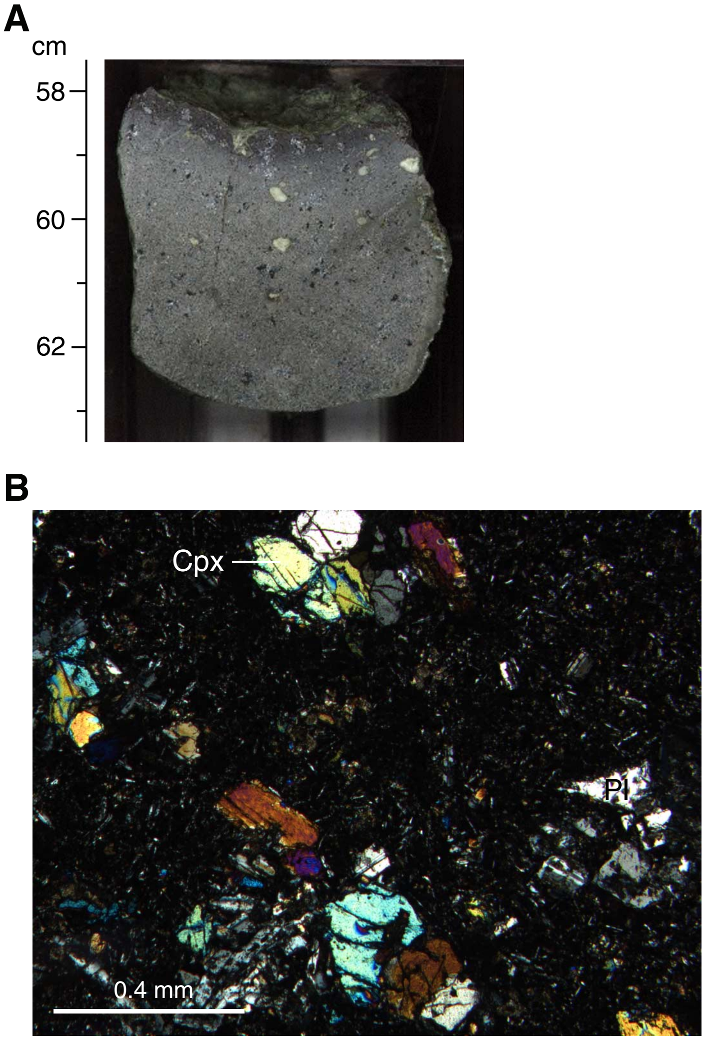

Figure F18. Composite diagram showing fracture distribution within the igneous units, core recovery and a summary of petrologic observations, and detailed FMS images for the depths at which OsmoSamplers (OS) 1 and 2 were installed.

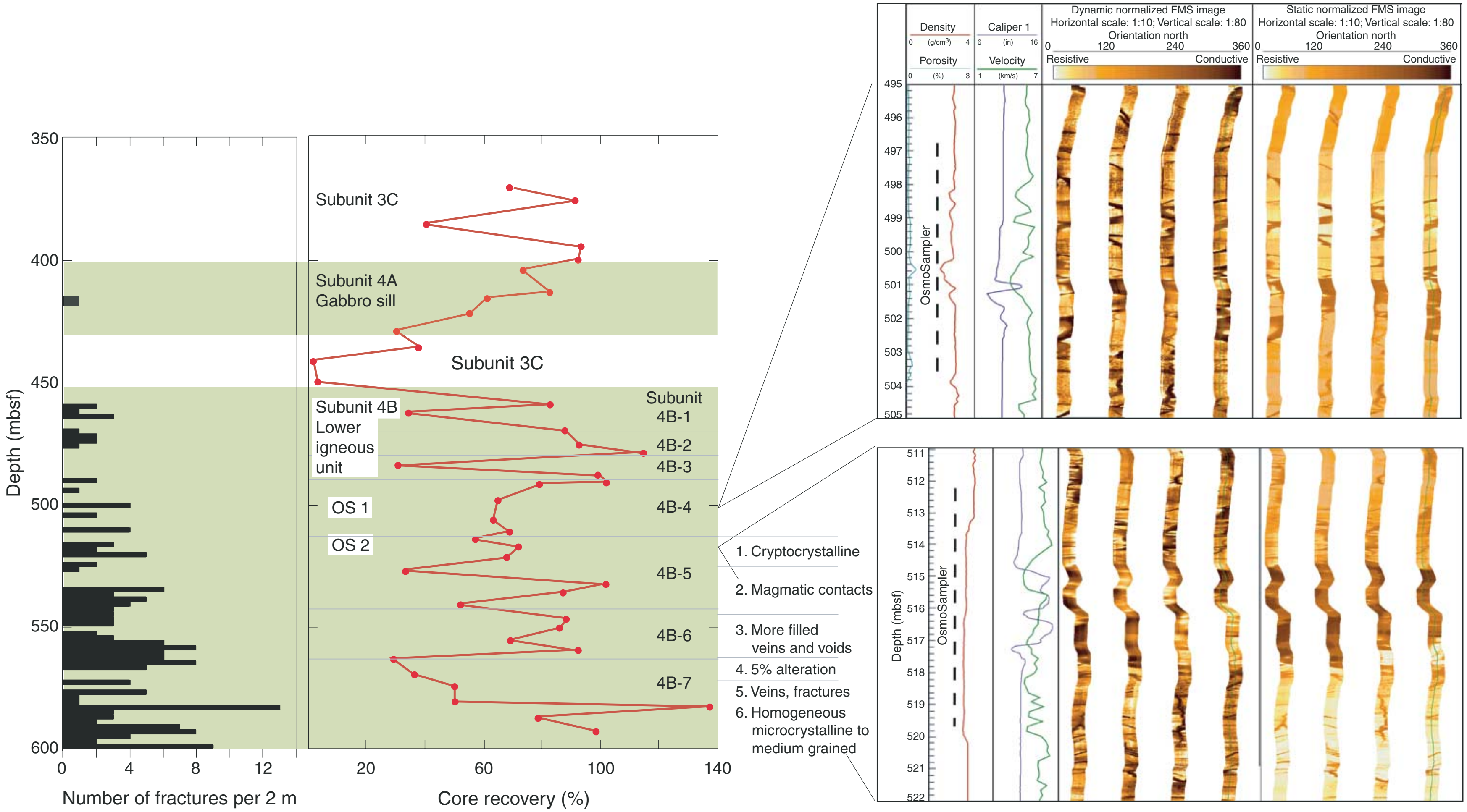

Figure F19. **A.** Photomicrograph showing the zeolite stilbite as a cavity filling in Section 205-1253A-33R-1, lower part of Subunit 4B. **B.** Vein up to 0.5 cm wide filled with pale green clay in interval 205-1253A-42R-2, 72–101 cm. The interior of the vein shows a lighter color, which could be zeolites. The sample in B was taken for microbiological studies at the interval immediately adjacent to the bottom of part B. pl = plagioclase.

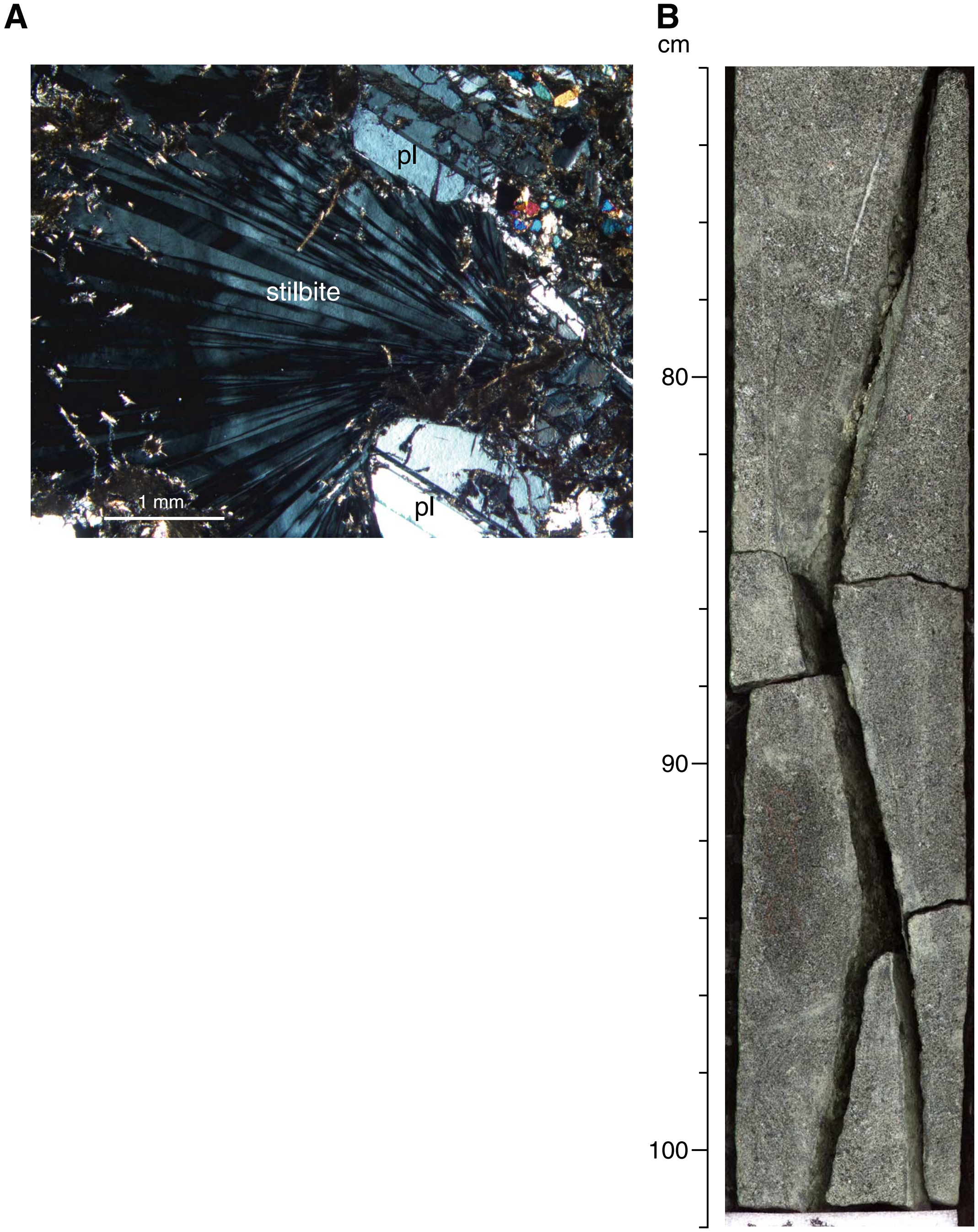

Figure F20. Composite diagram of pore fluid chemical data from Legs 205 and 170, measured just above and below the gabbro sill (Subunit 4A). Dashed horizontal line = depth of the sill in Hole 1039C for comparison.

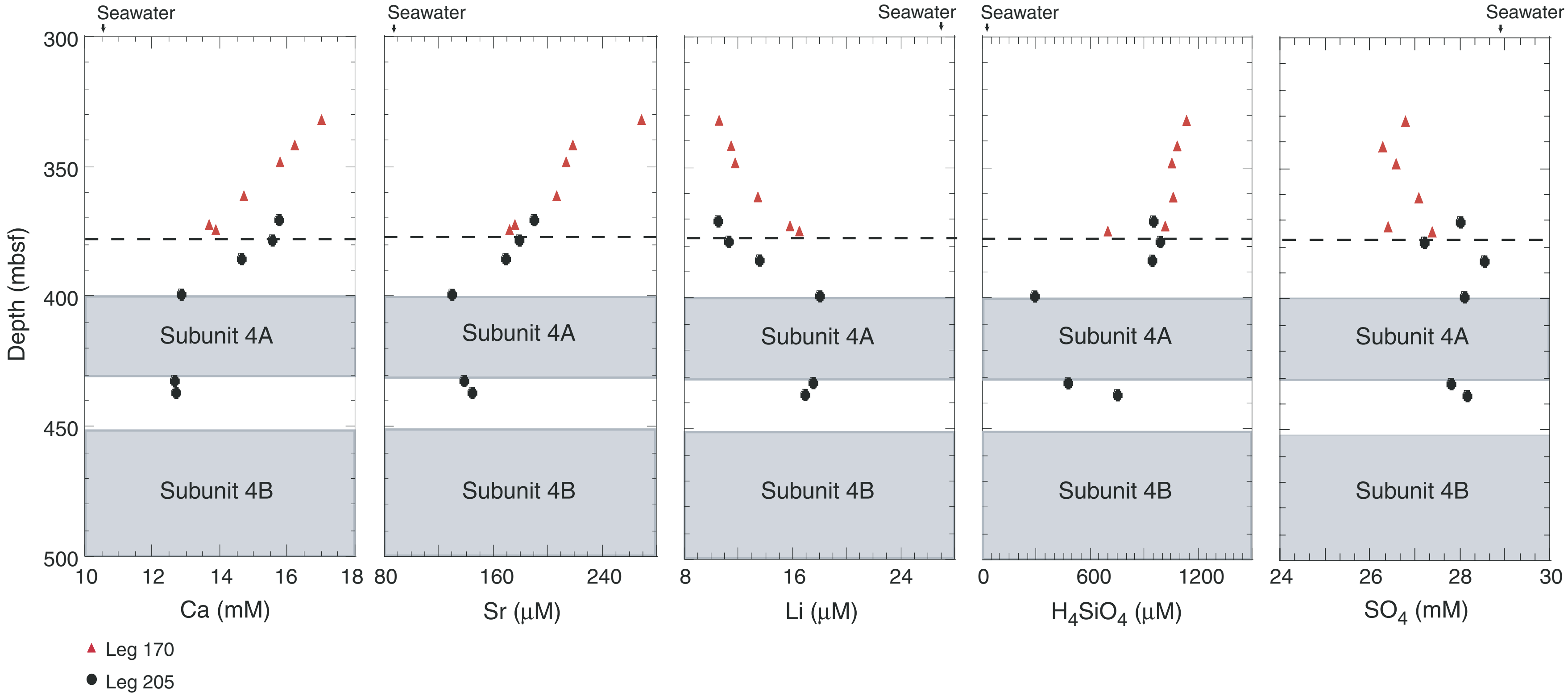

Figure F21. Hole 1253A borehole installation showing subseafloor depths for OsmoSamplers, screens, packers, and casing strings. This figure is not to scale.

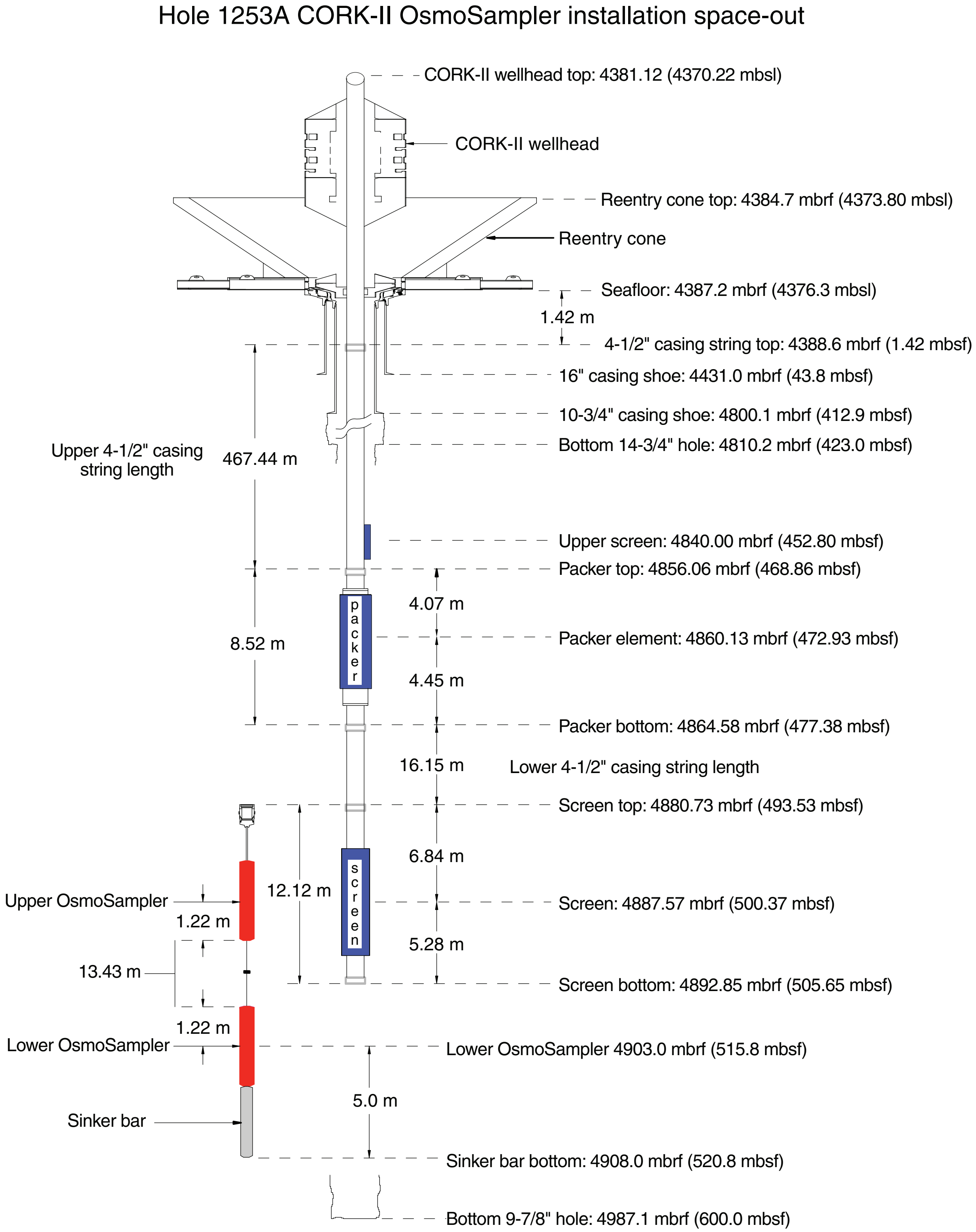

Figure F22. Location of Site 1254. Open circles = drill sites occupied during Leg 205, solid circles = drill sites occupied during Leg 170. Bathymetric map is an integration of the compilation by Ranero and von Huene (2000) and Simrad data from E. Flueh (pers. comm., 2000). LWD = logging while drilling.

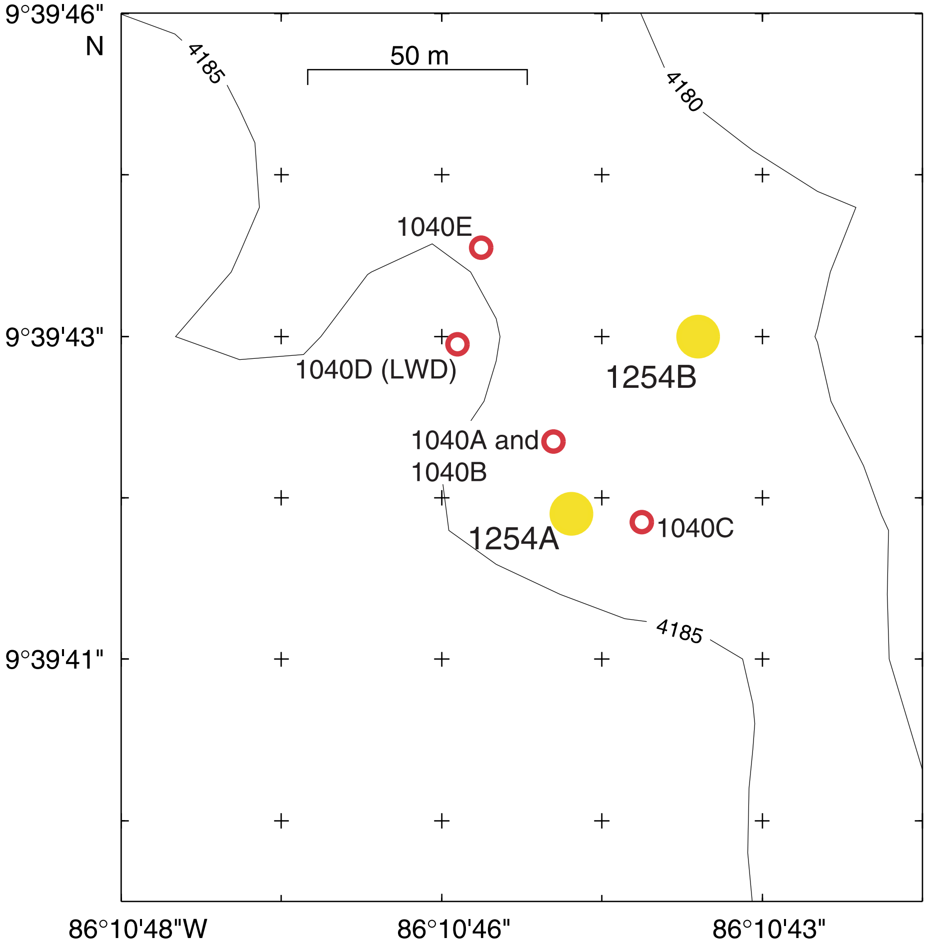

Figure F23. Portion of multichannel seismic profile BGR 99-44 across Sites 1254 and 1040. Figure F3, p. 44, shows the BGR 99-44 seismic profile across all drill sites. Vertical exaggeration = 1.7. CMP = common midpoint.

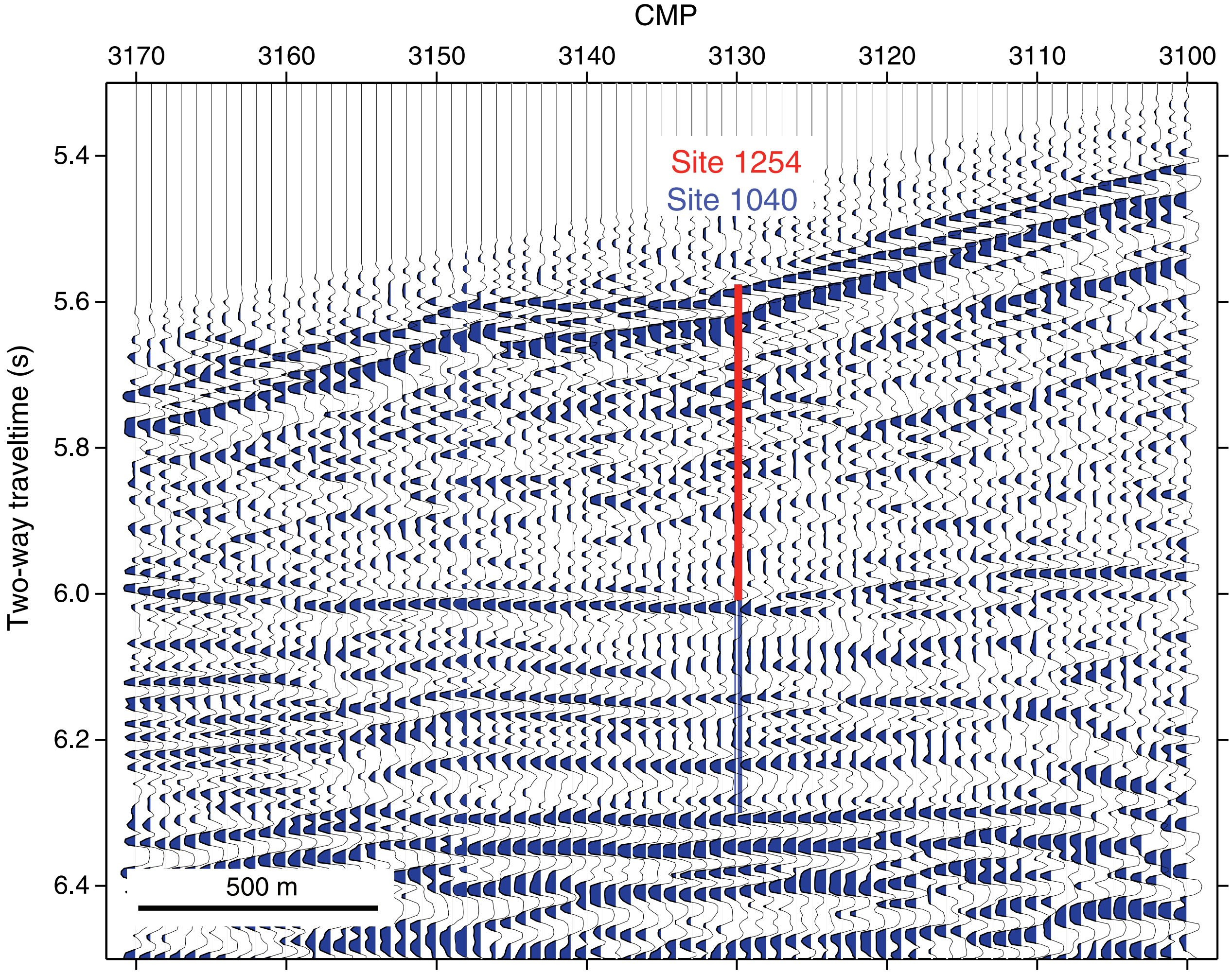

Figure F24. Summary of results in Hole 1254A. Composite view of structural and geochemical results from Hole 1254A with identification of major structural elements.

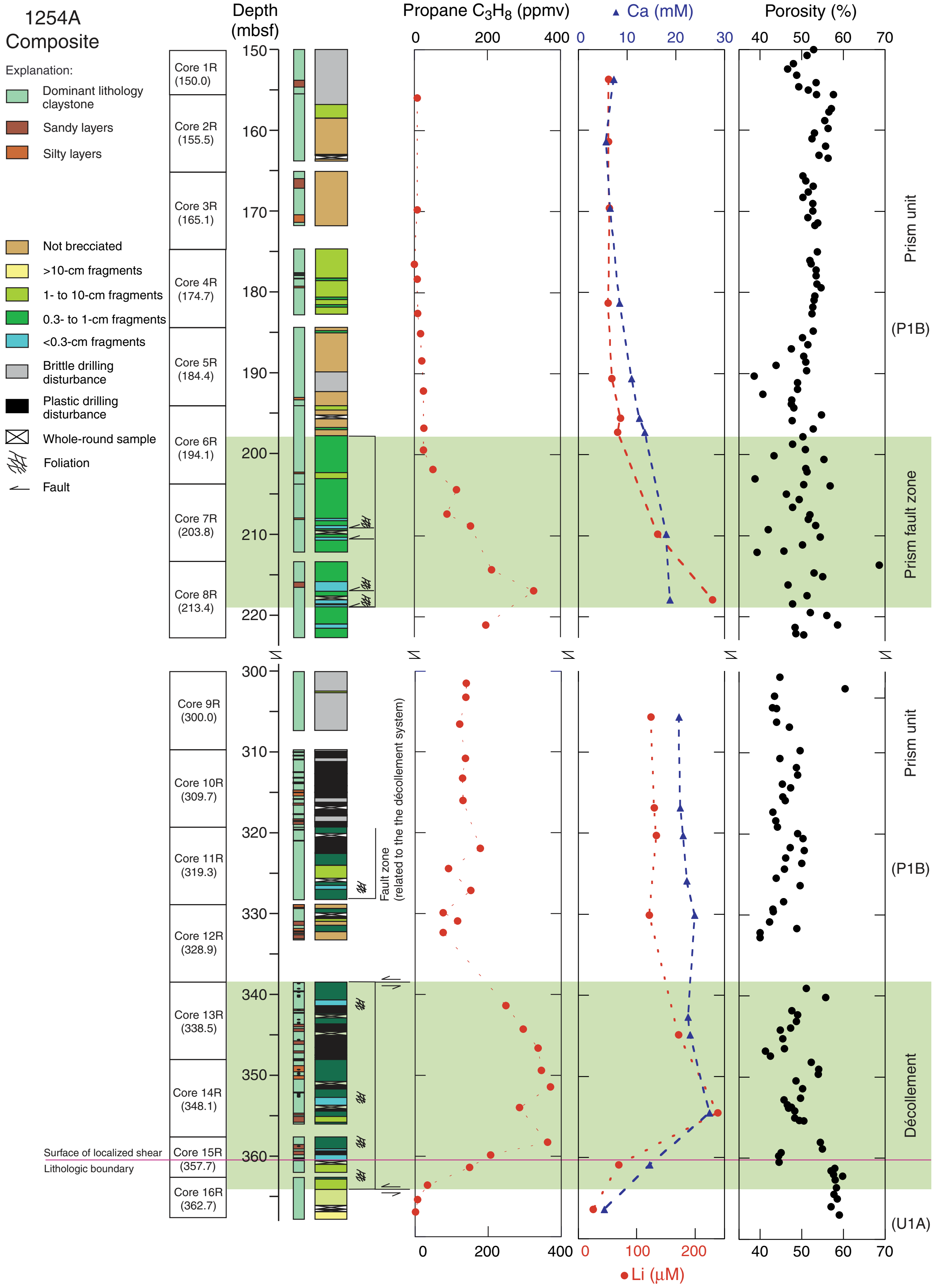

Figure F25. Photograph of the lithologic boundary between forearc prism sediments (Subunit P1B), represented here as darker claystone (interval 205-1254A-15R-2, 128–145 cm) and the underthrust sediment (Subunit U1A), which is shown here as a lighter, more silt-rich claystone.

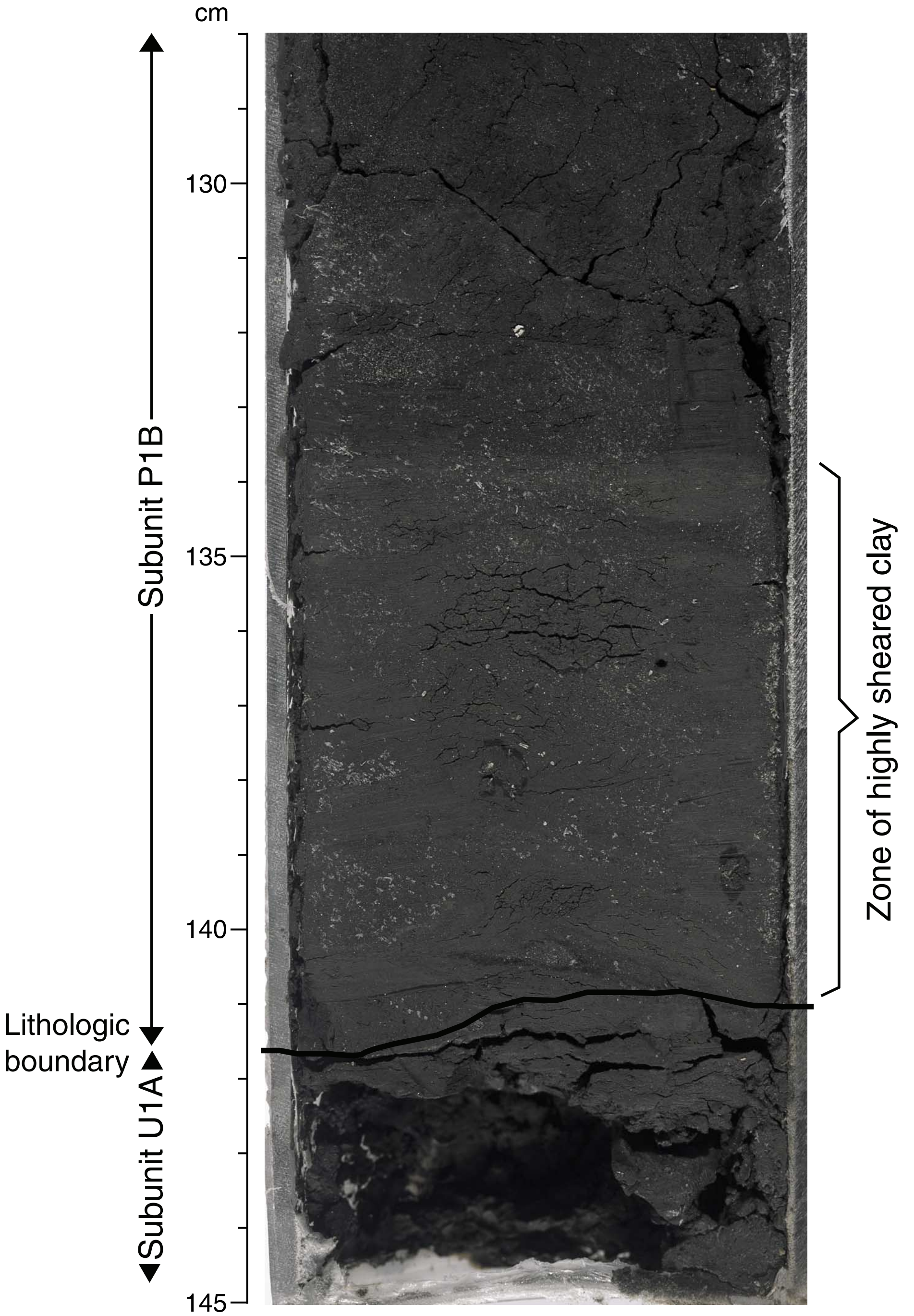

Figure F26. Photograph of deformed hemipelagic sediments (Subunit U1A) within the lowermost décollement zone (interval 205-1254A-16R-1, 96–100 cm), demonstrating that the lithologic boundary does not coincide with the base of the décollement.

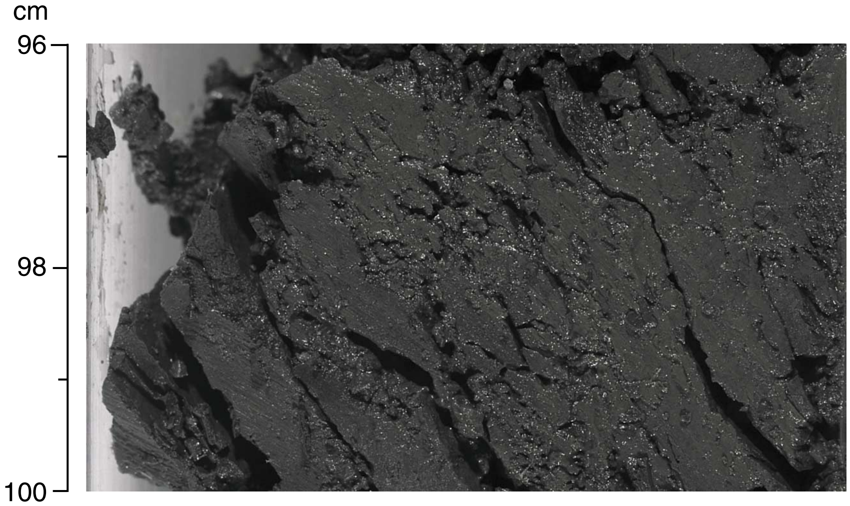

Figure F27. Photograph of a fault gouge (Riedel shear) developed by brittle shearing in a zone in the hemipelagic sediments of Subunit U1A (interval 205-1254A-16R-2, 20–32 cm) of discrete deformation.

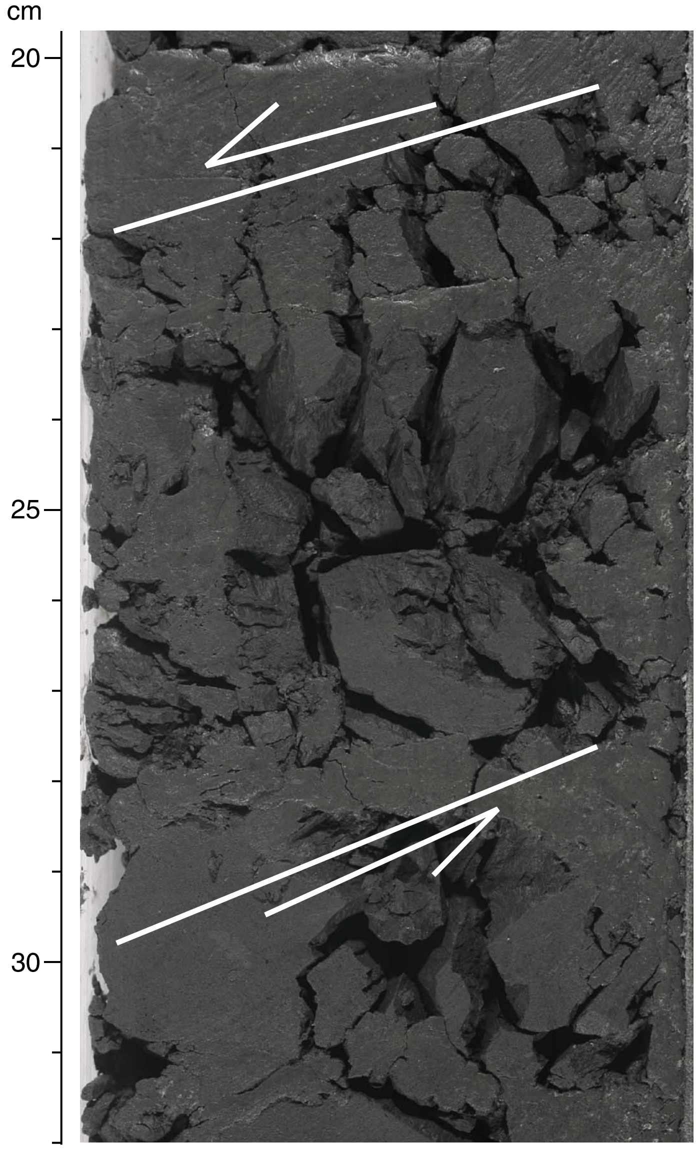

Figure F28. Location of Site 1255. Open circle = the drill site occupied during Leg 205, solid circles = the drill sites occupied during Leg 170. The bathymetric map is an integration of the compilation by Ranero and von Huene (2000) and Simrad data from E. Flueh (pers. comm., 2000).

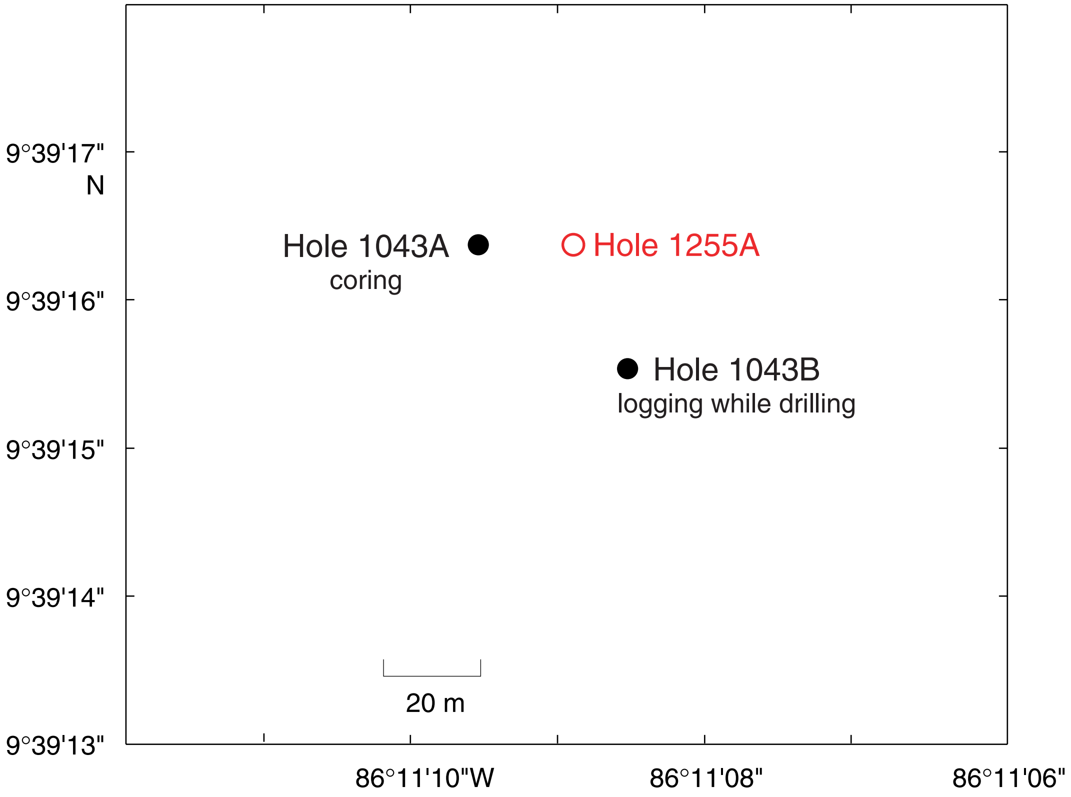

Figure F29. Portion of multichannel seismic profile BGR 99-44 across Sites 1255 and 1043. Figure F23, p. 65, shows the BGR 99-44 seismic profile across all drill sites. Vertical exaggeration = 1.7. CMP = common midpoint.

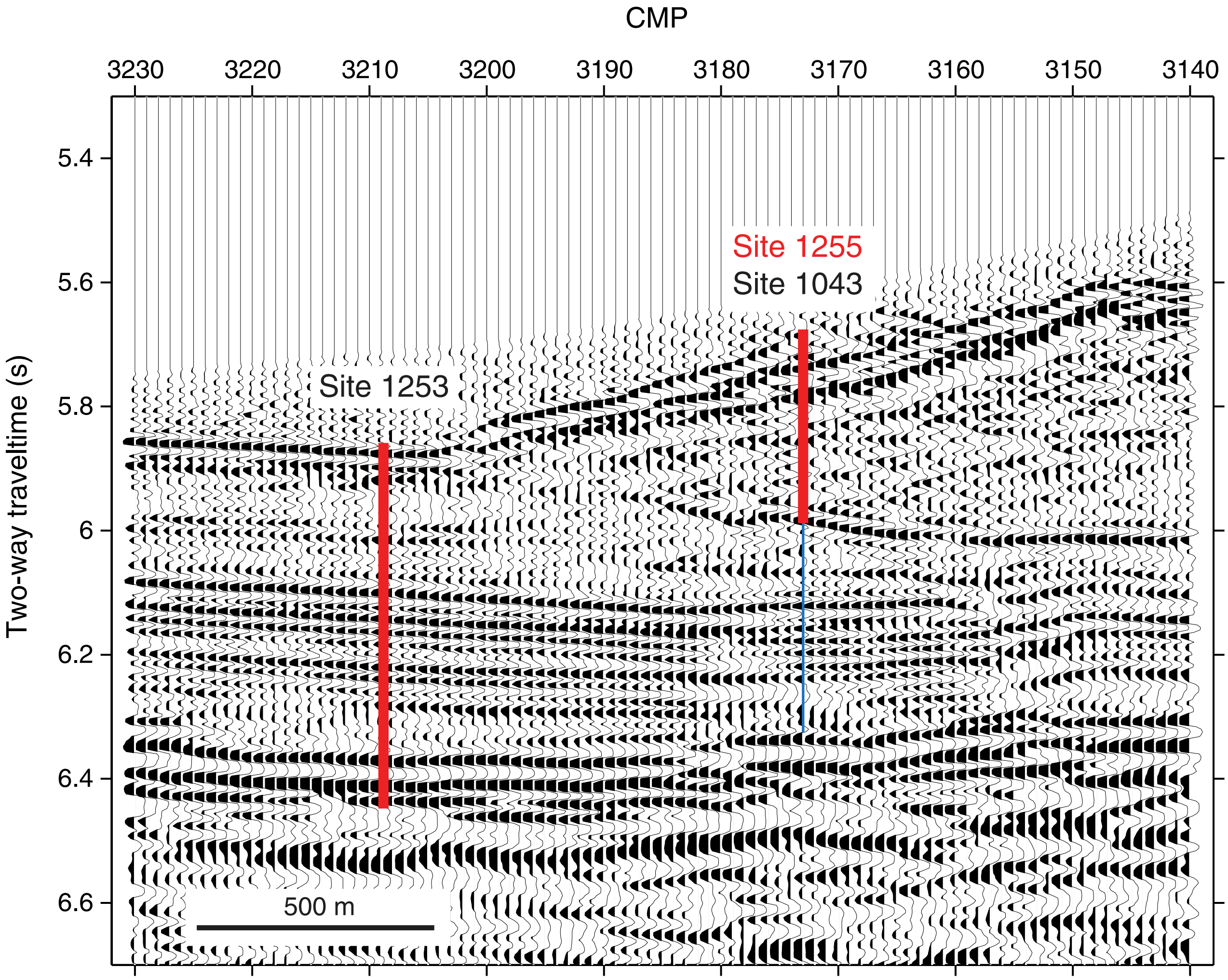

Figure F30. Hole 1255A borehole installation showing subseafloor depths for OsmoSamplers, screens, packers, and casing strings. This figure is not to scale.

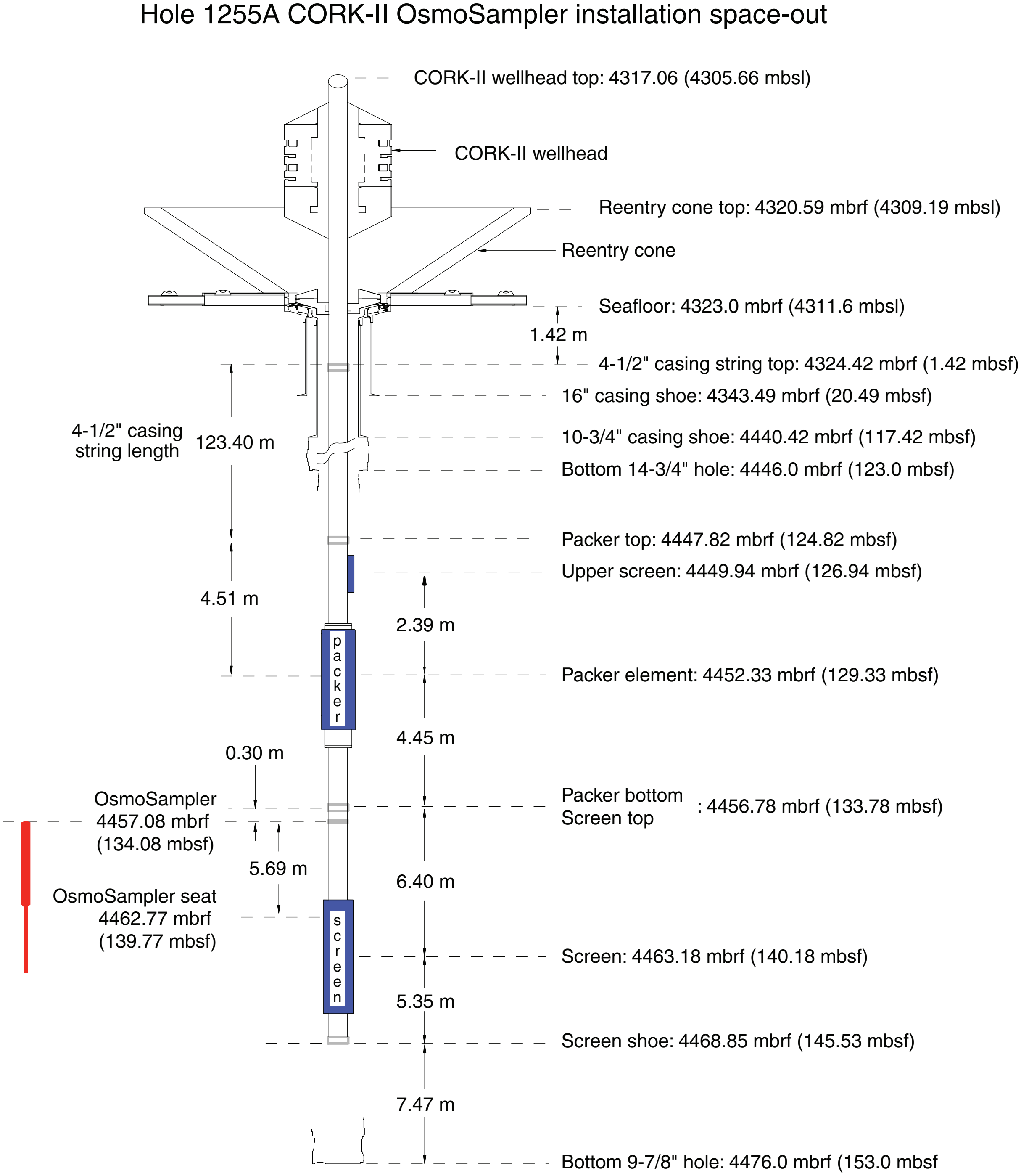

Figure F31. Video sequence showing CORK-II head and ROV landing platform of CORK-II installation at Site 1253 (K. Becker, pers. comm., 2002). (QuickTime software is available for Macintosh and Windows platforms only. Please see "QuickTime Movies" in 205IR.PDF for further information. Click the image to play the movie.)

Figure F32. Video sequence showing CORK-II head and ROV landing platform of CORK-II installation at Site 1255 (K. Becker, pers. comm., 2002). (QuickTime software is available for Macintosh and Windows platforms only. Please see "QuickTime Movies" in 205IR.PDF for further information. Click the image to play the movie.)

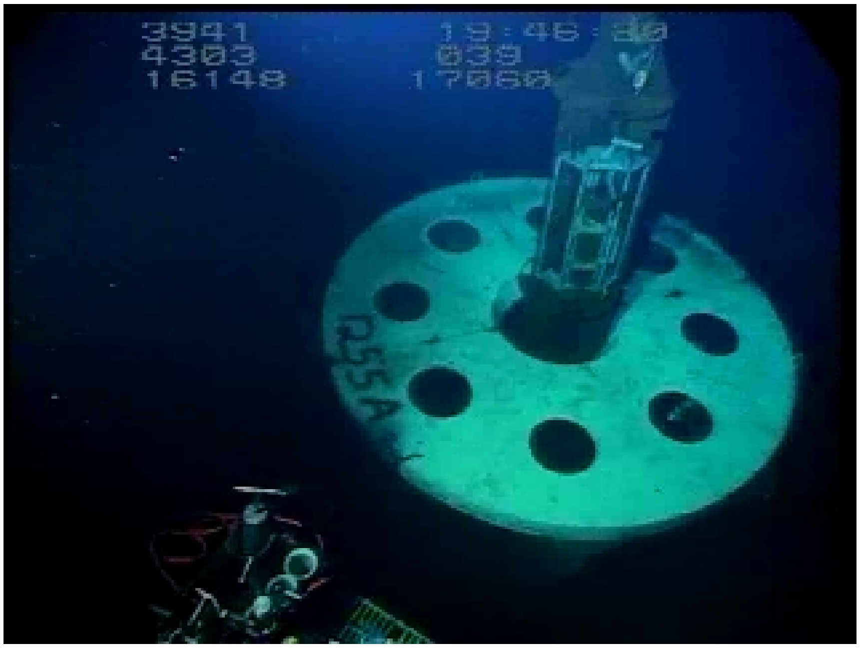

Table T1. Leg 205 operations summary.

Hole	Latitude	Longitude	Water depth (mbsl)	Number of cores	Cored interval (m)	Core recovered (m)	Core recovery (%)	Drilled interval (m)	Total penetration (m)	Time on hole (day)	Comments
1253A	9°38.8583′N	86°11.4337′E	4376.3	43	230.0	148.38	65.0	370.0	600.0	19.72	Cored; installed CORK-II
1254A	9°39.6989′N	86°10.7435′W	4182.8	16	140.5	125.00	89.0	227.0	367.5	7.98	Cored fault zone and décollement; attempted CORK-II installation; 10¾-in casing collapsed; hole abandoned.
1254B	9°39.7187′N	86°10.7274′W	4175.6	0	0.0	0.00	0.0	278.0	278.0	7.31	Attempted CORK-II installation; 4½-in casing parted; attempted but failed to remove casing stuck in hole; hole abandoned. Note: Time on hole does not include time fishing at end of leg.
1255A	9°39.2716′N	86°11.1492′W	4311.6	4	34.0	7.22	21.0	123.0	157.0	6.97	Cored décollement; installed CORK-II.
		Leg 205 totals:		63	404.5	280.60	69.0	998.0	1402.5	41.98	